

LIFETIMES OF SUPERDEFORMED STATES IN ^{38}Ar

By

ROBY ANNE ELIZABETH AUSTIN, B.Sc. M.Sc.

A Thesis

Submitted to the School of Graduate Studies

in Partial Fulfillment of the Requirements

for the Degree

Doctor of Philosophy

McMaster University

© Copyright Roby Austin, 2004

LIFETIMES OF SUPERDEFORMED STATES IN ^{38}Ar

DOCTOR OF PHILOSOPHY (2004)
(Physics)

McMaster University
Hamilton, Ontario

TITLE: Lifetimes of Superdeformed States in ^{38}Ar

AUTHOR: Roby Anne Elizabeth Austin, B.Sc., M.Sc.(McMaster University)

SUPERVISOR: Dr. J. C. Waddington

NUMBER OF PAGES: xii, 137

Abstract

Light nuclei provide an ideal laboratory for the study of the interplay between collective and single-particle interactions of nucleons. This thesis provides evidence via the lifetimes of states that the light nucleus ^{38}Ar undergoes superdeformation. Two highly deformed bands have been identified, one with a deformation parameter $\beta_2 = 0.30 \pm 0.03$. The deformation parameter of the more excited and more deformed band is less well measured, and it falls between $\beta_2 = 0.68$ and $\beta_2 = 0.95$. Superdeformation, the phenomenon in which a nucleus takes on an elongated shape with one axis approximately twice as long as another, occurs when nuclei are experiencing extreme conditions, particularly high angular momentum. The superdeformation of the nucleus ^{38}Ar is especially interesting because there is ample opportunity for interactions between superdeformed structures and normal deformed structures.

Acknowledgements

Thanks are first due to Jim Waddington. A brief scan of acknowledgements in the theses of students before me reflects my sentiments. No better supervisor can be found than Jim Waddington. Indeed, we would be hard pressed to find a better person. It has been my very great pleasure to know him and to work with him. I know just how lucky I have been.

I would also like to thank the rest of my committee: Both Brian King and Fiona McNeill have offered very interesting suggestions and support. I have enjoyed discussing my work with them and am grateful to them for all of their valuable assistance over the years.

I have worked with a good many people throughout my graduate degrees and have been fortunate to find friendships with most of them. Thanks to Carl Svensson, Greg Hackman, Gordon Ball, David Ward, Andreas Gorgen, Peter Klages, Geoff Grinyer, Tom Rodinger, Kristen Koopmans, Michelle Lee, Chris Malcolmson, Noel Novo, George Reed, Dirk Rudolph, Corina Andreiou, Augusto Macchiavelli, Duncan Appelbe, Mario Cromaz, Brent Washbrook, Paul Fallon, I-Yang Lee, Mike Carpenter, Robert Janssens, Dimitrios Sarantites, and many more.

Connie Roth has been a tremendous support for many years in matters of physics and the rest of life, too. Thanks also to Wendy Malarek, Cheryl Johnston, and Rose McNiece, and Sue Waddington, all of whom are reliable for great chats about things *not* physics. Marg Wilby is responsible for sending me along the path to nuclear physics and for that I will always be grateful. She changed my life for the better. So did my high school physics teacher, Bruce Robb, who in a single deft

question illustrated that even a final exam in physics can be funny enough to make us all laugh out loud.

Last, but of course not least, thanks to Michael Dunlavy without whose constant support and friendship I wouldn't feel like doing much, let alone be able to. With love, I dedicate this thesis to him.

Contents

Abstract	iii
Acknowledgements	iv
List of Figures	viii
List of Tables	xi
1 Introduction	1
2 Concepts	3
2.1 Nuclear Shapes	3
2.1.1 Nuclear Characteristics	4
2.1.2 Nuclear Deformation	4
2.1.3 Triaxiality	6
2.2 Superdeformation	8
2.3 Nuclear Decays	11
2.4 Quadrupole Moments and Lifetimes	13
2.5 Shell Model	14
2.5.1 Particle-Hole Configurations	16

2.6	Mixing	17
3	Experiment	19
3.1	GSFMA93	19
3.2	Heavy Ion Fusion-Evaporation Reactions	20
3.3	Detecting γ Rays	23
3.3.1	Electron-Positron Pair Production	28
3.3.2	The GAMMASPHERE Detector Array	28
3.4	Detecting Charged Particles	31
3.4.1	The MICROBALL Detector Array	32
3.5	Accelerating Projectiles	34
3.5.1	ATLAS	34
3.6	Experimental Considerations	37
3.6.1	Contamination	37
4	Analysis	39
4.1	γ - γ Matrices	39
4.2	Total Energy Plane	45
4.2.1	Unexpected Total Energy Plane Data	46
4.3	Off-Line Compton Suppression	58
4.4	Thin-Target Doppler Shift Attenuation Method	63
4.4.1	Side Feeding	66
4.4.2	Target Thickness	66
4.4.3	Stopping Powers	66
4.5	Determination of the Lifetimes	67

4.5.1	MICROBALL Bias	70
4.5.2	Exit Velocity	75
4.5.3	Initial Velocity	78
4.5.4	Target Thickness and Beam Energy	82
4.6	Sorting the Data	87
4.6.1	Double Gates	88
4.7	Implementation	89
5	Results	90
5.1	Level Scheme of ^{38}Ar	91
5.1.1	3182 & 3180 keV Doublet	94
5.2	Shell Model Configurations	97
5.2.1	Superdeformed Band Configurations	102
5.3	Lifetimes	107
5.4	Summary	117
6	Conclusions	120
A	Gamov Approximation	122
B	Table of Symbols and Abbreviations	126
	Bibliography	130

List of Figures

2.1	Potential Energy of Orbitals Varying with Deformation	7
2.2	The Superdeformed Minimum	9
2.3	Superdeformed Band in ^{152}Dy	10
3.1	Heavy Ion Fusion-Evaporation Reactions	21
3.2	Feeding of the Residual Nucleus	22
3.3	Compton Suppression	27
3.4	Escape Scattering	29
3.5	GAMMASPHERE at ANL	30
3.6	GAMMASPHERE Detectors	31
3.7	The MICROBALL	33
3.8	ATLAS Electron Cyclotron Resonance Ion Source	35
3.9	Linear Accelerator	36
4.1	Partial Level Scheme of ^{38}Ar	41
4.2	A γ - γ Matrix	43
4.3	Coincidence Gates	44
4.4	Total Energy Plane Gating	47
4.5	Total Energy Plane for ^{37}Cl	48

4.6	^{37}Cl Level Scheme and Total Energy Plane Profiles	50
4.7	Evaporated Particle Energies	54
4.8	Simple Calculation of Lifetimes of Proton Evaporation from ^{38}Ar	55
4.9	Known Levels in ^{38}Ar and ^{37}Cl	56
4.10	Total γ -Ray Energy and Yrast States for ^{38}Ar and ^{37}Cl	57
4.11	Near-Neighbour Scattering	60
4.12	GAMMASPHERE Near-Neighbour Map	61
4.13	Doppler Shifted Fast Transitions	62
4.14	Sample DSAM fit	65
4.15	Stopping Powers of ^{38}Ar	68
4.16	Velocity Distribution of the Recoils	71
4.17	Effect of Number of Events on the Average	72
4.18	Z-direction Kicks to the Recoils	73
4.19	Exit Velocity	75
4.20	X- and Y- Direction Kicks to the Recoils	76
4.21	Beam Energy Loss in the Target	83
4.22	Target Thicknesses for Given Energies and Velocities	85
4.23	Exit Velocity and Target Thickness for 80 MeV Beam	87
5.1	Level Scheme of ^{38}Ar	94
5.2	Evidence for Placement of 3183 keV Doublet	98
5.3	Angular Momentum 11 Negative Parity Band	101
5.4	Angular Momentum 13 Negative Parity Band	103
5.5	Schematic of Levels in Deformed Bands	106
5.6	“Simple” Fit of $F(\tau)$ Values	108

5.7	Smoothly Varying Q_t Fits of Deformed Bands	111
5.8	Fit of Yrast Deformed Band with Quadrupole Moment Constant . . .	113
5.9	Highly Deformed Bands	118

List of Tables

2.1	Some Values of Deformation Parameters	8
4.1	$F(\tau)$ Values at Exit Velocity Measured in Different Gates	77
4.2	Initial $F(\tau)$ Values for 2610 keV Transition	78
4.3	Comparison of $F(\tau)$ Values	81
4.4	Initial $F(\tau)$ Values for Transitions Above the 2576 keV Transition	82
5.1	Energies and Relative Intensities of Gamma Rays	92
5.1	(Continued) Energies and Relative Intensities of Gamma Rays	94
5.1	(Continued) Energies and Relative Intensities of Gamma Rays	95
5.1	(Concluded) Energies and Relative Intensities of Gamma Rays	96
5.2	“Simple” Fit of the Transition Quadrupole Moments	109
5.3	Lifetimes from Fits of Smoothly Varying Quadrupole Moments	112
5.4	Lifetimes of the Yrast Band	113
5.5	Fits to the Q_t of Individual Transitions	115
5.6	In-Band Transition Differences	119

Chapter 1

Introduction

One of the first things that attracted me to the study of nuclear physics was how hodgepodge our understanding of it seemed to me (an undergraduate). I could write down a single equation that encapsulated the state of our knowledge of gravitational interactions. In only four equations, I could express all there is to say about electromagnetic interactions. But nuclear interactions, the strong force and the weak force, have so far avoided such elegant summaries. Tom Stoppard expressed it nicely in his play *Hapgood* when he let his physicist character say:

There is a straight ladder from the atom to the grain of sand, and the only real mystery in physics is the missing rung. Below it, particle physics; above it, classical physics; but in between, metaphysics. [Sto94]

Stoppard is a playwright and not a physicist, and since he is such a good playwright, I forgive him for painting my studies with the somewhat derogatory brush labelled “metaphysics”. Still, the fact remains that while practitioners of many other disci-

plines of physics like to explore theories that begin from physical principles, nuclear physicists tend to begin with experimental data and work out models.

In nuclear structure physics there have traditionally been two models to play with. There is a microscopic model that scrutinizes each individual nucleon and each interchange between nucleons. This model quickly becomes unwieldy as the number of constituent nucleons increases. There is a model that takes principles of macroscopic physics and assigns the behaviour of bulk materials to nuclear matter. Such a treatment circumvents the difficulties of the dreaded “many body problem”, but introduces new problems because nucleons congregate in nuclei in numbers small enough to make “bulk matter” assumptions inappropriate.

This thesis probes the intersection of the two models. Data are presented for ^{38}Ar that give evidence for superdeformation, a phenomenon which emerges from mean field approximations. However, the relatively small number of nucleons in ^{38}Ar makes it almost calculable microscopically. The investigation begins with a discussion of some concepts of nuclear structure physics, followed by a detailed description of experimental procedures and a thorough account of analysis techniques. Finally, the thesis presents the evidence of superdeformation in ^{38}Ar , followed by a brief discussion of its implications.

Chapter 2

Concepts

2.1 Nuclear Shapes

The collective body of the nucleus can be approximated as a shape with a given radius. Since nuclear matter is incompressible, its density drops off sharply at some radius. The radial range over which the density drops from 90% to 10% of its maximum value is defined as the skin thickness. The radial distance where the density is 50% of its maximum value is called the “radius”. Clearly, the nucleus is a collection of quantum mechanical objects and is itself small enough to exist in the quantum realm. That said, it is convenient to ascribe classical notions, such as radius, to the nucleus to provide a bridge for visualisation and other useful classical things. It will be standard in this thesis, particularly in this chapter, to refer to things, like radii, which only exist in the classical world. I will do my best always to give a definition of those classicisms which is congruent with quantum mechanics.

2.1.1 Nuclear Characteristics

There have traditionally been two ways to describe nuclear matter. One way, which might be called “bottom-up”, focuses on the individual nucleons and the way their individual characteristics sum to make the characteristics of the nucleus as a whole. The other way to describe nuclear matter takes a “top-down” approach, in which the average characteristics of the bulk nuclear material are examined to understand the characteristics of a nucleus. These two views are the single-particle and collective models.

2.1.2 Nuclear Deformation

One approximate way to describe a nucleus is as a liquid drop. The natural shape for a liquid drop is that which minimizes the surface tension: a sphere. And just as a real liquid drop will lose its spherical shape under certain forces (for example, if it is given angular momentum), a nucleus will be non-spherical under some conditions. In fact, it will be non-spherical under most conditions. The primary influence away from nuclear sphericity is nuclear shells. At a closed shell, nuclei tend to be spherical. However, between closed shells, nuclei have deformed shapes.

This thesis deals with the deformation of ^{38}Ar , so it will be necessary to introduce the standard language of nuclear deformation here. This job is made difficult because the axiom that “necessity is the mother of invention” is particularly applicable to this aspect of the field and there are many “standards” to choose from.

The nuclear shape may be described as a deformed sphere, with a radius which

is dependent on θ and ϕ . A useful expansion from the spherical radius, R_0 is

$$R = R_0 \left[1 + \sum_{\lambda=0}^{\infty} \sum_{\mu=-\lambda}^{\lambda} \alpha_{\lambda}^{\mu} Y_{\lambda}^{\mu}(\theta, \phi) \right], \quad (2.1)$$

where

$$Y_{\lambda}^{\mu}(\theta, \phi) = \sqrt{\frac{(2\lambda+1)(\lambda-|\mu|)!}{4\pi(\lambda+|\mu|)!}} e^{i\mu\phi} (1-\cos^2\theta)^{|\mu|/2} \times \left(\frac{d}{d\cos\theta}\right)^{|\mu|} \frac{1}{2^{\lambda}\lambda!} \left(\frac{d}{d\cos\theta}\right)^{\lambda} (\cos^2\theta-1)^{\lambda} \quad (2.2)$$

are the spherical harmonic functions. The terms α_{λ}^{μ} ensure that volume is conserved.

The first spherical harmonic function is a constant, so it can be absorbed into R_0 and the sum can begin at $\lambda = 1$. The second spherical harmonic functions, with $\lambda = 1$ represent motion of the centre of mass. We will choose a reference frame where the centre of mass is stationary, and set

$$\alpha_1^{\mu} = 0. \quad (2.3)$$

Thus the first interesting terms in the expansion are those with $\lambda = 2$. Of those terms, only the $\mu = 0$ term is axially symmetric (i.e. independent of ϕ) and so, for the time being, we'll set

$$\alpha_2^{\pm 2} = 0 \quad (2.4)$$

$$\alpha_2^{\pm 1} = 0. \quad (2.5)$$

For many nuclear deformations, the sum over λ can be truncated to include only the $\lambda = 2$ term and then the approximation of the radius as a function of angle is is [Str67]

$$R(\theta, \phi) = R(\theta) = R_0 \left[1 + \alpha_2^0 \sqrt{\frac{5}{16\pi}} (3\cos^2\theta - 1) \right]. \quad (2.6)$$

There are at least three common symbols in use to describe the deformation of a nucleus. The first is β_2 , which, if we take the definition of the radius as given in equation 2.6, is simply equal to the coefficient α_2^0 . β_2 is related to the long and short axes of the ellipsoid, a and b respectively, by

$$\beta_2 = \frac{4}{3} \sqrt{\frac{\pi}{5}} \frac{(a-b)}{R_0}. \quad (2.7)$$

The second symbol to discuss is δ , which is defined as [FSB⁺96]

$$\delta = \frac{(a-b)}{R_0}. \quad (2.8)$$

Clearly δ and β_2 have a simple relationship:

$$\beta_2 = \frac{4}{3} \sqrt{\frac{\pi}{5}} \delta. \quad (2.9)$$

The final symbol in common usage is the Nilsson quadrupole deformation parameter, ε_2 . A plot mapping the effect of deformation on the energies of nuclear orbitals is shown in figure 2.1. ε_2 can be defined as an expansion around $\delta = 0$ as [Löb70]

$$\varepsilon_2 = \delta + \frac{1}{6} \delta^2 + \frac{5}{18} \delta^3 + \frac{37}{216} \delta^4 + \dots \quad (2.10)$$

The values of β_2 , δ , and ε_2 for some long axis to short axis ratios of interest are given in table 2.1.

2.1.3 Triaxiality

There is, of course, no reason for the nucleus to restrict its deformation to the β variable. Triaxiality is a well-known trait of nuclei. A triaxial shape has three distinguishable axes, like a kiwi fruit. Because there is no way to measure triaxial deformation via heavy-ion fusion reactions the analysis in this thesis will primarily make the simplifying assumption that there are two identical axes in all deformations determined by measurement.

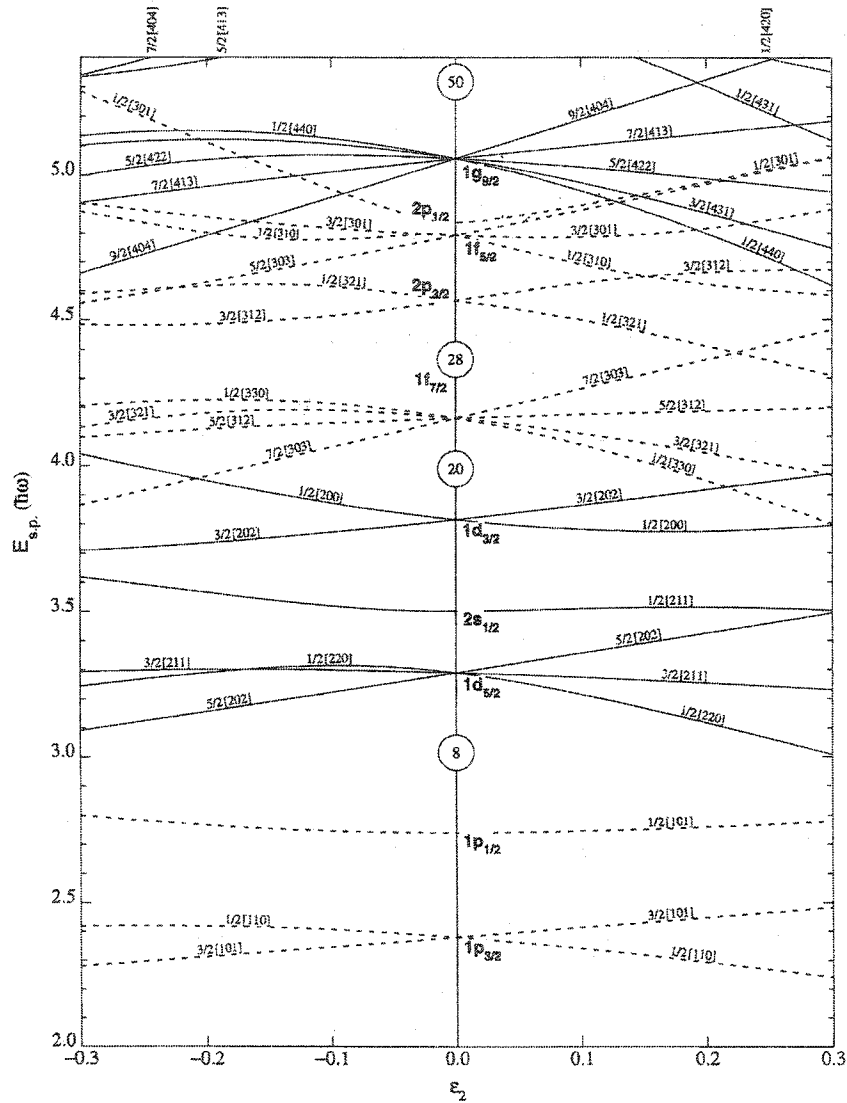


Figure 2.1: Potential Energy of Orbitals Varying with Deformation
 This is a Nilsson diagram. The energy of orbitals may increase or decrease with changing deformation. This means that a nucleus with a single unpaired nucleon in the $1d_{5/2}$ level will have a lower ground state energy if it is deformed. From [FSB+96].

a : b	β_2	δ	ε_2
2 : 1	$\sqrt{\pi/5}$	3/4	0.90
5 : 3	$\sqrt{64\pi/605}$	6/11	0.66
3 : 2	$\sqrt{16\pi/245}$	3/7	0.49

Table 2.1: Some Values of Deformation Parameters

The values of the deformation parameters β_2 , δ , and ε_2 are given for a number of different regimes of superdeformation.

2.2 Superdeformation

Just as the nuclear potential favours deformed shapes for inter-shell nucleon numbers, it may also favour deformation when the nucleus is endowed with high angular momentum. If the angular momentum is sufficiently high, the deformation may be pushed to an extreme ellipsoid with a major-to-minor axis ratio of 3:2, 5:3, or even 2:1. This is called superdeformation. Real nuclei will have non-integer axis ratios.

Figure 2.2 illustrates the changing nuclear potential with increasing deformation, up to the point of fission. The historical image of the dependence of the potential on deformation is represented by the dotted line. Our current understanding of the second well is shown by the solid line in the figure.

Superdeformation was first theorized by Strutinsky [Str67] as an explanation for some very short-lived spontaneous fissions [Pol62]. The first superdeformed bands were observed in the mid-1980's by Peter Twin and his collaborators [Nya84, Twi85]. That superdeformed band, the spectrum of which is shown in figure 2.3, is typical of the superdeformation observed in heavier nuclei. The band has the attributes of a simple description of a rigid rotor.

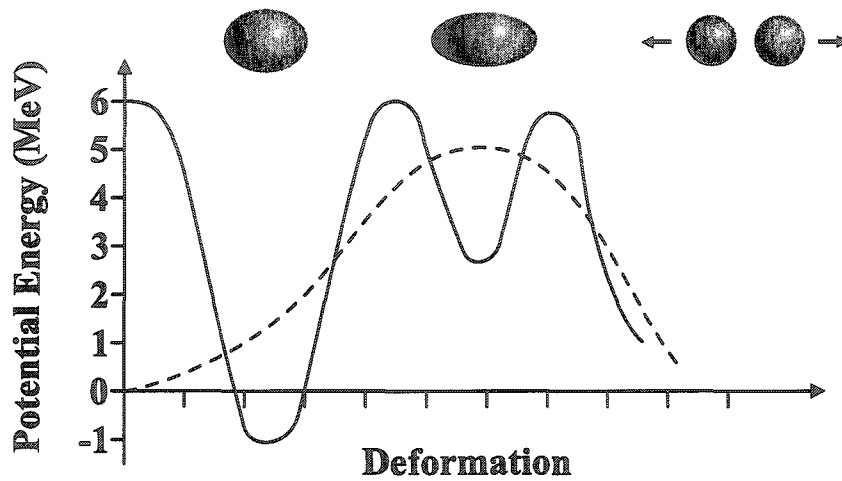


Figure 2.2: The Superdeformed Minimum

A schematic of the minimum in potential energy at superdeformation between normal deformation and fission is shown for a high-mass example ([Has98], adapted from [PB75]). The dashed line indicates what the predicted shape of the potential energy was before superdeformation was theorized. The superdeformed minimum is also known as the second well to distinguish it from the first potential energy well at normal deformations. Superdeformed states are usually then connected to the normal deformed states by tunnelling transitions.

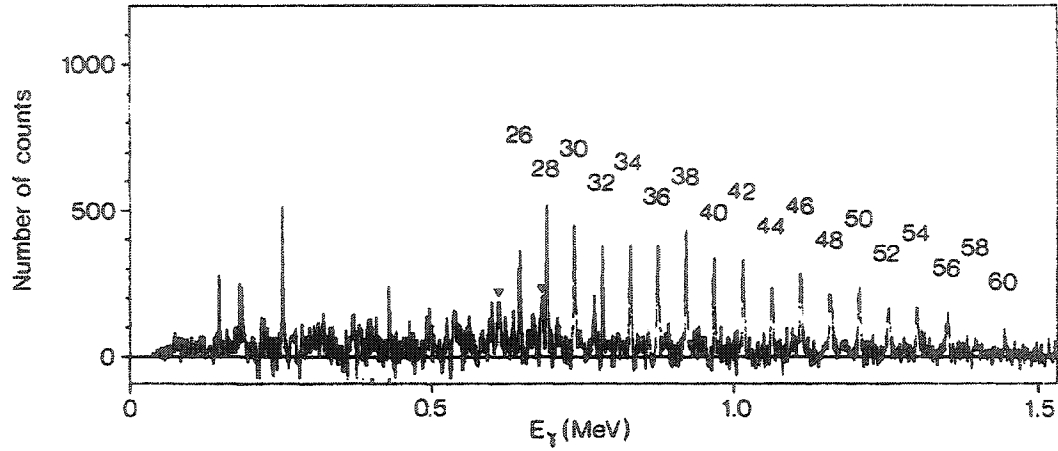


Figure 2.3: Superdeformed Band in ^{152}Dy

The superdeformed band in ^{152}Dy is shown [Twi86]. The regular spacing of the peaks indicates a rotational band, and the actual amount of the interval can be used to determine the moment of inertia of the band according to equation 2.13.

Classically, a rigid rotor has kinetic energy E associated with its motions

$$E = \frac{1}{2} \frac{I^2}{\mathcal{J}}. \quad (2.11)$$

The quantum mechanical equivalent of that * is

$$E = \frac{\hbar^2 I(I+1)}{2 \mathcal{J}}. \quad (2.12)$$

And this is very convenient, indeed, because it implies that the γ -ray energies, E_γ , are evenly spaced (when the moment of inertia is unchanging) and only dependent on the moment of inertia of the rotor:

$$\begin{aligned} E_\gamma(I \rightarrow I-2) &= \frac{\hbar^2}{2\mathcal{J}} (I(I+1) - (I-2)(I-1)) \\ &= \frac{\hbar^2}{\mathcal{J}} (2I-1). \end{aligned} \quad (2.13)$$

*i.e. the eigenvalue of the equation $H\psi = E\psi$ when $H = H_{rotor}$.

In the above equations 2.11, 2.12, and 2.13 the total angular momentum is represented by I and the moment of inertia is represented by \mathcal{J} . This makes the spectra of traditional heavy-nuclide superdeformed bands rather like a picket fence, as in figure 2.3. Furthermore, the regular spacing in E_γ enables a fairly straightforward determination of the moment of inertia (even if it is smoothly varying), the rotational frequency of the nucleus and other relevant parameters.

I have been careful to describe the “picket fence” ideal of superdeformation as traditional and belonging to the region of heavy nuclei. Since its first observation, superdeformation has been mainly understood as a collective effect. While it has always been understood that each nucleon occupies in its own orbital, it has usually been the collective combination of the nuclear orbitals, with the contribution of the individual orbitals largely washed away by the overall effect, to which superdeformation was attributed. That works very well for one hundred nucleons, but in light nuclei individual orbitals cannot be smeared away by the collective whole.

2.3 Nuclear Decays

The lifetime of a state (τ) is the average time the state survives before it decays. This is different from the half-life of the state ($t_{1/2}$), which is the time that passes before that state decays in one half of the nuclei in a sample. The relationship between τ and $t_{1/2}$ is simple:

$$t_{1/2} = \frac{\tau}{\ln(2)}. \quad (2.14)$$

Quantum mechanical decay lifetimes are governed by purely statistical probabilities. This differentiates them from other processes with specific lifetimes where the probability of the process occurring changes over time. Take for example waiting for a

bus: If a bus is scheduled to pass every 45 minutes, a person arriving at the bus stop at a random time and waiting for half an hour without a bus arriving has a greater possibility of having the bus arrive in the next five minutes than does a person who arrives at the bus stop at a random time and waits for 15 minutes without a bus arriving. If bus arrival times were governed by Poisson statistics, like nuclear decays, then the probability of a bus arriving in the next five minutes would not differ, no matter how long a person waited at the stop.

The decay of a collection of unstable nuclei depends only on each individual nucleus' probability of decay. The number of decays observed from a mass of unstable nuclei will vary with the number of unstable nuclei in the sample, N , and the nuclear species' decay probability, λ .

$$\frac{\Delta N}{\Delta t} = -\lambda N(t). \quad (2.15)$$

Although it upsets mathematicians to treat a discrete quantity like a continuous one, it is usually understood that there is an observable $\Delta t \ll \tau$, the lifetime. Under those circumstances, it is fair to integrate and find an equation for the number of unstable nuclei as a function of time, $N(t)$

$$N(t) = N(0)e^{-\lambda t}. \quad (2.16)$$

The number of unstable nuclei at time $t = 0$, $N(0)$ is usually denoted N_0 .

The "activity", A , of the sample is defined as the amount of decays in per time. We have an expression for the activity of the sample:

$$A = \lambda N_0 e^{-\lambda t}. \quad (2.17)$$

But if the number of decaying states is changing because it is being fed in one case

and decaying in another case, as in a cascade, then we get

$$A_n = N_0 \sum_{i=1}^n c_i e^{-\lambda_i t}, \quad (2.18)$$

where the constants, c_m , are

$$c_m = \frac{\prod_{i=1}^n \lambda_i}{\prod_{i \neq m}^n (\lambda_i - \lambda_m)}. \quad (2.19)$$

A detailed discussion of this can be found in [Kra88].

So our first state, which begins with a certain number N_0 , gives off the activity

$$A_1 = N_0 \lambda_1 e^{-\lambda_1 t}. \quad (2.20)$$

But the second state is a little bit trickier because it is being created as the first state decays and then it is being destroyed as it decays, so its activity is

$$A_2 = N_0 \left[\lambda_1 e^{-\lambda_1 t} + \frac{\lambda_1 \lambda_2}{(\lambda_1 - \lambda_2)} e^{-\lambda_2 t} \right]. \quad (2.21)$$

And by the time we reach the sixth transition in the decay chain, the activity is

$$\begin{aligned} A_6 = N_0 & \left[\lambda_1 e^{-\lambda_1 t} + \frac{\lambda_1 \lambda_2}{(\lambda_1 - \lambda_2)} e^{-\lambda_2 t} + \frac{\lambda_1 \lambda_2 \lambda_3}{(\lambda_1 - \lambda_3)(\lambda_2 - \lambda_3)} e^{-\lambda_3 t} \right. \\ & + \frac{\lambda_1 \lambda_2 \lambda_3 \lambda_4}{(\lambda_1 - \lambda_4)(\lambda_2 - \lambda_4)(\lambda_3 - \lambda_4)} e^{-\lambda_4 t} \\ & + \frac{\lambda_1 \lambda_2 \lambda_3 \lambda_4 \lambda_5}{(\lambda_1 - \lambda_5)(\lambda_2 - \lambda_5)(\lambda_3 - \lambda_5)(\lambda_4 - \lambda_5)} e^{-\lambda_5 t} \\ & \left. + \frac{\lambda_1 \lambda_2 \lambda_3 \lambda_4 \lambda_5 \lambda_6}{(\lambda_1 - \lambda_6)(\lambda_2 - \lambda_6)(\lambda_3 - \lambda_6)(\lambda_4 - \lambda_6)(\lambda_5 - \lambda_6)} e^{-\lambda_6 t} \right]. \quad (2.22) \end{aligned}$$

2.4 Quadrupole Moments and Lifetimes

The quadrupole moment is related to the lifetime as follows [FSB⁺96, Ste65]

$$\tau = \frac{1}{1.219 E^5 Q^2 |\langle IK20 | IK \rangle|^2}. \quad (2.23)$$

In the above, the lifetime, τ , is in ps if E is in MeV and Q is in e-fm².

The quadrupole moment determined here is the transition quadrupole moment, which is sensitive only to β deformation. The overall quadrupole moment, Q_{20} , which includes both γ and β deformation is related to the transition quadrupole moment by [Hil53]

$$Q_{20} = \frac{\cos(30^\circ)}{\cos(\gamma + 30^\circ)} Q. \quad (2.24)$$

The deformation parameter β_2 introduced in section 2.1.2 can be extracted from the quadrupole moment

$$\beta_2 = \frac{\sqrt{5\pi}}{3} \frac{Q_{20}}{ZeR_0^2}. \quad (2.25)$$

2.5 Shell Model

The nucleus exhibits closed shell behaviour, much like the atom, or indeed any multiparticle quantum mechanical harmonic oscillator. Proton separation energies, nuclear radii, neutron capture cross sections and many other indicators show either dips or spikes at certain N 's and Z 's. The particular N 's and Z 's corresponding to closed shells appeared at first to follow the multiparticle quantum mechanical harmonic oscillator shells, but then diverged after $N, Z = 20$. The puzzle was solved by Maria Göppert-Meyer, who introduced a spin-orbit potential to complete the picture of the closed shells.

The orbitals are described in a similar way to atomic orbitals, with s, p, d, f, g, \dots signifying

$$\ell = 0, 1, 2, 3, 4, \dots, \quad (2.26)$$

The shorthand for nuclear orbitals is

$$n\ell_j, \quad (2.27)$$

and I will indicate the number of nucleons, nn , in the orbital as follows

$$(n\ell_j)^{nn}. \quad (2.28)$$

The principal quantum number is n ; it counts the number of ℓ orbitals which have passed before and adds 1. The quantity ℓ is the orbital angular momentum, to which the nucleon spin of $\frac{1}{2}$ is added to make total nucleon angular momentum $j = \ell \pm \frac{1}{2}$. The number of nucleons an orbital can support is $2j+1$. The projection of the angular momenta of each nucleon in an orbital with angular momentum j will be between $j\hbar$ and $-j\hbar$. In this thesis, where necessary, I will follow the common convention that each individual nucleon total angular momentum is represented by a lower-case j , and the total angular momentum of the nucleus is represented by an upper-case I . Nuclear structure physicists further confuse the issue by referring to the total nuclear angular momentum as “spin”. Confusing though it is, I have made it a habit and it will permeate this thesis as it permeates the field.

The first thirty-two nucleons, when the nuclear potential is un-deformed, fill orbitals in the following order

$$\left(1s_{\frac{1}{2}}\right)^2 \parallel \left(1p_{\frac{3}{2}}\right)^4 \left(1p_{\frac{1}{2}}\right)^2 \parallel \left(1d_{\frac{5}{2}}\right)^6 \left(2s_{\frac{1}{2}}\right)^2 \left(1d_{\frac{3}{2}}\right)^4 \parallel \left(1f_{\frac{7}{2}}\right)^8 \parallel \left(2p_{\frac{3}{2}}\right)^4, \quad (2.29)$$

where I have marked shell gaps with a \parallel .

The crux of the shell model is the assumption that the bulk nuclear behaviour can be described as a product of the behaviour of individual nucleons in their shell

model orbitals. That means that the angular momentum of the nucleus, j is the sum of the individual nucleon angular momenta, j_i ,

$$j = \sum_{i=1}^A j_i. \quad (2.30)$$

The parity of each nucleon, π_i , depends on the angular momentum of the orbital in which that nucleon resides

$$\pi_i = (-)^{\ell_i}. \quad (2.31)$$

The parity of the nucleus is then a product of the parities of the individual nucleons

$$\pi = \prod_{i=1}^A \pi_i \quad (2.32)$$

or

$$\pi = (-)^{\sum_{i=1}^A \ell_i}. \quad (2.33)$$

The result of equation 2.33 is that no nucleon which is paired contributes to the total parity (since double anything is even).

It is also an axiom of the shell model that any filled orbital will contribute nothing, since the nucleons occupying that orbital will have the angular momentum projections

$$m_{j_i} = j, j-1, \dots, -j \quad (2.34)$$

and the sum of all those projections will be zero, as enforced by Pauli's exclusion principle.

2.5.1 Particle-Hole Configurations

A convenient way to describe configurations is by the number of particles excited across a certain gap. In the mass region examined here, the gap is the one at $N, Z =$

20. Theorists who truncate the valence space beyond the $2p_{\frac{3}{2}}$ orbital and assume that there is an inert filled core up to the $1d_{\frac{5}{2}}$ orbital would call this the “sd-pf” gap. The only active orbitals in this description are

$$(1d_{\frac{5}{2}}) (2s_{\frac{1}{2}}) (1d_{\frac{3}{2}}) || (1f_{\frac{7}{2}}) || (2p_{\frac{3}{2}}). \quad (2.35)$$

To give a complete description of the configurations, it is useful to include the number of holes effectively crossing the gap, as well. Of course, that number is predetermined by the number of excited particles and the number of particles available. The particle-hole configuration picture provides us with a straightforward shorthand for comparing bands in different nuclei.

Of course, this picture of discrete occupation is convenient for those of us used to thinking in the classical world, but the nuclear regime is more flexible. One should, strictly speaking, be discussing “average” occupations of orbitals, as a reflection of the fact that nucleons in orbitals are not billiard balls in pockets. Rather, nuclei consist of quantum mechanical wave packets of nucleons, each of which possesses probabilities of being excited to the energies of the orbitals. Sometimes this flexibility manifests itself in discussions of “quasiparticles”. It is important to bear in mind that this wavefunction picture underlies the billiard-ball picture, which I will use for the remainder of the thesis.

2.6 Mixing

The pure states will be mixed by residual interactions, which can cause an adjustment to their energies. The Dirac representation of mixing between states A and B is

$$\langle \psi_A | \mathcal{O}_{AB} | \psi_B \rangle \quad (2.36)$$

where \mathcal{O} can be thought of as an “overlap operator”.

For a γ transition between two states to be probable within a finite amount of time, there needs to be some overlap in the configurations of the states. “Fermi’s Golden Rule” mathematically expresses the idea that the probability of a decay (once again represented here by λ) is proportional to the overlap between the two states and the density of final states (written below as ρ_B):

$$\lambda = \frac{2\pi}{\hbar} |\langle \psi_A | \mathcal{O}_{AB} | \psi_B \rangle|^2 \rho_B. \quad (2.37)$$

As was mentioned in section 2.2, there is not, in the traditional heavy-nuclide version of events, a strong overlap between superdeformed and normal deformed states. However, in the light nuclei, there can be orbitals which are very closely related between the normal deformed states and the superdeformed states.

In some ways, the fact that the superdeformed and normal deformed states are intermixed is useful. Traditional heavy-nuclide superdeformation is difficult to observe because feeding to the superdeformed states is often on the order of a hundredth or a few thousandths of the feeding of the normal deformed states. Because the superdeformation states in ^{38}Ar are close to the normal deformed states in level space, the highly deformed bands are quite intense, with some transitions visible in the total projection! However, the “picket fence” signature of superdeformation is sacrificed, and the quadrupole moment *must* be measured (through the lifetimes) to determine the deformation of the bands.

Chapter 3

Experiment

3.1 GSFMA93

To produce the nucleus discussed in this work, an 80 MeV beam of ^{20}Ne was impinged on a ^{24}Mg target. The beam was delivered by the operators at ATLAS into the target at the joint center of the MICROBALL and GAMMASPHERE detector arrays. The reaction produced ^{44}Ti ,



which then evaporated one α particle and two protons to reach the nucleus of interest here.



The experiment was designated “GSFMA93”, and it will occasionally be referred to as such in this work.

Two different targets were used. One was a thin self-supporting magnesium

foil $440 \mu\text{g}/\text{cm}^2$ thick and the other was $420 \mu\text{g}/\text{cm}^2$ of magnesium mounted on a $11.75 \text{ mg}/\text{cm}^2$ gold backing*.

3.2 Heavy Ion Fusion-Evaporation Reactions

To observe excited states of nuclei, it is necessary to put nuclei into those excited states. One way to affect this is through heavy ion fusion evaporation reactions.

Heavy ion fusion-evaporation reactions begin with a beam of projectile ions accelerated onto a target. The frequency with which an ion in the beam interacts with an atom in the target is determined by the intensity of the beam, the density and thickness of the target, and the reaction cross section. If the projectile carries sufficient energy to overcome the Coulomb repulsion between the positively charged protons in the projectile and the target, then the two nuclei may fuse. Very quickly (on a time scale of approximately 10^{-19} s) the nucleons of the once separate nuclei will thermallise and the compound system will be formed. In a thermallised nucleus, all of the nucleons are at the same temperature; they retain no signature of the nucleus they originated in (projectile or target).

The compound system may fission before or immediately after thermallisation, if there is so much angular momentum or excess energy in the reaction that it is impossible for the nucleus to remain intact. In fusion evaporation reactions, the excess angular momentum of the system should not be sufficient to cause the compound nucleus to fission. Instead, the hot, rotating nucleus de-excites by releasing light particles such as protons, neutrons and α particles, followed by γ rays.

*A $\mu\text{g}/\text{cm}^2$ is a unit of thickness used by scientists who are more concerned with the stopping power of a material than its actual extent in space. $440 \mu\text{g}/\text{cm}^2$ of magnesium is approximately $2.6 \mu\text{m}$ thick. Or, for those of an even more esoteric bent, it is approximately 3 stone/acre

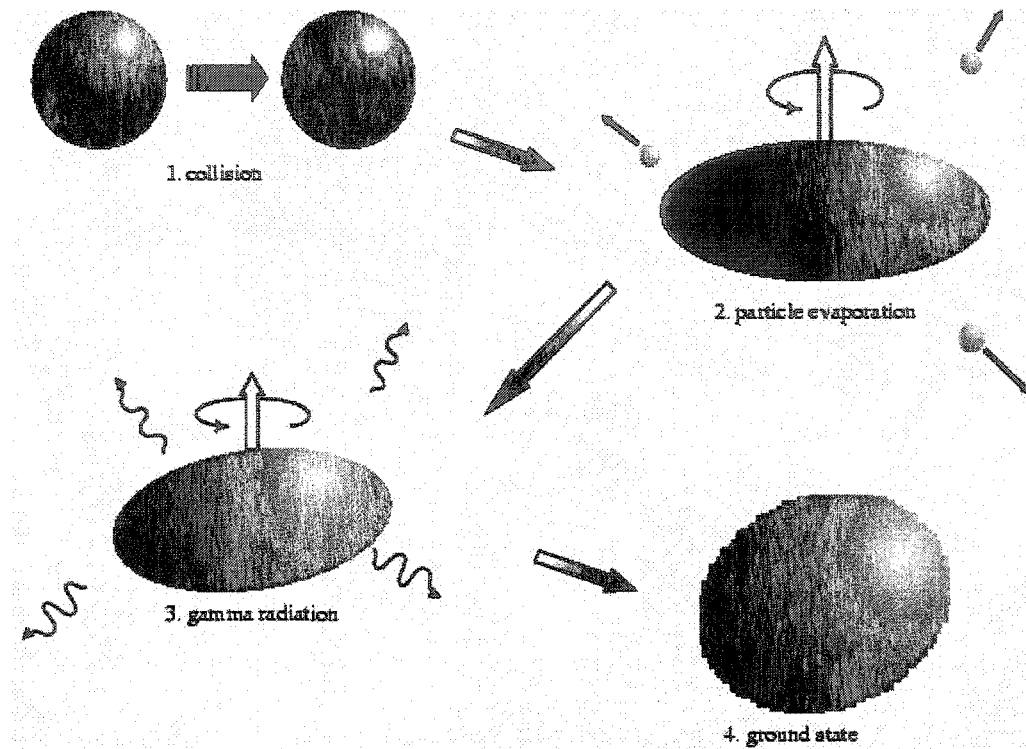


Figure 3.1: Heavy Ion Fusion-Evaporation Reactions

The projectile collides with the target atom. Particle evaporation occurs, beginning to cool the hot, rotating nucleus. When the excess energy is sufficiently reduced, the residual nucleus cools by γ -ray emission to the ground state.

As is illustrated in cartoon form in figure 3.1, the projectile fuses with the target and the two then thermallise into the high-energy, high-spin compound system. Particles evaporate from the compound system, carrying away excitation energy and angular momentum. Eventually the system reaches an energy where particle evaporation is no longer viable, after which the residual nucleus de-excites to the ground state through γ -ray emission (and internal electron conversion).

Another way to visualise this process is given in figure 3.2. The compound system is formed in the lightly shaded region on the top of the figure where the

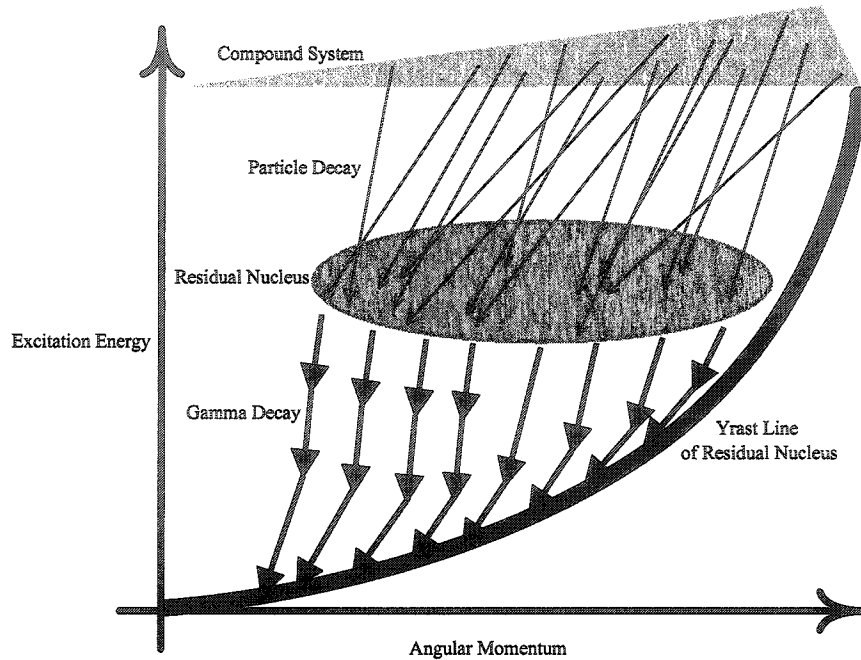


Figure 3.2: Feeding of the Residual Nucleus

The residual nucleus is fed by particle decay to a broad region of continuum states above the yrast line. The particle decay is followed by statistically distributed in energy γ decays in the continuum. Eventually, the level density decreases and the residual nucleus de-excites to the ground state by γ decays through discrete states near and on the yrast line. Adapted from [Dia80]

excitation energy is high. The range in energy of that region is determined by the range in energy of the beam. The maximum angular momentum of the compound system is, by a first order approximation, determined by the impact parameter of the collision that formed the system. Higher order effects may, for example, depend on the angular momentum of the projectile, or the shapes of the reactants. The maximum angular momentum for a given energy is called “yrast” (old Swedish for “dizziest”). The yrast line equivalently marks the minimum possible excitation energy for each spin, and it is in this context that the term is most frequently used.

The compound system is formed in a very excited state. The fastest and most efficient way for it to dissipate that surplus energy, along with some excess angular momentum, is by the emission of light particles. A wide range of particle energies leads to a wider range of energies in the feeding of the residual nucleus. In figure 3.2 the feeding of the residual nucleus is indicated by the darker region near the middle of the figure. From that region, the lifetimes for γ decays to continuum states are very short, shorter than those for particle decay. The nucleus de-excites by statistically distributed in energy γ rays between continuum states until the level density is low enough to accommodate discrete transitions between discrete states. It is those discrete γ rays that are used in this thesis to resolve the structure of the nucleus.

Figure 3.2 shows the most common mechanism for the feeding of the residual nucleus. In section 4.2.1 a description of a less common feeding mechanism, observed in this experiment, is given.

3.3 Detecting γ Rays

Photons outside of the visible range must be detected through their interaction with matter. Electromagnetic radiation (as γ rays are) scatters off charged particles in a process called Compton scattering. The lightest, most common, and most loosely bound charged particle available to experimenters is electrons. Interaction between a γ ray and an electron requires the γ ray to pass reasonably close to the electron, which implies that substances dense in electrons make good detectors of γ rays. One way to create a high density of electrons is to create a dense crystal, with atomic sites close together. Another way to attain density of electrons is to use high-Z materials.

The more scattering centres per volume there are, the less material overall will be necessary.

Of course, there are other considerations to take into account. The material must be capable of transmitting something meaningful about the interaction which disturbed its electrons through to its edges (where electronics can pick up the information). This makes pure, single crystals desirable as detectors. If the information about the interaction comes in the form of emitted light (rather than current, for example) then it is obviously imperative that the crystal be transparent to that wavelength. If the information about the interaction comes in the form of current, then it is clearly an advantage to have a band gap of small enough energy to make the detector have a very high sensitivity to the radiation it will detect.

Germanium Detectors

Germanium is a semiconductor with a band gap of about 0.7 eV. Radiation in the form of γ rays can scatter off electrons in the crystal, exciting them to the conduction band. Further conduction electrons are produced as the electrons slow in the material. This accumulation of charge is eventually collected on terminals surrounding the crystal. The amount of charge collected is proportional to the amount of energy deposited in the crystal by the scattering γ ray. The technology of germanium detectors has advanced since the first Ge detectors were used for γ -ray spectroscopy [Ewa64] and now the standard detectors are formed from high-purity germanium crystal (HPGe), also referred to as intrinsic germanium. A detailed description of the workings of Ge detectors can be found in, for example [Kno89, Leo87].

Since the band gap in germanium is so low, at room temperature ordinary

thermal excitations would produce a constant current through the detectors. For this reason, the crystals are kept cooled with liquid nitrogen to reduce background noise.

It is possible for high-energy neutrons resulting from heavy ion fusion evaporation reactions to displace atoms from the crystal lattice. This will reduce the energy resolution of the detector, since some current may get “trapped”, or at least delayed beyond the time window of the electronics. The result of that action is that sometimes the detector registers less energy than it should (because some of the charge from the interaction does not reach the electronics in time) and occasionally the detector registers more energy than it should (because some charge left over from previous interactions finally makes it to the electronics, but is recorded during a later event rather than the one from which it originated). The experimental signal for neutron damage is wide tails on peaks in the single-detector spectrum. Neutron damage to the crystal may be repaired through annealing.

Bismuth Germanate Detectors and Compton Suppression

Now and again, a γ ray will enter a germanium detector and Compton scatter out of the crystal, leaving only a portion of the total γ -ray energy in the detector. Thus when the detector only measures a fraction of the total energy of the γ ray, this produces a background below the photopeaks. The result in a spectrum of many events taken over time is a narrow peak from all the events where the full energy was deposited in the germanium crystal combined with a wide smear at lower energy from all of the partially-deposited γ rays, as in the top trace of figure 3.3.

Bismuth Germanate (BGO) is a scintillating crystal of high density. It has excellent time resolution, but its energy resolution is not up to the standards set by

HPGe.

Although BGO can be used to gather energy information, because it has inferior energy resolution, its primary purpose in modern arrays is as a device for Compton suppression.

If a germanium detector is surrounded by BGO, then when a γ ray scatters out of the HPGe, it will usually scatter into the BGO and leave some or all of what remains of its energy there. The density of BGO is such that a relatively thin shell around the HPGe detectors is all that is required to provide a veto for events in which a γ ray has scattered out of the HPGe crystal, which is exactly what is meant by Compton suppression. This gives it an added advantage over other scintillation detectors (such as NaI) because it allows suppressed HPGe detectors to be close-packed.

The experimenter is then given two advantages from the presence of the BGO. One is that any event where both a HPGe and its surrounding BGO fired can be labelled as one where not all the energy was collected in the HPGe and can therefore be suppressed. The second advantage is that the total energy is still collected, albeit with lower resolution than if the array were a solid shell of HPGe. The total energy is useful, especially for the total energy plane method [Sve97] described in section 4.2.

In practical terms, Compton suppression is not perfect. As can be seen in figure 3.3, not all of the energy is in the photopeak for every event, even when a Compton suppressor is used. Some γ rays will scatter through the BGO without interacting at all, since the BGO shields, while dense, are of finite thickness. The result of this effect is discussed in section 4.3.

There may also be a characteristic hump in spectra at ~ 255 keV, which arises from those events in which the γ ray scatters at 180° (for example, back out the front

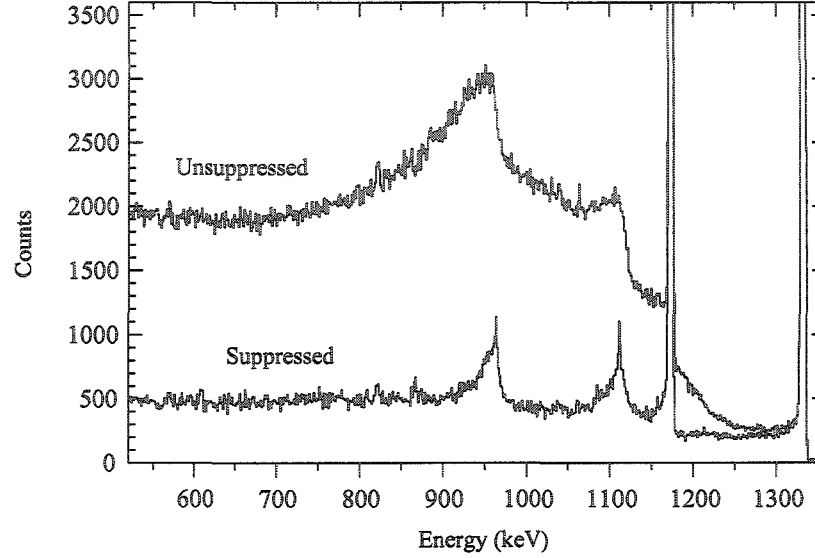


Figure 3.3: Compton Suppression

Spectra of a ^{60}Co source from one GAMMASPHERE HPGe detector. The “suppressed” spectrum has the Compton suppression on, and the “unsuppressed” spectrum does not. The two spectra are normalised to have the same height of the photopeaks, which are cut off to enable a clear view of the benefits of Compton suppression. (From [Sve97].)

opening of the detector). The energy, E_{γ}^{scat} , of the scattered γ ray is given by [Kno89]

$$E_{\gamma}^{\text{scat}} = \frac{E_{\gamma}}{1 + \left(\frac{E_{\gamma}}{m_e c^2}\right) (1 - \cos \theta)}, \quad (3.3)$$

where $m_e c^2$ is the equivalent energy of the rest mass of an electron, and θ is the scattering angle. If the scattering is back out the front of the detector into its partner opposite and E_{γ} is very large, we can approximate equation (3.3) to be

$$E_{\gamma}^{\text{scat}} \approx \frac{m_e c^2}{2}. \quad (3.4)$$

That is responsible for creating a wide peak in the spectrum at ~ 255 keV.

3.3.1 Electron-Positron Pair Production

Another source of rogue peaks in the spectrum is escape peaks. If a γ ray has more than twice the mass energy of an electron, it is possible for that γ to create an electron-positron pair. The annihilation of the positron by an electron generates two γ rays of 511 keV travelling in opposite directions to each other. They enter the detector array and are then Doppler-corrected offline, resulting in a wide self-coincident peak at 511 keV. (For more on Doppler correction, see section 4.4, particularly equation 4.4.) The 511 keV peak is sharp in un-Doppler-corrected spectra.

It also happens that the positron-electron annihilation occurs inside the germanium crystal, and only one of the two photons is captured. The result is sharp peaks in the spectrum at 511 keV (or 1022 keV) less than the energy of the real γ ray, as is shown in figure 3.4. That single-escape γ ray will be in coincidence with all the same γ rays as the original γ ray.

3.3.2 The GAMMASPHERE Detector Array

The experiment which produced the results described in this thesis was performed with the GAMMASPHERE array [Lee90]. GAMMASPHERE consists of 110 HPGe detectors arranged in 17 rings perpendicular to the beam. Although the alignment of the rings is perpendicular to the beam, each detector is pointing towards the centre of the target. Every HPGe detector is inside a cylindrical shell of BGO, and also backed by more BGO to catch the Compton scattering events. Each HPGe detector is 7.1 cm in diameter and 8 cm in length. The total solid angle covered by HPGe detectors is 47% of 4π .

In the fall of 1997, GAMMASPHERE was moved from the Ernest Orlando

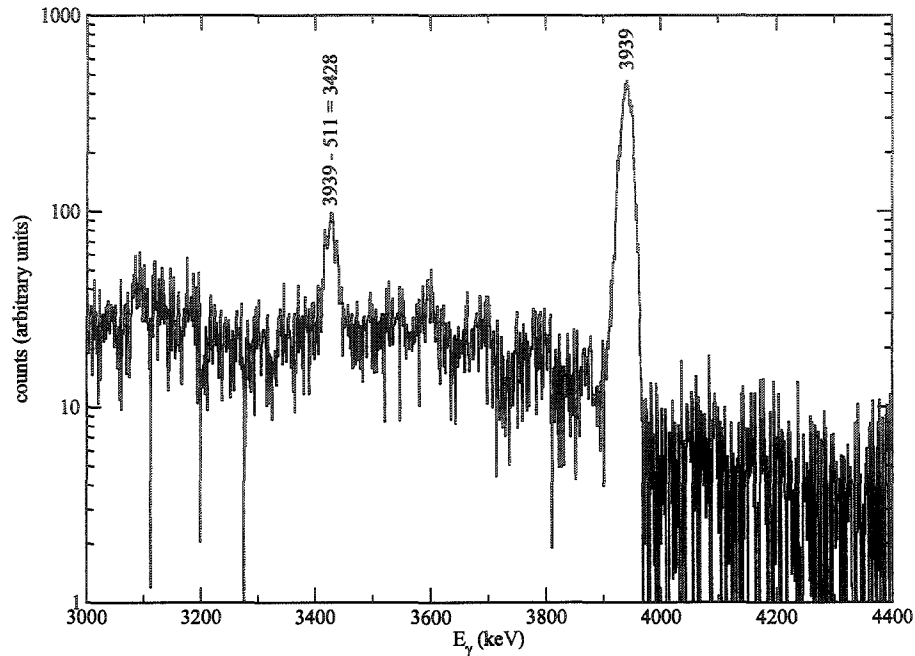


Figure 3.4: Escape Scattering

In this single, background-subtracted gate on the 1414 keV γ ray, the peak at 3428 keV does not arise from a transition in the nucleus, but from the single escape from the 3939 keV transition.

Lawrence Berkeley Laboratory, in Berkeley CA to the Argonne National Laboratory in Argonne, IL. The purpose of the move was to couple the γ -ray detection power of GAMMASPHERE with the mass selection power of the Fragment Mass Analyzer [Dav92]. Coupling the two instruments required the removal of the front ring (at 17°) of GAMMASPHERE, which reduced the total number of HPGe detectors available for this experiment to 101. The Fragment Mass Analyzer was not used for this experiment.

GAMMASPHERE coupled to the Fragment Mass Analyzer at Argonne is shown in figure 3.5. The two hemispheres of the detector are closed around the particle detector (see section 3.4.1) and the target chamber. What is visible in this photograph

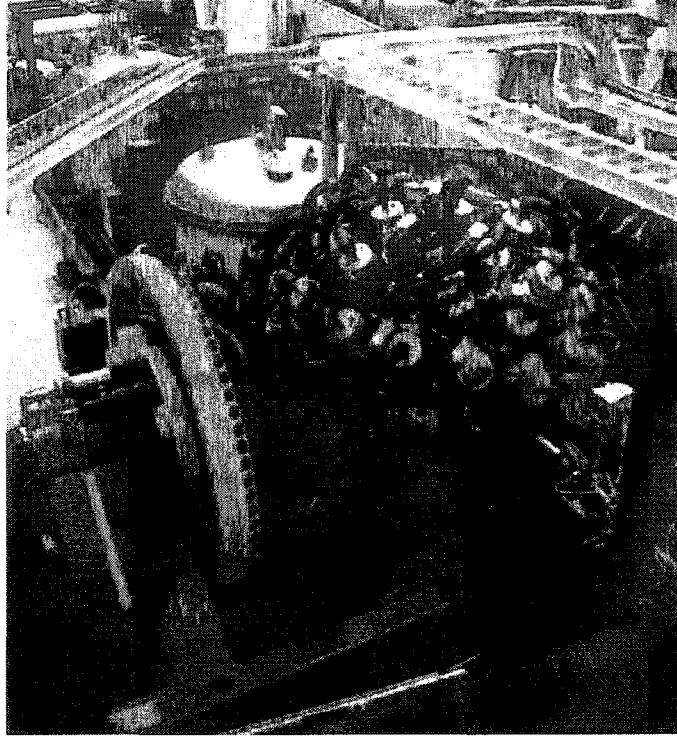


Figure 3.5: GAMMASPHERE at ANL

The closed GAMMASPHERE (foreground) in place next to the Fragment Mass Analyzer (beginning with pale tank behind the GAMMASPHERE) at Argonne National Laboratory. The beam pipe comes up from the bottom right side of the picture. The MICROBALL is enclosed inside, and the target is inside that. (From [Laua].)

are the liquid nitrogen dewars at the end of each detector. For the very curious, it is possible to see in figure 3.5 the mechanism which allows the hemispheres of GAMMASPHERE to rotate about an axis perpendicular to the beam and parallel to the ground. This complicated system makes it convenient to access GAMMASPHERE HPGe detectors, since they can be rotated to an accessible position. The benefit of this system (which requires complexity in the feeding of the liquid nitrogen and electronics) is that it makes it possible to install GAMMASPHERE in tight spaces.

A photograph of some of an open hemisphere of GAMMASPHERE is shown

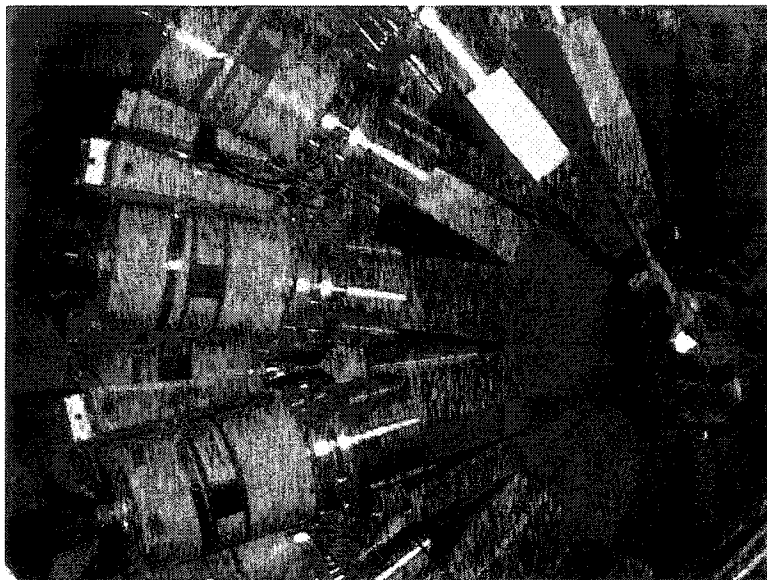


Figure 3.6: GAMMASPHERE Detectors

Some GAMMASPHERE detectors. The array opens into two hemispheres, of which this is a photograph of slightly more than one quarter. The liquid nitrogen dewars with electronics strapped to them can be seen. The cans of the BGO shields are also clearly visible. (From [Fal].)

in figure 3.6. The sides of the tapered hexagonal-cylinder-shaped BGO shields are visible. The central hollow, into which goes the target and any internal auxiliary detectors, can be seen. The diameter of that space is 50.5 cm [Lee90]. A reflection of the camera's flash is visible in the center of the right side the picture. That is a reflection off an absorber in front of a single HPGe and BGO shield unit, which gives a sense of the size of the detector opening relative to the array.

3.4 Detecting Charged Particles

Charged particles interact with bulk matter through electromagnetic interactions, like γ rays. However, since they are massive, and usually more energetic than the γ rays

of interest in heavy ion nuclear reaction experiments, charged particles are usually detected by means other than γ rays. Charged particles have very different ionising powers than photons, and it is the ionising powers of the charged particles that are used to distinguish different particles.

3.4.1 The MICROBALL Detector Array

Charged particles were detected using the MICROBALL array [Sar96]. The MICROBALL consists of 97 CsI(Tl) detectors, arranged in 9 rings perpendicular to the beam. The MICROBALL covers a solid angle $\sim 97\%$ of 4π and was mounted inside GAMMASPHERE.

Crystal excitations in CsI have two different decay times (one fast and one slow), and it is that fact which makes it useful to distinguish types of charged particles [Kno89]. The excitation created when an α particle is stopped in the crystal de-excites more by the fast decay time than by the slow decay time. Protons have a lower ionising density than α particles and therefore the excitations caused by proton-CsI interactions de-excite more by the slow decay. Hence, for proton interactions, the total time for light collection in the photodiodes is longer than it is for α particle interactions. The time of collection can then be used to distinguish between protons and α particles. Of course, other light charged particles entering the crystal will have different ionizing powers and they too will be distinguishable.

Figure 3.7 shows the MICROBALL inside one half of the vacuum chamber that houses it inside GAMMASPHERE. The MICROBALL is very carefully constructed to have the same angles as GAMMASPHERE detectors. Also, the rings are arranged to be slightly overlapping to reduce the probability of particles escaping undetected (i.e. to

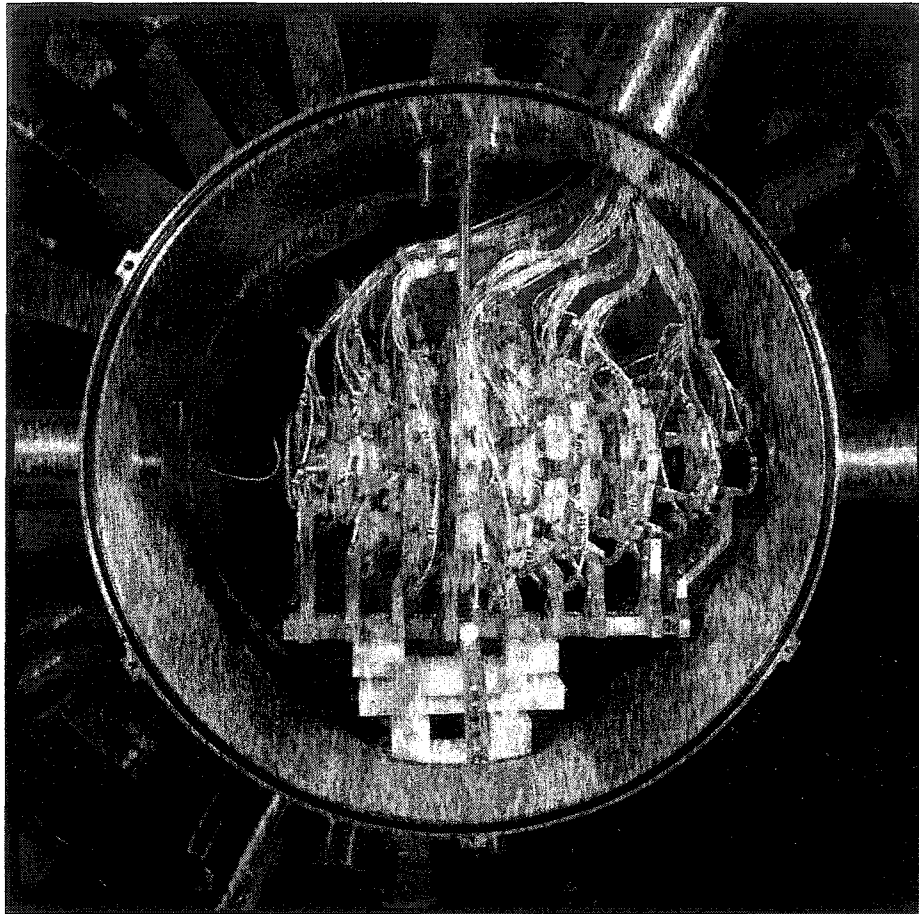


Figure 3.7: The MICROBALL

The MICROBALL inside GAMMASPHERE. One hemisphere of the vacuum chamber has been removed to enable this view. GAMMASPHERE detectors are visible in the background. The target sits in the center of the MICROBALL, suspended from above by the rod visible in the picture. The beam travels from left to right in the photograph, through the pipe shown. (From [Sar].)

increase the total solid angle coverage). The MICROBALL is front-back asymmetric, which is clearly visible in figure 3.7. The front rings have more segmentation (i.e. more CsI crystals per area) than the back. This is because heavy-ion fusion evaporation reaction kinematics favour forward-going particles, and higher segmentation provides

increased sensitivity.

3.5 Accelerating Projectiles

The acceleration of projectiles can be accomplished in many different ways. There are linear accelerators, cyclotrons, tandem accelerators and clever combinations of and variations on all three. Although it is possible to move neutral atoms with laser pulses, the energies required for heavy-ion fusion evaporation reactions are achieved by accelerating charged ions across potential differences.

3.5.1 ATLAS

This experiment was performed at the Argonne Tandem Linear Accelerator System (ATLAS) [Bol93]. ATLAS consists of an FN-type tandem accelerator or a electron cyclotron resonance ion source with a booster linear accelerator coupled to a superconducting radiofrequency linear accelerator. The linear accelerator resonators are constructed of pure niobium operating at liquid helium temperatures.

ECR sources

Large numbers of atoms may be ionized to reasonably high charge states using electron cyclotron resonance (ECR) ion sources. An oven releases a gas of atoms into the ECR chamber. The ECR chamber is filled with a plasma, in which free electrons are exposed to microwaves. The microwaves are tuned to the cyclotron frequency of the electrons (which are inside a magnetic field) which guarantees constant motion of the electrons. Collisions between the vapour and the electrons in the plasma free electrons from the atomic vapour. By the time the vapour reaches the far side of the ECR chamber, it will be multiply positively charged.

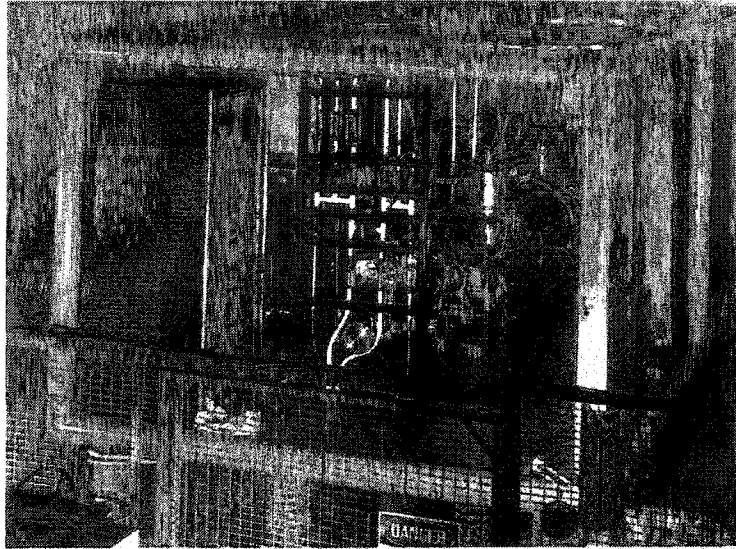


Figure 3.8: ATLAS Electron Cyclotron Resonance Ion Source
The ECR source at ATLAS, inside a high-voltage platform, is shown. The atoms become positively charged when their atomic electrons are removed in collisions with a plasma of fast-moving free electrons. From [Laub].

Linear Accelerators

Linear accelerators move ions by sending cunningly alternating currents to sections of pipe such that the ion is always being pushed to the next section. This requires having pipe sections of different lengths carefully calculated to be exactly the distance the ion will travel in the time between polarity changes.

While room temperature linear accelerators historically used coupled resonating cavities, when superconducting linear accelerators were developed, they were made with each resonator standing alone. This has one very practical advantage (among various theoretical ones) that if one resonator is not operational the rest can still be used and the linear accelerator will still work.

A linear accelerator beam is not continuous, instead it arrives in short pulses

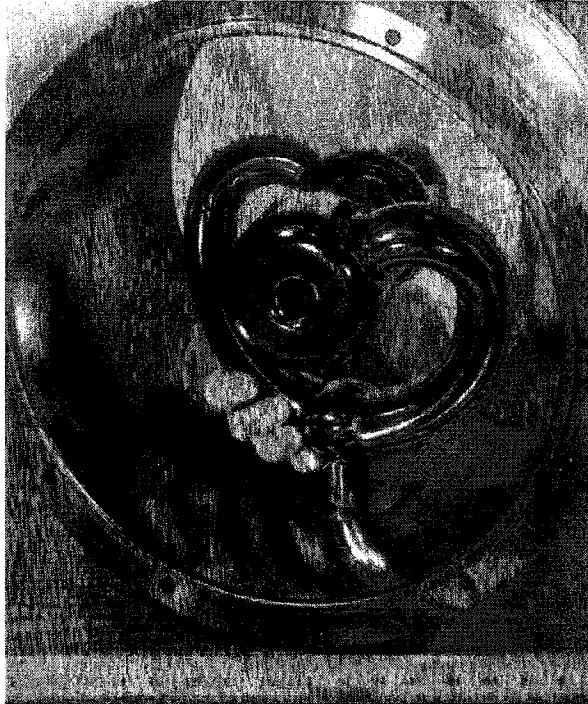


Figure 3.9: Linear Accelerator

A pure niobium superconducting resonator from ATLAS. From [Laub].

called bunches. A neat trick of linear accelerators is to have the phase of the resonator adjusted such that the point of maximum voltage is shortly *after* the bunch enters the accelerating gap. This causes ions that arrive early to experience less acceleration than the majority. Ions that arrive late experience more acceleration than the majority. The slow ones get a greater kick to put them back in the pack and the fast ones are only given sufficient energy to bring them up to the speed of the pack. In this way, the bunches are tightened at each accelerating gap.

A detailed description of superconducting linear accelerators and ATLAS in particular can be found in [Bol86].

3.6 Experimental Considerations

It is hardly necessary to mention that nothing ever goes perfectly; I will outline some of the experimental considerations particular to the circumstances of this experiment.

3.6.1 Contamination

During the course of GSFMA93, it was necessary to monitor the data for contamination from impurity built up on the target, mainly silicon and carbon, constituents of greases used in the vacuum system. The contamination manifested itself as a reduction in energy or widening of the total energy peak caused by the degradation of the beam energy as the impurities accumulated on the upstream face of the target.

This obstacle was overcome by occasionally moving the target slightly (a matter of one or two millimetres up or down) so as to expose a fresh part of the target to the beam. Because the thickness of the target has an impact on the calculations of lifetimes, it was important to keep the uncertainty introduced by this contamination lower than the uncertainty in the thickness of the target as it arrived from the target-maker's bench. This uncertainty is explored in great detail in section 4.5.3

Magnesium metal oxidises very easily, so the amount of contact between the target and air was kept to a minimum. Any oxidation of the target is easily detected in the form of products of the reaction



These products were not observed.

Since the total energy of the reaction in equation 3.5 is quite different from the total energy of the uncontaminated reaction in equation 3.1, it is unlikely that

there was much danger of target oxidation hindering analysis of ^{38}Ar events. However, increased particle emissions and fission events from the reaction in equation 3.5 during the experiment would have limited the rate of data taking, so it was still very important to ensure that no oxide built up on the target face.

Chapter 4

Analysis

Once the data have been obtained they are sifted through and interpreted. The techniques of resolving the gathered material into understandable quantities are described in this chapter. The specifics of the analysis leading to the determination of lifetimes are given in detail later in the chapter.

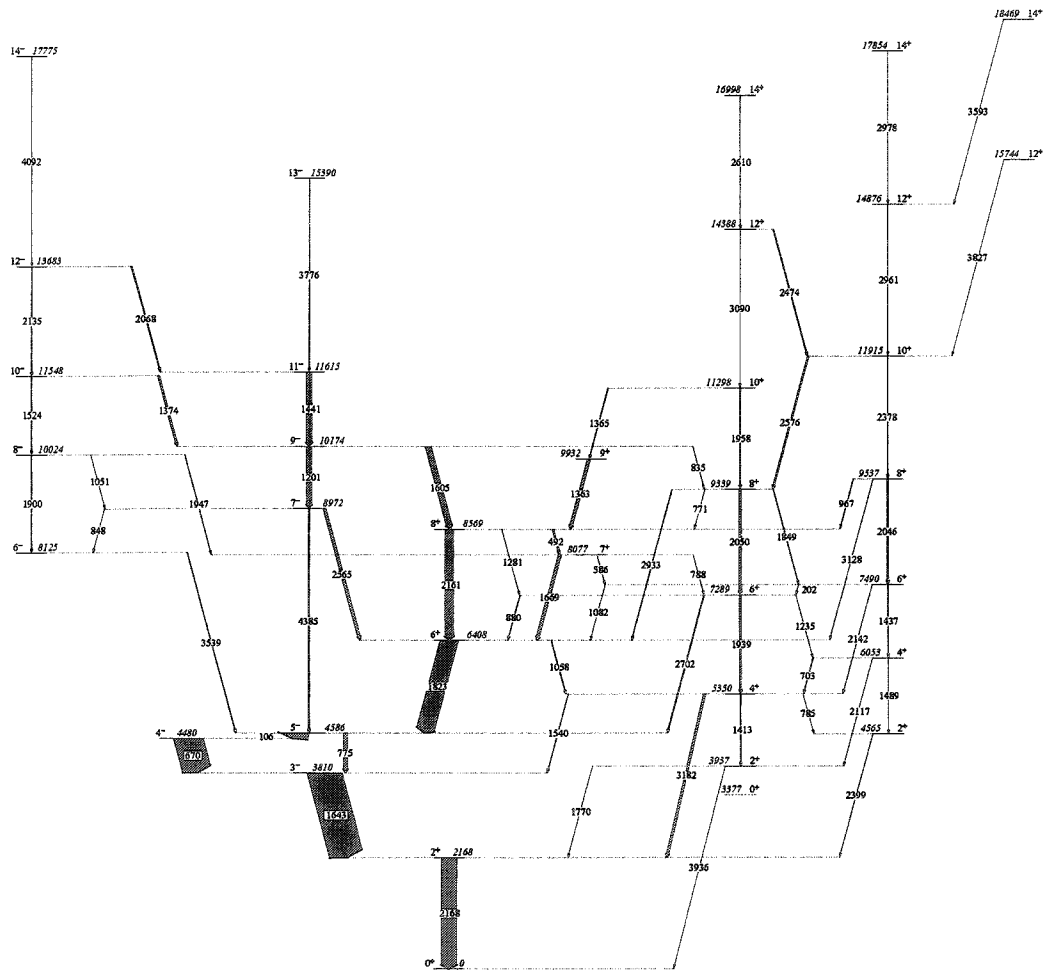
4.1 γ - γ Matrices

An HPGe detector, exposed to many different decays, may be used to eventually collect a γ -ray energy spectrum. The peaks in that spectrum will have areas proportional to the probability of those transitions occurring in the decay chain convolved with an efficiency function for the detector. It is possible, if the structure of the nucleus in question is fairly tidy (for example, if the structure is exclusively based on noninteracting, regularly spaced rotational bands), to build a level scheme using arguments based on the intensities of the peaks and the sums of certain combinations

of peak energies. However, it is very rare indeed for any nucleus to be so obliging as to have structure that is built exclusively on noninteracting, regularly spaced rotational bands; the nucleus described in this thesis is testimony of that. A partial level scheme of ^{38}Ar is given in figure 4.1 as an illustration. In the face of complexity, the information from a single spectrum is insufficient to distill a level scheme. The solution to the problem is to introduce another HPGe detector recording events simultaneously. This enables the experimenter to collect twice the statistics in the same time, and more significantly, can supply extra information in the form of coincidences (pairs of γ rays from the same event).

One might plot the events from one detector on the x-axis of a matrix and the coincident events from the other detector on the y-axis of the matrix and the result would be like fig 4.2. A projection of the entire matrix onto the x axis just brings back the familiar 1-detector spectrum, and if the matrix is symmetric (along its diagonal $x = y$ axis), the projection onto the y-axis will produce the identical 1-detector spectrum. However, one need not project the entire matrix onto the axis in question. Instead, it is illuminating to project only a few channels, those containing a particular peak, onto the axis. This process is referred to as gating. The gate contains only peaks at energies of γ rays that are coincident with the gated peak.

What follows is an outline of the process of level-scheme construction using coincidence spectra. Two gate spectra taken from the ^{38}Ar data are to be seen in figure 4.3. The γ rays referred to in the following discussion are placed in the partial level scheme of ^{38}Ar in figure 4.1. In the upper half of figure 4.3, a gate on the 670 keV γ ray is shown. The most probable coincidences with the 670 keV transition are the 106 keV transition and the 1643 keV transition immediately above and below it in



the level scheme, respectively. The peak with the most area in the 670 keV gate is the 1643 keV peak because GAMMASPHERE's efficiency of detection drops off at energies as low as 106 keV. There is no 775 keV peak in the 670 keV gate because the 670 keV transition and the 775 keV transition are anticoincident (i.e. any decays that include the 670 keV transition necessarily by-pass the 775 keV transition). The lower half of figure 4.3 shows a gate at 2167 keV. It is possible for a single decay sequence in ^{38}Ar to have two transitions of ~ 2167 keV. Decays involving the 2161 keV transition from the level at 8.6 MeV will most probably also include the 2167 keV γ ray at the bottom of the level scheme. The upshot of that is that a gate at 2167 keV will contain coincidences with the 2161 keV transition and vice versa. Another informative feature of the spectrum from the gate on the 2167 keV transition is that the 670 keV peak is much larger than the 775 keV peak. The information to be obtained from that fact is that the 670 keV transition is more probable than the 775 keV transition. They are so close in energy that the response of the detector is unlikely to make an impact in their relative sizes.

Two dimensional coincidence spectroscopy is clearly more than twice as powerful as merely examining 1-dimensional spectra. For example, take the two transitions near 2167 keV in the lower half of figure 4.3, discussed earlier. This is a case in which a third HPGe detector, with the data sorted into a cube, is necessary. Double gates can then be made to unravel which γ -ray belongs where.

GAMMASPHERE had 101 detectors operational for GSFMA93, and thus in theory a 101-dimensional hypercube could have been created and centuple gates could be made. This procedure was not performed for a number of reasons. The first reason is that the advantage of gathering one hundred and one times the statistics of one

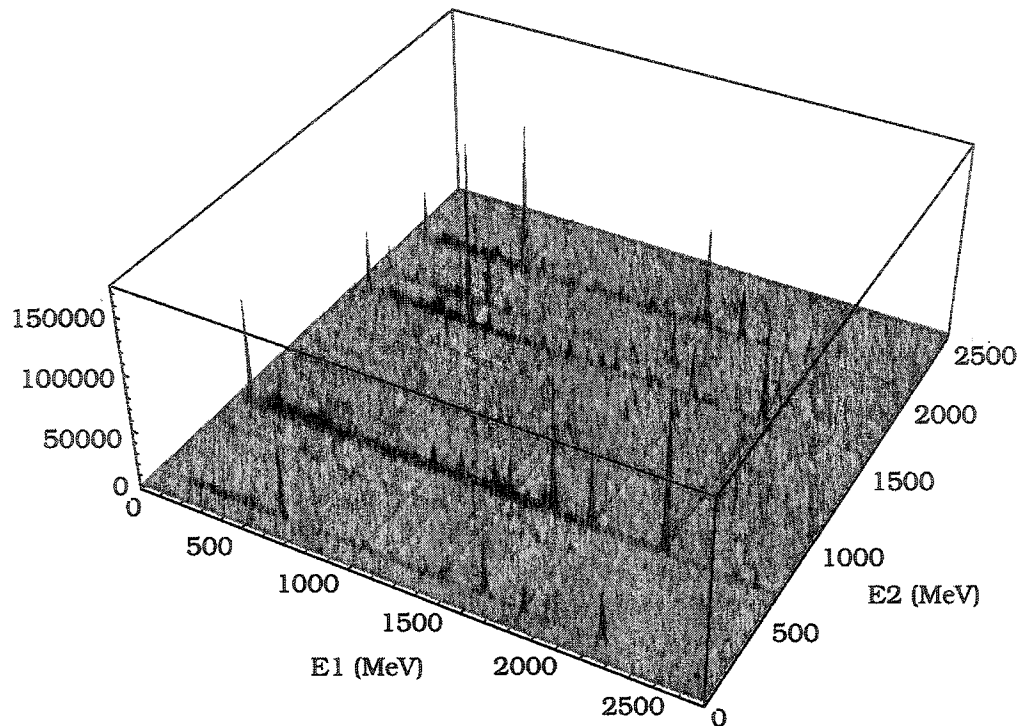


Figure 4.2: A γ - γ Matrix

A γ - γ matrix for ^{38}Ar . Note that the peaks, for example the 670 keV peak, correspond to ridges in the matrix. Peaks are highest where the most probable coincidences lie, such as at 670 keV and 1643 keV.

detector is lost. Even cubes represent such a dramatic loss in statistics that often their creation is futile. The second reason is that a 101-dimensional hypercube would occupy a prohibitive amount of memory on the computer. Typically, each axis of a matrix is 4096 channels (4096 short integers) and thus takes 33554432 bytes. A cube will take more; if treated in the same way as a matrix or a spectrum (i.e. as a $4096 \times 4096 \times 4096$ short integer object), it will occupy approximately 130 Gb. Although there are algorithms for clever ways to fold the dimensions, 101 dimensional objects are still out of reach. The third reason is more trenchant: There is not really

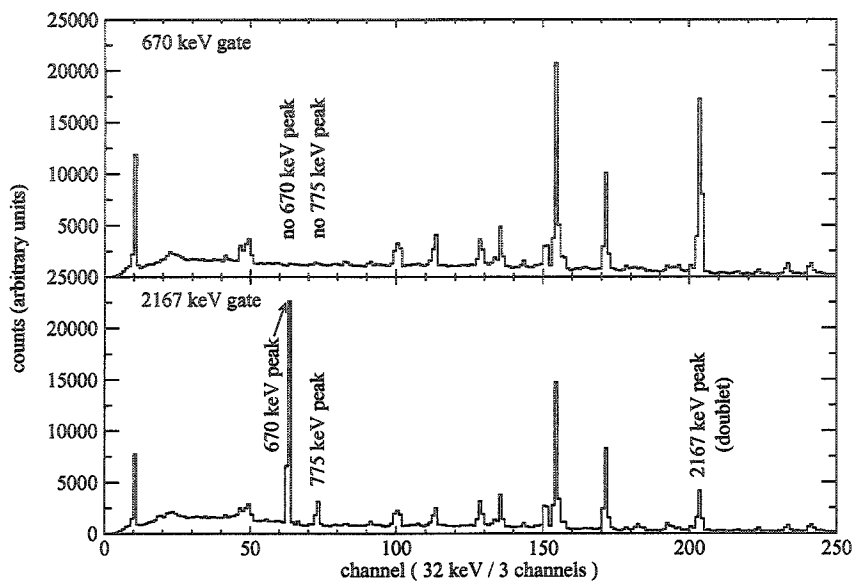


Figure 4.3: Coincidence Gates

The upper histogram is a gate on the matrix in figure 4.2 at 670 keV and the lower is a gate on that matrix at 2167 keV. The 670 keV gate contains neither a 670 keV peak nor a 775 keV peak. The histogram of the 2167 keV gate includes a peak near 2167 since there are two transitions in the level scheme near that energy. These gates had a background spectrum subtracted from them.

any reason to do it. The technique of cubes and matrices is powerful in part because it is easy to imagine what is being done with a double gate. It is unlikely that many people are able to imagine a 101 dimensional hypercube, and even fewer would be able to keep track of the gating conditions of such an object. The fourth reason is most significant of all: There has not yet been a reaction where a real event would produce 101 coincident γ rays, so if one did gate in 100 dimensions, the end result would be an empty spectrum anyway.

Some useful discussion of coincidence techniques is to be found in [Leo87].

4.2 Total Energy Plane

The total energy available to the residual nucleus after a reaction, $E_{\text{total, residual}}$, is an easy quantity to calculate. This is mainly because the reactions are not relativistic, so we can write the conservation of energy rule in a simple, classical manner.

$$E_{\text{total, residual}} = T_{\text{projectile + particles}} - \sum E_{\text{particle separation}} \quad (4.1)$$

The sum of the kinetic energy of the projectile and the evaporated particles, $T_{\text{projectile + particles}}$, is a quantity established by the experimenter. The particle separation energy, $E_{\text{particle separation}}$ is the difference in energy between the mass of the emitting nucleus and the sum of the masses of the emitted particles and the resultant daughter nucleus, and is therefore also an easily accessible quantity before the experiment begins.

The energy of the γ rays, collected in both the HPGe detectors and the BGO detectors, can be added together to give a total γ energy per event, called H. The kinetic energy of the charged particles, collected in the CsI detectors, can also be totalled for each event. Furthermore, the directional and energy information from the particle detector array enables a determination of the kinetic energy of the recoils (which are not directly detected). A map of the energy in the compound system with H on one axis and the summed particle and recoil kinetic energy on the other is called a total energy plane. The sum of H and the total kinetic energy (of both the recoils and the particles) is the total energy available to the residual nucleus. That number is well understood, and can be calculated simply by hand as described in equation 4.1 or using a programme such as QVAL [Lov89]. That total energy represents a line in the total energy plane with slope -1 and intercept (on both axes) equal to the total energy. A “gate” in the total energy plane along that line will therefore

select only events of the reaction with that total energy and will considerably reduce backgrounds. This technique is described in [Sve97].

The advantage of this can be seen in fig 4.4. On the left is shown a spectrum taken in coincidence with all events in which the particles were identified as one alpha and three protons. The inset on that spectrum shows the total energy plane for those events. The large peak in the total energy plane represents events which in fact are not from the $\alpha 3p$ channel. The small shoulder on the left of the major peak are the $\alpha 3p$ events. That is to say, the vast majority of the events for which an α and three protons were identified by the off-line sort routine are not $\alpha 3p$ events at all (see below).

There are a number of factors which contribute to the mis-identification of channels. For example, a low energy α may be labelled a proton, or a high energy proton may be labelled an α , or a particle may be missed altogether. The spectrum on the right in fig 4.4 is the total projection of the $\alpha 3p$ channel once an appropriate gate has been applied on the total energy plane. The gated total energy plane (with only the shoulder) is shown in the inset.

4.2.1 Unexpected Total Energy Plane Data

As indicated above, other reactions were studied in addition to the $\alpha 2p$ channel. The $\alpha 3p$ channel to ^{37}Cl (shown in figure 4.4) was of interest not only because it is a possible contaminant to the ^{38}Ar dataset (whenever one proton is missed), but also because of a remarkable attribute of the total energy plane. A contour plot of the gated total energy plane for the $\alpha 3p$ channel is shown in figure 4.5. Usually, the total energy plane data have a single non-background peak without features. In the $\alpha 3p$

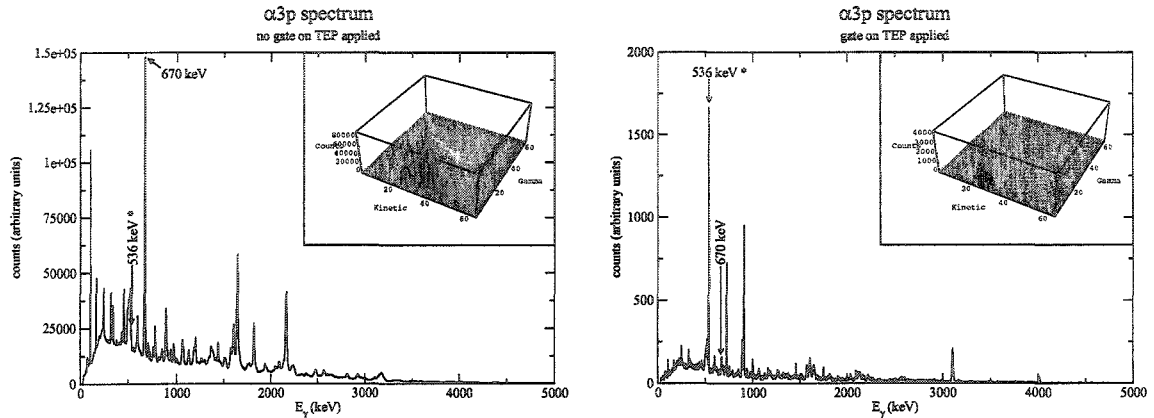


Figure 4.4: Total Energy Plane Gating

The advantage of total energy plane gating is shown. On the left is a spectrum taken in coincidence with all events identified as $\alpha 3p$, with an inset picture of the total energy plane for those events. On the right is the same after total energy plane gating. The two highest peaks in both spectra are marked in both spectra to give a sense of the impact of the total energy plane gating. The peak marked with an asterisk is in the $\alpha 3p$ channel.

data, there are two distinct peaks in the total energy plane. The two peaks are not visible in the total projection on either axis because they are sufficiently close that the added resolution of a two-dimensional plot is needed to distinguish them. It was only through the use of the total energy plane gating method (for entirely different purposes) that this peculiarity came to light.

The canonical understanding of how residual nuclei are fed in heavy-ion fusion-evaporation reactions is that particle evaporation populates states in the continuum which de-excite by γ rays randomly distributed in energy to discrete states which then de-excite by discrete γ rays (as shown schematically in figure 3.2). Recent analysis of feeding mechanisms in a heavy-ion fusion-evaporation reaction has provided insight into another population mechanism, whereby the emission of particles populates discrete states directly. This is a variation on the phenomenon of particle decay from

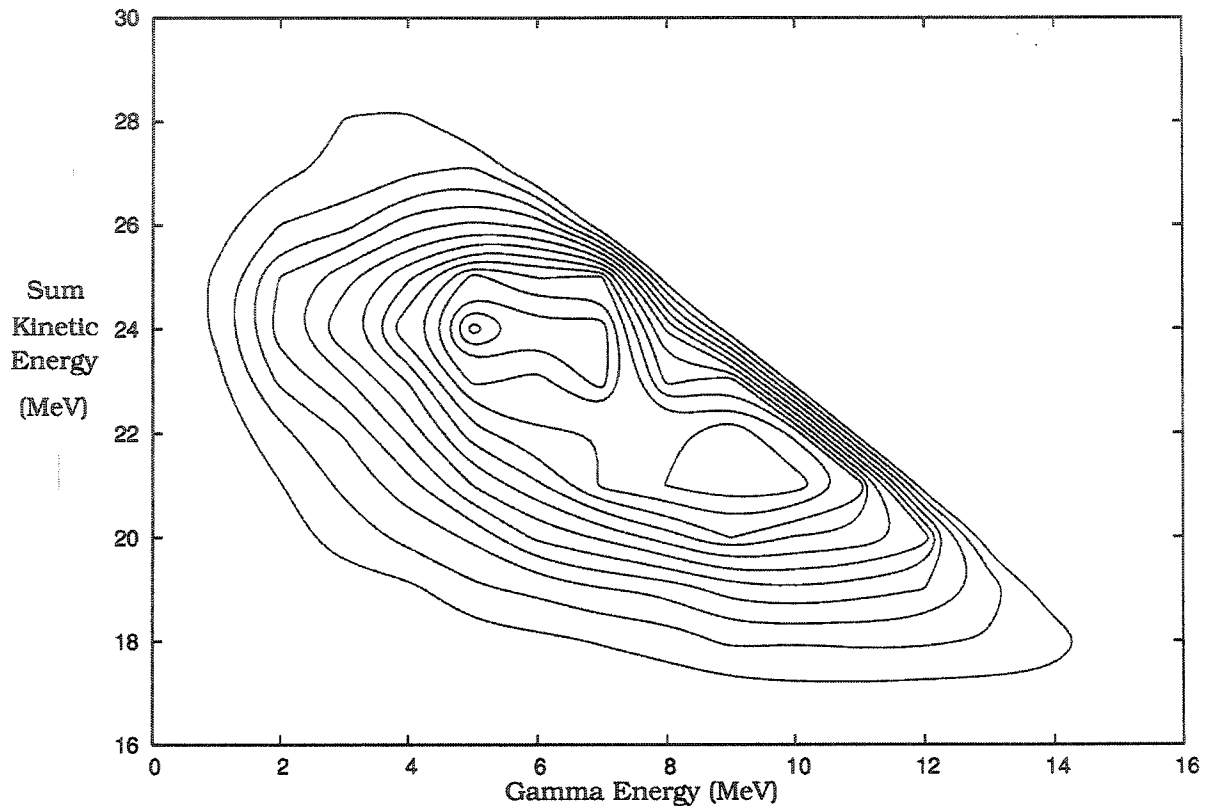


Figure 4.5: Total Energy Plane for ^{37}Cl

The contour map of the total energy plane of ^{37}Cl is shown, with total kinetic energy (in MeV) on the ordinal and total γ -ray energy (also in MeV) on the abscissa. There is one sharp peak at 5 MeV on the H axis and a second, larger peak centred near ~ 9 MeV.

discrete states seen in the mass ~ 60 region [Rud02]. It may be possible to use the events which use this production method to directly experimentally determine the entry spin and energy distributions of some particle unbound states.

The unusual presence of two peaks in the total energy plane indicated that there were two distinct regions of the nuclear level scheme being populated. To better determine what distinguished the two feeding mechanisms, a level scheme of ^{37}Cl was

constructed, and the total energy plane in coincidence with each γ ray in the scheme was examined.

Figure 4.6 shows the level scheme of ^{37}Cl , with the total energy plane profile in coincidence with the stronger γ rays along side. A total energy plane profile is the projection on the summed γ -ray energy of a diagonal single-channel gate along the line of total energy. In other words, it is the total excitation energy available to the channel less the particle kinetic energy. The diagonal gate of the profile provides a well-resolved view of the two regions in the total energy plane.

Both peaks fall on the line of total energy; no γ -ray energy is missing. This is a different effect than that where the total energy plane has two peaks because one is the result of an isomer where some amount of γ -ray energy has been missed. For that reason, in the case of an isomer, both peaks will not fall on the line of constant total energy.

Despite the fact that the $\alpha 3p$ channel was a relatively weak one for this reaction, it is possible to distinguish between the two regions of feeding in the total energy plane for the strongest γ rays. It is therefore fortunate that there is a strong 1458 keV γ ray which de-excites the 8911 keV level. In the profile in coincidence with that γ ray, there is only evidence of one region of population; the higher γ -ray sum energy region at approximately 11 MeV. The very strong 724 keV γ ray which de-excites the 5270 keV level is also in coincidence with a profile with evidence of the majority of its feeding taking place in one region; the lower γ -ray sum energy region at approximately 5 MeV. In coincidence with γ rays below the 724 keV γ ray in the level scheme, both peaks appear in the profile. Those γ rays in coincidence with the 1458 keV γ ray are also in coincidence with profiles showing the higher γ -ray sum

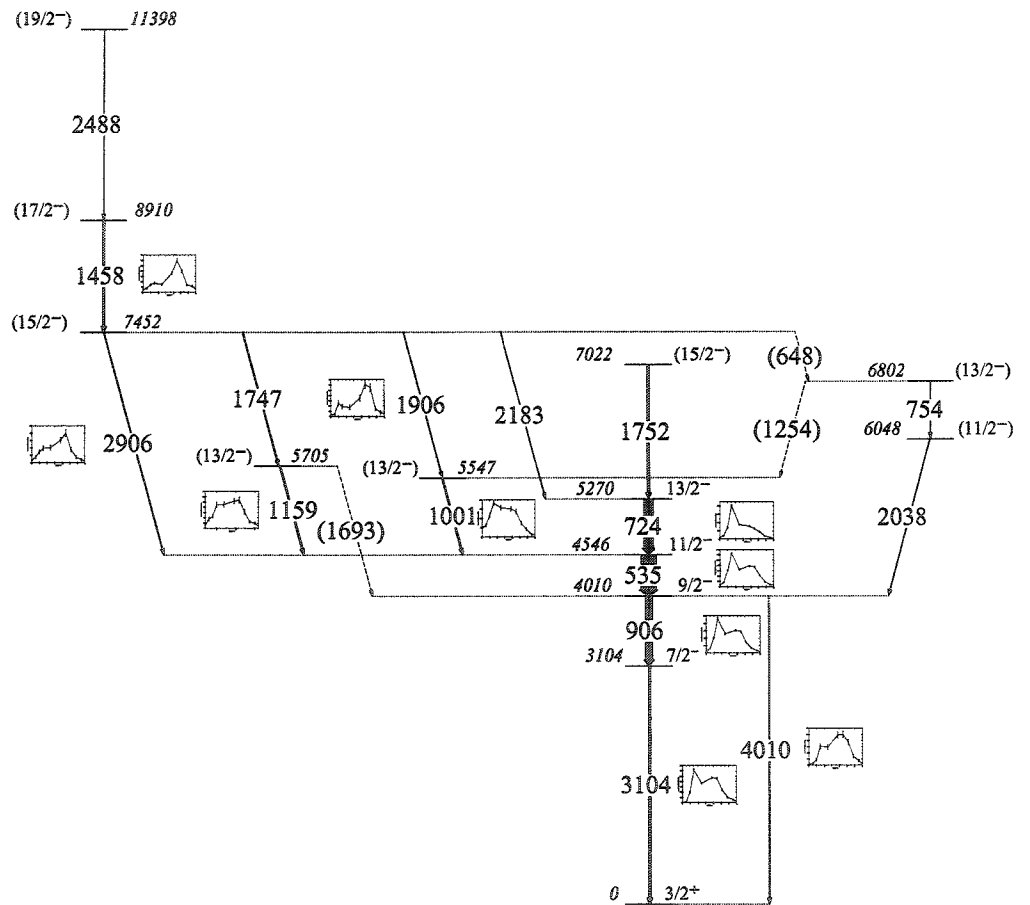


Figure 4.6: ^{37}Cl Level Scheme and Total Energy Plane Profiles
 The level scheme of ^{37}Cl . Profiles in coincidence with strong singly-gated γ rays with no background subtraction are shown.

energy region of feeding.

By adding the total energy plane information to the observation that there is an increase in intensity below the 5270 keV level, we deduce that the lower region of feeding is to that state and not through any other discrete γ rays. Given that there is insufficient energy for statistical γ rays, and that it is improbable that continuum states would exist with any strength with discrete states nearby, we deduce that the feeding of the 5270 keV state is not through any statistical γ rays, either. The particle evaporation populates the discrete 5270 keV state directly, without any intervening γ decays.

Now that it has been established that the 5270 keV level has been fed directly by particle evaporation, the question of why that state would be so favoured must be asked. There are two other states with the same spin and parity assignment within 500 keV. Why would the 5270 keV level gain so much intensity through the direct particle evaporation feeding and the other two so little? To answer that question, in the discussion that follows, I will describe how particles tunnelling out of parent states in ^{38}Ar close in energy to the 5270 keV state in the daughter ^{37}Cl can explain all of the unusual observations. Furthermore, I will describe the advantage of studying this kind of discrete population, which is that it makes a previously unavailable determination of the spin and energy of the state in the parent ^{38}Ar possible.

The first, and most obvious answer is that the spin and parity assignments for those states are incorrect. Indeed, the previous assignment of the 5705 keV state is $\frac{9}{2}^-$, and for the 5547 keV state it is tentatively $\frac{7}{2}^- - \frac{13}{2}^-$ [FSB+96]. However, given the strengths of the decays from those states to the 4546 keV $\frac{11}{2}^-$ state, it does not seem likely that the spins of those states are less than $\frac{13}{2}$. Both states also are fed

by γ rays from the $\frac{15}{2}^-$ state, which reinforces the spin and parity assignment given here. The 1748 keV (from the 7453 keV state to the 5705 keV state) doublet with the 1750 keV γ ray (from the 7021 keV state to the 5270 keV state) had not been observed when the previous spin and parity assignments were made, but now that it has been placed in the level scheme, it is highly unlikely that it is an M3 but with strength comparable to the E2 2907 keV transition. The same can be said of the 1906 keV γ ray. The assignment of $\frac{9}{2}^-$ spin and parity to the 5705 keV state [Noo84] was based on lifetime and branching ratio arguments, which selected $\frac{9}{2}^-$ from a choice of $\frac{5}{2}^- - -\frac{11}{2}^-$. The additional information now available makes a re-assignment of that spin and parity reasonable.

Once we accept that there really are other $\frac{13}{2}^-$ states near in energy to the 5270 keV state, some reason for the strong feeding to the 5270 keV state and not the others must be found. A good reason would be that the particle whose evaporation populates the 5270 keV state is close to it in energy. If it were, in fact, tunneling through the Coulomb barrier, then small differences in energy would make very large differences in the probability of the proton evaporation taking place. The ideal test of that theory is in the particle energies in coincidence with the 1159, 1001, and 724 keV γ rays. A comparison of those energies distinguishing between particles feeding the continuum states and particles feeding discrete states (particularly the 5270 keV state) would enable a measurement of the relative intensities of the feeding. However, the variation of the particle energies was too great to make any distinction.

As an alternative, the tunneling probability can be calculated as a function of energy. The bounds of the particle energy peak were reduced in this analysis by finding the most probable order of emission of the particles as follows: The energy

of all particles was first reconstructed to the centre of mass frame. The energies of all particles and their particle separation energies were then compared to find the one which removed the most excitation energy from the compound system. That particle was designated the first evaporated. The three remaining particles were then reconstructed to the stationary frame of the recoil created when the first particle was evaporated. In that frame the three remaining particles energies and separation energies were compared and the one which removed the most excitation energy was designated the second particle out. This procedure was repeated until all of the α and three protons had been given an order of evaporation. By this reasoning, the most probable order of evaporation was 61% by $p\alpha pp$, 34% by αppp , and 5% by $ppp\alpha$. The very high proton separation energy of ^{42}Ca results in there never being the order of evaporation $pp\alpha p$. Since 95% of the time the final particle evaporated is a proton (regardless of the order of evaporation), that is the particle discussed here. The energy of the final proton evaporated is approximately 3 MeV. Figure 4.7 shows the energies of the deduced last particle evaporated.

The lifetime for a proton tunnelling from ^{38}Ar (the $\alpha 2p$ channel of this reaction) is calculated by modifying the simple Gamov α decay theory [Gam28], including the angular momentum removed by the proton, as shown in appendix A. The lifetime, τ , is calculated for a range of low energies

$$\tau(E) = r_1 \sqrt{\frac{2m}{E}} \exp \left[2 \int_{r_1}^{r_2} \sqrt{2m \left(\frac{e^2}{4\pi\epsilon_0} \frac{Z_1 Z_2}{x} + \frac{\hbar^2}{2m} \frac{\ell(\ell+1)}{x^2} - E \right)} dx \right] \quad (4.2)$$

using $r_1 = 1.2A^{\frac{1}{3}}$, and r_2 the radius at which the sum in the brackets goes to zero (when $E = V$). The results are shown in figure 4.8. Although this is a very simple calculation and its absolute values should by no means be taken as predictive, it

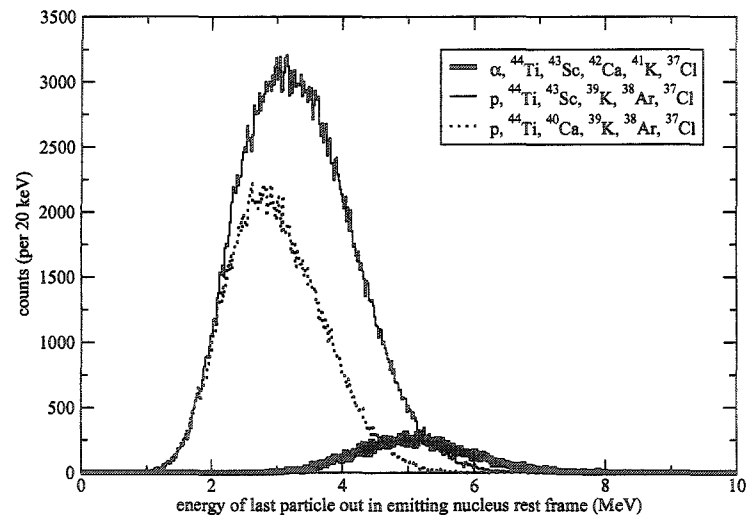


Figure 4.7: Evaporated Particle Energies

Three different evaporation chains were deduced. For each of these chains, the energy of the final particle evaporated (in the frame of the emitting recoil) is shown.

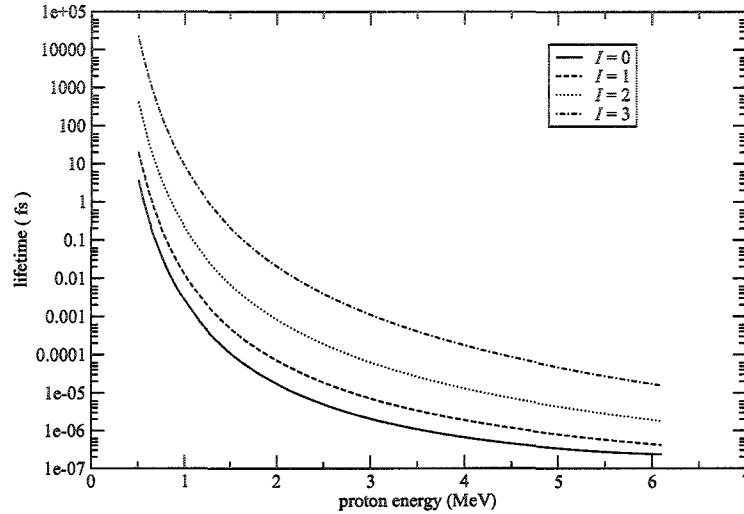


Figure 4.8: Simple Calculation of Lifetimes of Proton Evaporation from ^{38}Ar . The lifetime for proton tunneling from particle-unbound parent states in ^{38}Ar as a function of the energy of the proton evaporated, for protons which remove 0, 1, 2, or 3 units of angular momentum. Compare the lifetimes for 3 MeV protons removing $I = 0\hbar$ or $1\hbar$.

is useful when comparing relative lifetimes. Using the base proton energy 3 MeV, a difference of 500 keV will more than double the lifetime. It is therefore no surprise that the 5270 keV level should be populated more than its neighbours. Unfortunately, the width of the particle energy peaks is such that it is really impossible to draw further conclusions.

This simple calculation of the lifetimes has one other benefit: It shows the very large differences in tunneling probabilities for particles which remove angular momentum compared to those that do not. At the energy of interest, 3 MeV, the difference in lifetime between a proton which removes one unit of angular momentum

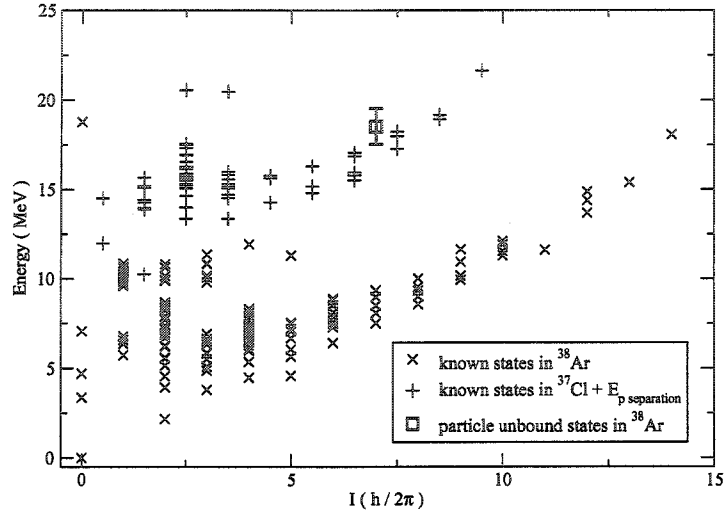


Figure 4.9: Known Levels in ^{38}Ar and ^{37}Cl

The known states in ^{38}Ar and ^{37}Cl shown. The ^{38}Ar proton separation energy is added to the ^{37}Cl states to make both appear with the same absolute scale. The position of the proposed particle-unbound parent states in ^{38}Ar is also shown.

and one that removes none is almost an order of magnitude. Thus with reasonable certainty it is possible to state that the spin of the particle-unbound parent states in ^{38}Ar was $\frac{1}{2}\hbar$ different than the 5270 keV state in ^{37}Cl . Furthermore, if the particle-unbound parent states in ^{38}Ar had had a spin $\frac{1}{2}\hbar$ less than $\frac{13}{2}$, the decay would have had the opportunity to go to the 4546 keV level by a proton with 724 keV more energy and that would have been favoured. The most plausible spin of those particle-unbound parent states in ^{38}Ar is $\frac{1}{2}\hbar$ more than that of the 5270 keV state in ^{37}Cl .

Thus, the spin of the parent states in ^{38}Ar is $7\hbar$, and they have negative parity. The energy of those states is known to the current particle energy resolution. This

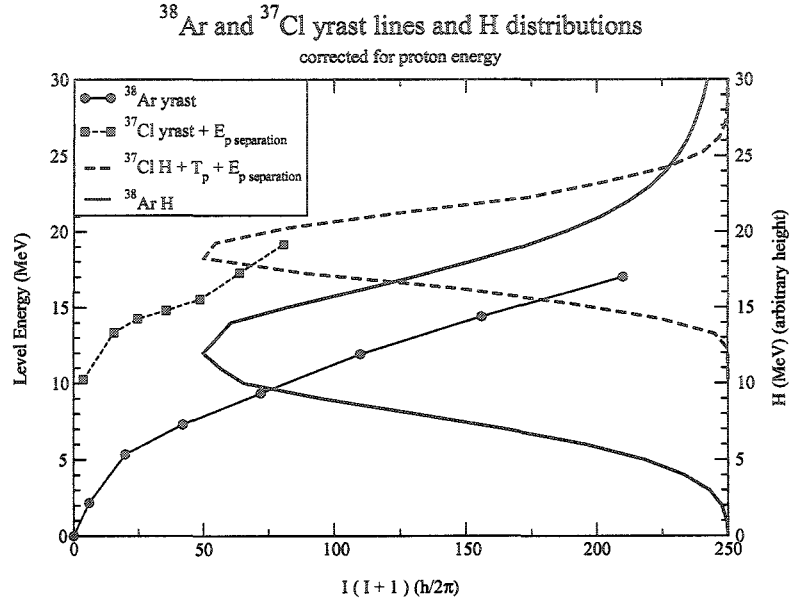


Figure 4.10: Total γ -Ray Energy and Yrast States for ³⁸Ar and ³⁷Cl. The data is from GSFMA93. In that instance, the entry energy distribution of ³⁸Ar is completely overlapping with the ³⁷Cl energy distribution, even for the particle-bound states.

gives us a direct experimental determination of the spin and energy of a region of parent states in ³⁸Ar. (It is a direct experimental determination of the entry energy and entry spin of those states.) Figure 4.9 shows the known discrete levels in ³⁸Ar and the known discrete levels in ³⁷Cl on the same scale; i.e., with the proton separation energy added to the ³⁷Cl levels. Also on the figure is the deduced location of the parent states in ³⁸Ar from this work. Figure 4.10 shows the H (total γ -ray energy) distributions on the same scale as the yrast levels for both ³⁸Ar and ³⁷Cl.

Although the population of discrete particle-bound states from continuum particle-unbound parent states is not what is usually observed, it is also not new physics. It is well understood that there is competition between all kinds of decay

whenever a nucleus occupies an unstable state, and the most probable decays are the ones that get studied because they produce the most statistics for experimentalists. What is observed in this case is that whenever ^{38}Ar was populated with a certain spin and a certain range of energies, a proton evaporated to form ^{37}Cl at a discrete excitation. We can comfortably imagine that if ^{38}Ar were populated at an MeV or two greater energy, an α particle might have been evaporated instead. ^{38}Ar was populated at a particular spin and a particular energy; at some sets of spins and energies γ decay would dominate as the means of de-excitation, at other spins and energies, neutron decay might dominate. As it happens, the existence of the 5270 keV state in ^{37}Cl caused proton decay to dominate when ^{38}Ar was populated at spin $7\hbar$ and excitation energy ~ 18.5 MeV.

There is no reason to assume that this technique of determining the entry spins and energies is unique to this nucleus. In fact, I observed the same effect in the $2\alpha 2p$ channel of the same experiment, ^{34}S . There is an advantage in the low mass nuclei of sparse level schemes at low energies, which makes this system is a good starting point. However, once the cause of the different feeding mechanisms is well understood, there is every reason to believe that experimental determinations of entry spins and energies of particle-unbound parent states could be made in other mass regions.

4.3 Off-Line Compton Suppression

As mentioned in section 3.3, the HPGe array is surrounded by BGO crystals to catch Compton scattered γ rays. Although it is possible to put a block of BGO in the front of the HPGe, it is undesirable to have much material between the reaction site and the detectors, and so it is possible to have γ rays scattering at 180° . This

source of background can be removed by disallowing coincidences between detectors that oppose each other in the array. However, it is also possible for high-energy γ rays to deposit some energy in a HPGe detector and then scatter without interaction through two full BGO suppressors before finally depositing the remainder of their energy in a second HPGe crystal. The amount of energy deposited in the first crystal is minimized when the scattering angle is near 90° , which is the scattering angle between near-neighbour detectors. This kind of background is not frequently observed, since it arises from very intense, usually high-energy decays. The level scheme of ^{38}Ar features a relatively high energy γ ray as the $2^+ \rightarrow 0^+$ (i.e. strongest) transition. The combination of high energy and high intensity produced an unexpected source of noise in the data. Since the level scheme for ^{38}Ar has several high-energy decays near the ground state (i.e. quite intense), and the channel was a very strong one for the reaction, the background from near-neighbour scattering was a concern.

Figure 4.11 shows a gate at 1414 keV. In that gate are clearly visible peaks at 106 and 670 keV. Both of those γ rays are in anticoincidence with the 1414 keV γ ray and should therefore not be observed in the gate. The clue to the source of these peaks is in the wide peak at ~ 229 keV. Immediately below the 106 and 670 keV peaks in the ^{38}Ar level scheme is a 1643 keV γ ray. If that γ scatters at $\sim 160^\circ$, then it will deposit 229 keV in the first detector and the final 1414 keV in the second detector, 160° away. Hence in the 1414 keV gate will be peaks from γ rays coincident with the 1643 keV γ ray. Since in this instance, the 1414 keV γ ray in partnership with the 229 keV γ ray is “standing in” for the 1643 keV gamma ray, no peak at 1643 keV should appear in the spectrum. Confirming that, figure 4.11 contains no peak at 1643 keV. The rogue peaks are so intense because the 1643 keV γ ray is much

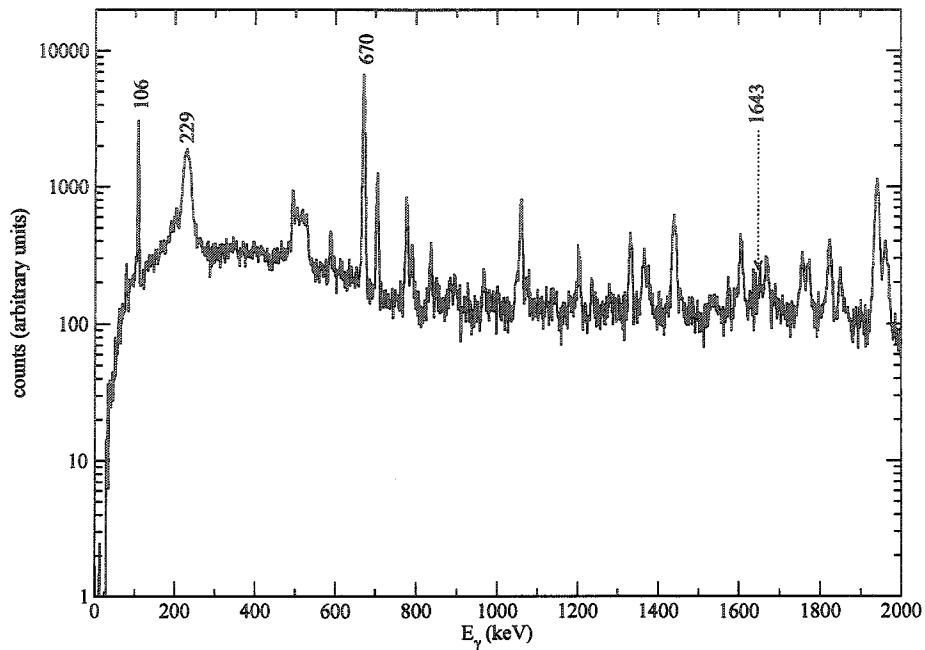


Figure 4.11: Near-Neighbour Scattering

This gate on the 1414 keV transition illustrates scattering between near-neighbour HPGe pairs. The coincidences with the 670 and 106 keV transitions (with which the 1414 keV transition is actually anticoincident) arise, along with the wide peak at 229 keV, from near-neighbour scattering of the intense 1643 keV γ ray. This is explained in detail in section 4.3.

more intense than the 1414 keV γ ray. It may seem unlucky in this case that a γ ray genuinely in the decay scheme should have the same energy as a scattered peak from a very intense γ ray scattering by one of the discrete angles between detectors inside the array, but there are so many very intense decays combined with so many more decays elsewhere in the scheme that it is statistically probable.

This pattern of background quite convincingly mimics a real phenomenon of nuclear excitation, where bands of E2 transitions are joined to other bands of different E2 transitions through pairs of M1 transitions, with energies that sum to the original

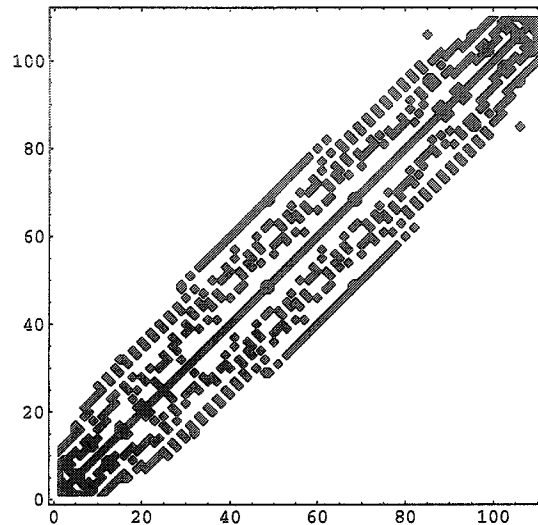


Figure 4.12: GAMMASPHERE Near-Neighbour Map

The map of near neighbours of the GAMMASPHERE array. The x- and y-axis scales are both detector number. Self-coincident pairs are also indicated.

E2 transition energy.

The solution to the problem of near-neighbour scattering was analogous to the solution to the 180° scattering: to disallow near-neighbour collisions. Figure 4.12 shows the coincidences between detectors that were removed. In the interests of preserving statistics, only the near-neighbour coincident pairs were removed from the data set, which means that one may see artifacts of Compton scattering at other angles in the data.

Of course, if it is possible for γ rays to scatter undetected through two adjacent Compton suppressors at, it is possible for them to scatter undetected through more. Greater scattering angles will force the γ ray to travel through more BGO, and the probability of detection increases with increasing path length, so adjacent-detector scattering represents the highest contribution to this source of background. There

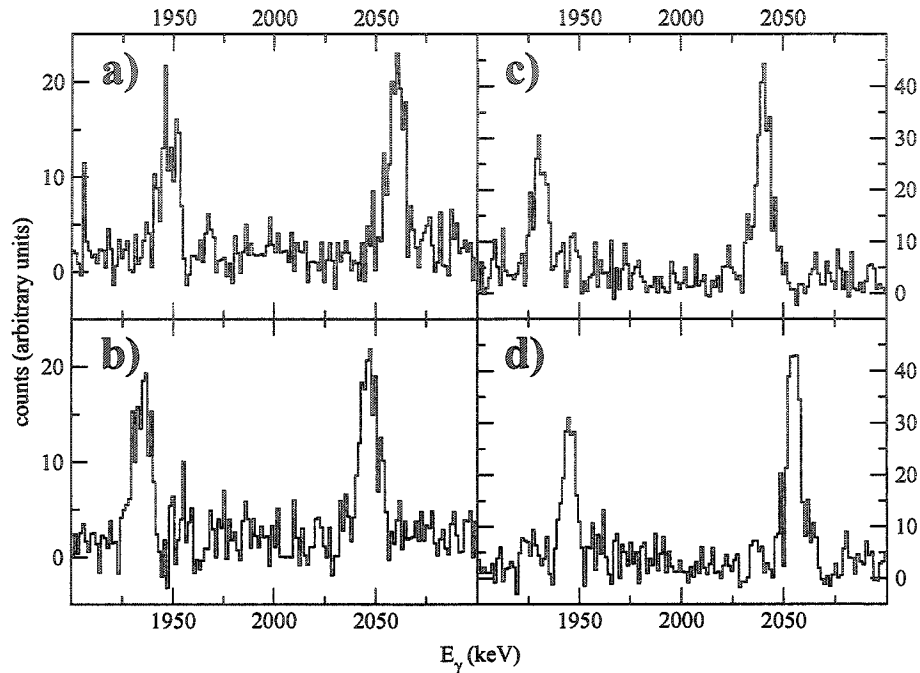


Figure 4.13: Doppler Shifted Fast Transitions

The 1939 keV and 2050 keV transitions at different angles in the detector and with varying Doppler corrections. Figures a) and b) have $\beta_{\text{corr}} = 80\% \beta_{\text{max}}$ and figures c) and d) have been Doppler corrected with $\beta_{\text{corr}} = \beta_{\text{max}}$. Figures a) and c) are data observed in the front ring, at 32° , and figures b) and d) are data observed in the back ring, at 163° . Note that the difference in measured energy between the front and back rings is more pronounced at low β_{corr} for the faster 2050 keV transition than it is for the 1939 keV transition lower in the band. These data are from gates on the 2981 keV transition.

are 3 near neighbours to each detector, which means that there are 330 possible scattering pairs of adjacent detectors (given that one may scatter into its neighbour, or its neighbour may scatter into it). That does not represent many of the 5995 total possible pairs of detectors.

4.4 Thin-Target Doppler Shift Attenuation Method

The lifetimes of states can be measured by the Doppler Shift Attenuation Method (DSAM) [Sie77]. The standard technique of DSAM is to use a target backed by gold or tantalum foil, in enough quantity to be guaranteed to stop all the recoils inside it (while still allowing the γ rays to escape). The decaying recoil nuclei then emit γ rays as they travel at varying velocities, slowed by the thick target. The γ rays are emitted from a moving nucleus and therefore have a shift in energy from the Doppler effect. The distribution of velocities of the moving nuclei emitting the γ rays leads to a so-called Doppler shift distribution. The shape and degree of Doppler broadening is related to the velocity and velocity distribution of the decaying nucleus, which in turn is related to the time that the state takes to decay, i.e. the lifetime.

Thin-target DSAM is very like the standard DSAM, but it is used to measure lifetimes that are very short, such as those of quickly rotating states in superdeformed bands. As the name suggests, there is no extra backing on the target, and this constrains the technique to measuring only states which decay (on average) in less time than it takes for the recoil to exit the target.

The measured Doppler-shifted γ -ray energy E'_γ is related to the angle between the path of the recoil and the path of the γ ray, θ , and the velocity (divided by c) of the recoil, β , by

$$E'_\gamma = E_\gamma \frac{\sqrt{1 - \beta^2}}{1 - \beta \cos \theta}. \quad (4.3)$$

During analysis, that measured E'_γ is corrected by β_{corr} to be

$$E_\gamma^{\text{corr}} = E'_\gamma \frac{1 - \beta_{\text{corr}} \cos \theta}{\sqrt{1 - \beta_{\text{corr}}^2}}, \quad (4.4)$$

which is related to the original, true γ -ray energy, E_γ , by

$$E_\gamma^{\text{corr}} = E_\gamma \frac{1 - \beta_{\text{corr}} \cos \theta}{1 - \beta \cos \theta} \sqrt{\frac{1 - \beta^2}{1 - \beta_{\text{corr}}^2}}. \quad (4.5)$$

Using the binomial theorem, and ignoring all terms which have the small β and β_{corr} terms of order greater than one*, equation (4.5), can be reduced to

$$E_\gamma^{\text{corr}} \approx E_\gamma (1 - (\beta_{\text{corr}} - \beta) \cdot \cos \theta) \quad (4.6)$$

Thus, plotting E_γ^{corr} against $\cos \theta$ will produce a line with slope $\beta_{\text{corr}} - \beta$. The point at which the slope is equal to zero is where the corrected β_{corr} is equal to the true β . This is illustrated in figure 4.14. Each point is a fit of the area of a peak in a spectrum that is corrected by the % Doppler shift indicated.

Figure 4.13 illustrates how the spectra are different at each shift. The shape, and position of peak in the spectrum varies with each new Doppler correction applied. The response of the peak to the Doppler correction is unique to the average velocity of the recoil when that transition took place. For this reason, it is necessary to fit each peak at each Doppler shift individually (for each gate, of course).

The corrected γ -ray energies are least-squares fit to straight lines, which are shown in figure 4.14. The slopes of those lines are then plotted against the percent of the full shift used to correct the energies, and where that line crosses zero is the true velocity, expressed as a percentage of the velocity in the full Doppler shift. This quantity is the $F(\tau)$ value. In summary, then, β is the scaled average velocity of the recoils when they decay from a particular state, to be distinguished from β_{corr} which is a value input to the Doppler correction by the experimenter. β_{corr} is usually chosen

*In this reaction, β_{corr} is 4.21% c , so terms with β or β_{corr} of order greater than one contribute at most 0.2% c (or 5% of the total Doppler correction) to the equation.

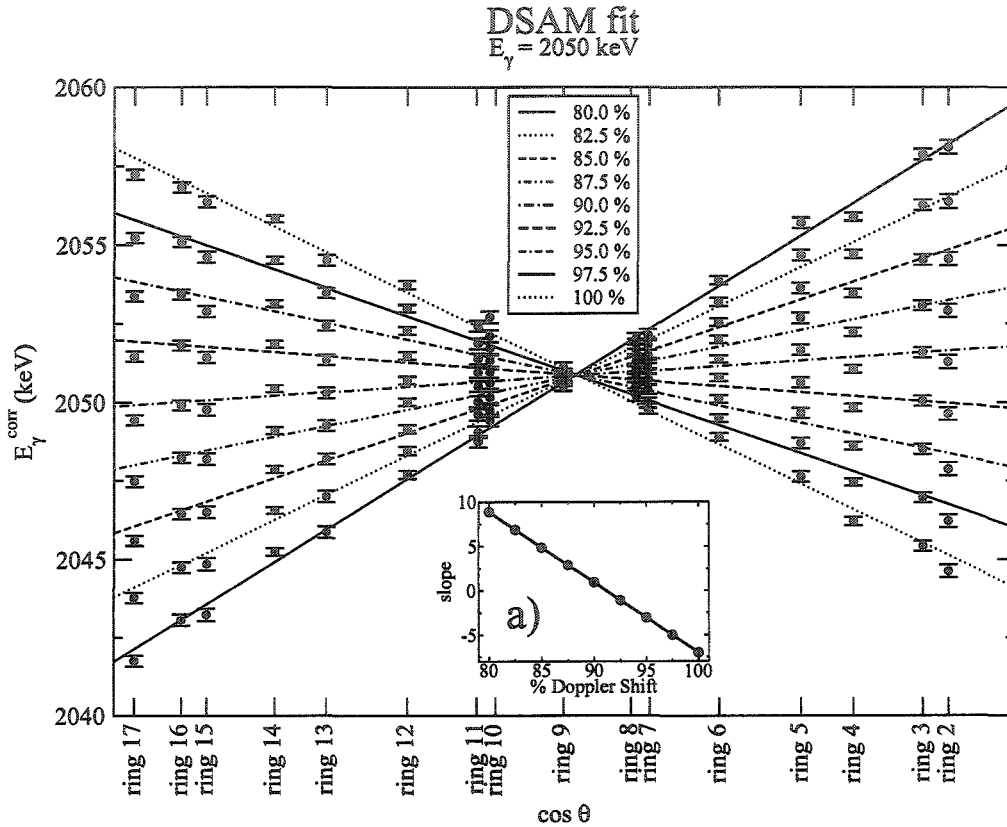


Figure 4.14: Sample DSAM fit

In this figure are the fits to a peak at $E_\gamma = 2050 \text{ keV}$ at Doppler shifts varying from 80% to 100% of the full shift. The inset, a), shows the least squares fit to a straight line of those slopes, which yields the result, for this particular gate and this particular γ ray, that the true velocity shift is $(91.17 \pm 0.58)\%$ of the velocity applied in the full Doppler shift correction. The error bars on the inset figure are smaller than the data points.

to be a percentage of the full scaled velocity, β_{full} , which is the scaled velocity of the compound system at the time of its creation as calculated through the experimental kinematics. The $F(\tau)$ value is then

$$F(\tau) = \frac{\beta}{\beta_{full}} \quad (4.7)$$

4.4.1 Side Feeding

The determination of the lifetime of a state relies on an understanding of the transitions preceding the one being studied, as described in section 2.3. However, states are fed by a number of different transitions, some of which may be randomly distributed in energy and therefore unmeasured. The measurement of $F(\tau)$ is best made from a gate above the transition of interest.

4.4.2 Target Thickness

Because the lifetimes of states are determined from the velocity of the recoil, and the velocity depends on the distance the recoil has travelled through the target, the calculation of the lifetime is dependent on the target thickness. Although the target thickness is estimated by the target maker, it is not known with any accuracy. For that reason, the target thickness is determined by matching the exit velocity (see section 4.5.2) as measured to the exit velocity resulting from a simulation in which the target thickness can be varied.

4.4.3 Stopping Powers

The stopping powers used were taken from the Northcliffe and Schilling (NS) tables [Nor70]. Those values are for electronic stopping only, but at the velocities involved in heavy-ion fusion-evaporation reactions the nuclear stopping is negligible [Bla66]. However, the NS values do not include atomic shell effects and in order to improve those values, the method of Sie *et al* was followed [Sie77]. Tables compiled by Ziegler and Chu (ZC) of the stopping of ${}^4\text{He}$ [Zie74] which include the atomic shell

effects are used to scale the NS values for the stopping of heavy ions (HI):

$$\left(\frac{dE}{dx}\right)_{\text{HI}}^{\text{better}} = \left(\frac{dE}{dx}\right)_{\text{HI}}^{\text{NS}} \left[\left(\frac{dE}{dx}\right)_{\alpha}^{\text{ZC}} / \left(\frac{dE}{dx}\right)_{\alpha}^{\text{NS}} \right], \quad (4.8)$$

where the $\left(\frac{dE}{dx}\right)_{\alpha}^{\text{ZC}}$ and the $\left(\frac{dE}{dx}\right)_{\alpha}^{\text{NS}}$ possess a common energy per mass unit with the $\left(\frac{dE}{dx}\right)_{\text{HI}}^{\text{NS}}$.

Although the ZC tables have data only up to 0.5 MeV/amu, they include a semi-empirical extrapolation of the data up to 1.0 MeV/amu, which is high enough in energy to be of use for the stopping of the recoils in the target. It is the stopping of the recoils in the target to which the final result is most sensitive. The stopping powers for the beam in the target (which have comparatively little impact on the final outcome) are not scaled by the ZC values because the relatively high energy per mass unit of the beam is too far to extrapolate the ZC tables.

The ZC-scaled stopping for ^{38}Ar can be seen in figure 4.15. The NS values $\pm 10\%$ are included in the figure also, to give a sense of the scale of the ZC corrections. The highest impact of the ZC corrections is at higher proton number in the rare-earth region [Sie77], where the correction can be as great as 25%.

4.5 Determination of the Lifetimes

The general technique to determine lifetimes is to model the system and compare the data outcome of the model to the measured data. The model most importantly includes the slowing-down of the recoil as it passes through the target and the lifetime of the state. Other parameters of the model used here are the slowing-down of the beam in the target (including random positioning of the reaction in the target), the momentum kick given by the evaporated particles to the recoil, and an optional

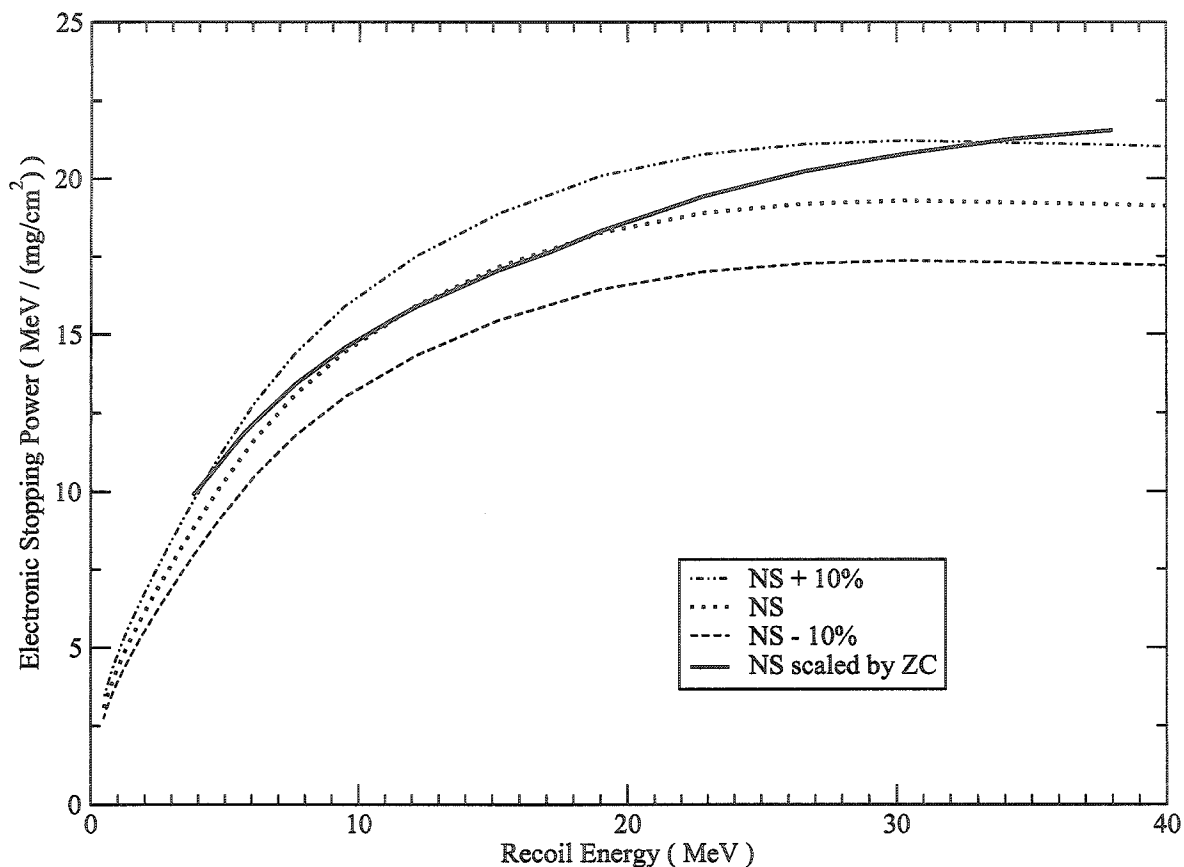


Figure 4.15: Stopping Powers of ^{38}Ar

The stopping of ^{38}Ar in Mg is shown for the NS table values and those values scaled by ZC according to equation 4.8. The values of NS $\pm 10\%$ are also included for comparison.

number of “unseen” transitions feeding the measured ones. The lifetime is established when the modelled data match the measured data for the velocities of the recoils when the state decays.

In order to extract a lifetime for a level from the data, it is necessary to make some assumptions about the decays that preceded the one of interest. The favoured technique is to make a simulation of a decay chain with a given quadrupole

deformation. This assumes that the quadrupole moment is constant throughout the band. For superdeformed bands in higher mass regions, this can be a reasonable assumption; for states high in energy above the decay out of the superdeformed band, there is very little interaction between states in the superdeformed band and states in the rest of the level scheme. Even if there is some change in the quadrupole moment within the band, it is usually acceptable to assume that the change is smooth and linear with angular momentum. In either case, the quadrupole moments are used to calculate lifetimes of the states, and the decay chain is simulated using those lifetimes. The velocity of the recoil at the point it de-excites from those levels is simulated. (It is at this point that the measured bias in the data is introduced, see section 4.5.1). This process is repeated many times, and in the end a mean $F(\tau)$ value is obtained for each level in the band. Those mean $F(\tau)$ values are compared to the ones measured and a χ^2 minimization is performed to determine the quadrupole moment(s) for that band. The lifetime is calculated from the transition quadrupole moment according to equation 2.23.

For the highly deformed bands of ^{38}Ar , the story is somewhat different. It is difficult to classify them as “bands” in the traditional sense. There is a great degree of interaction with the rest of the level scheme, and this has an effect on the quadrupole moments which makes it unlikely that they are either constant or smoothly varying. In this case, it is possible to assign a unique quadrupole moment to each individual level. However, such an assignment affords no means of ascertaining the uncertainty in the fit itself. In that case, the error bars reflect the uncertainty in the measured $F(\tau)$ value and the beam energy and the target thickness and the stopping powers. For that reason, such a determination of the quadrupole moment is not ideal.

Both methods were used to calculate the lifetimes, and the outcome of the method using the most appropriate assumptions for each cascade individually was used to decide the final results.

4.5.1 MICROBALL Bias

The events detected have a bias towards slower-going recoils. This is because the particle detectors are more efficient at catching higher-energy particles. Forward-going particles are more likely to have higher energy in the lab frame because they get a boost from the centre-of-momentum motion. Those forward-going particles give the recoils a backwards “kick” when they are emitted. The end result is a bias in the data towards slower recoils. This can be seen in figure 4.16, which shows a contour plot of the combined x-velocity and the z-velocity of the recoils. The x-velocities are symmetric about a point very near zero (as are the unshown y-velocities), but the z-velocity peaks at $\sim 0.0325 c$ which is considerably below the centre-of-mass velocity of the compound system ($\sim 0.042 c$). If the particles were detected perfectly isotropically, there would be no average contribution to the recoil velocity from the particle “kicks”, and the mean z-velocity of the recoils would be the same as that of the centre-of-mass system. As it stands, the fully-reconstructed recoil velocities are on average $\sim 6.9\%$ slower than the centre-of-mass system.

The bias is included in the simulations through the addition of the actual recoil velocities (as calculated from the particle energies and angles). The calculation of lifetime is made for each event, and a random kick taken from the real data is included in the simulations of the recoil’s progress, and then an average over all events is obtained. In this way, the model has the same bias as the data and the two

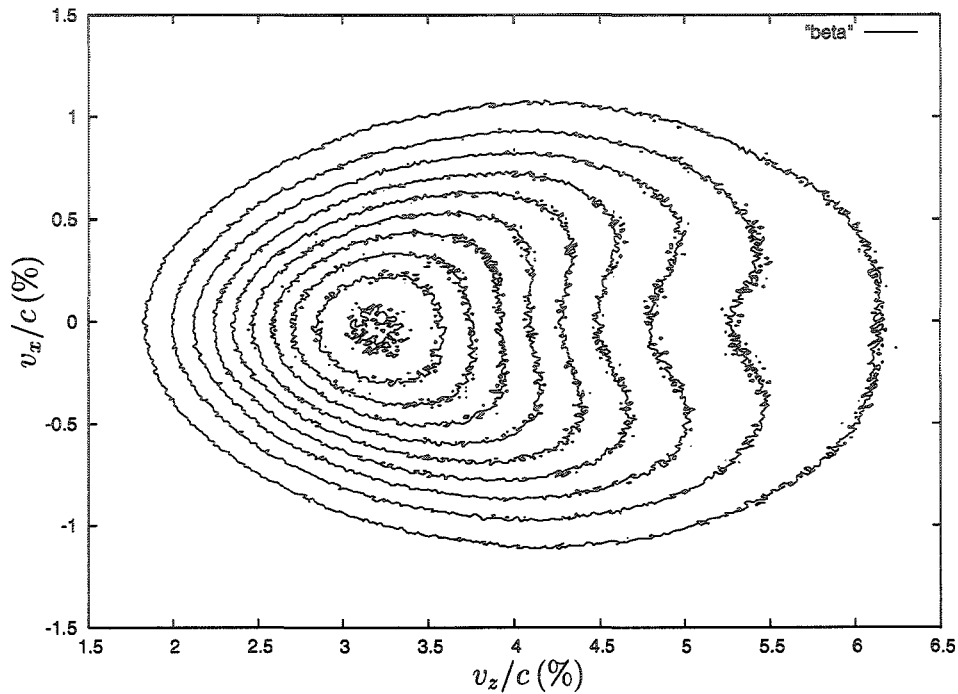


Figure 4.16: Velocity Distribution of the Recoils

The recoils receive a “kick” as each particle is emitted. Because the particle detector is more efficient at detecting forward-going particles (because they have the additional centre of mass velocity to increase their energy in the lab frame), the total recoil distribution is biased towards recoils that have been kicked upstream.

may equivalently be compared.

To ensure that the mean kick was not creating instability in the simulations, different numbers of real events averaged over for the simulations were tested. The results are shown in figure 4.17. With less than approximately 1 million events, the variation in the results is noticeable. For that reason, a minimum of 1.5 million events were used for each simulation. The bias was sampled at different times during the run to ensure that there was no change in the bias over time.

It is possible to avoid the biasing problem altogether by not fully reconstructing the events. Although that removes one potential source of problems, it introduces

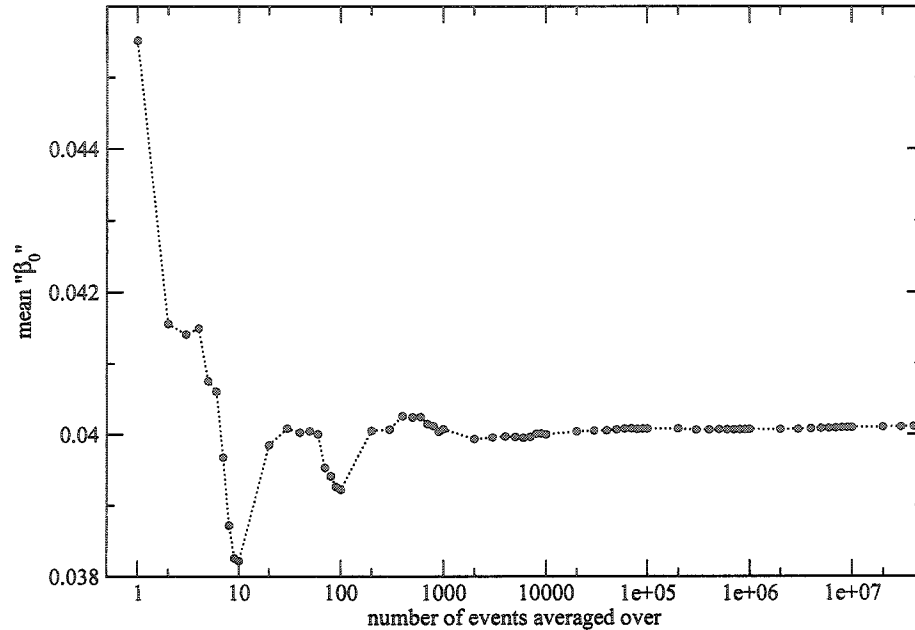


Figure 4.17: Effect of Number of Events on the Average

The number of real events included in the simulations has a considerable effect unless that number is greater than ~ 100000 . Simulations used 1.5 M events, by which point the average has stabilized completely, but the calculation time is not too high.

another. Weaker, higher-energy transitions (which is as good a way as any to describe traditional superdeformed band transitions) suffer loss of resolution in the spectra and may become unmeasurable.

Since the transitions at the very top of the band require very high H reactions, it is true that the particles detected in coincidence with those high transitions must have lower energies than average. Intuitively, this would imply that the kick given to recoils created with very high excitation energy was less than the kick given to recoils created with average excitation energies. However, because the particles in coincidence with the transitions high in the band have lower energies than average, they are less likely to be detected in the rear detectors and the average rear-ward

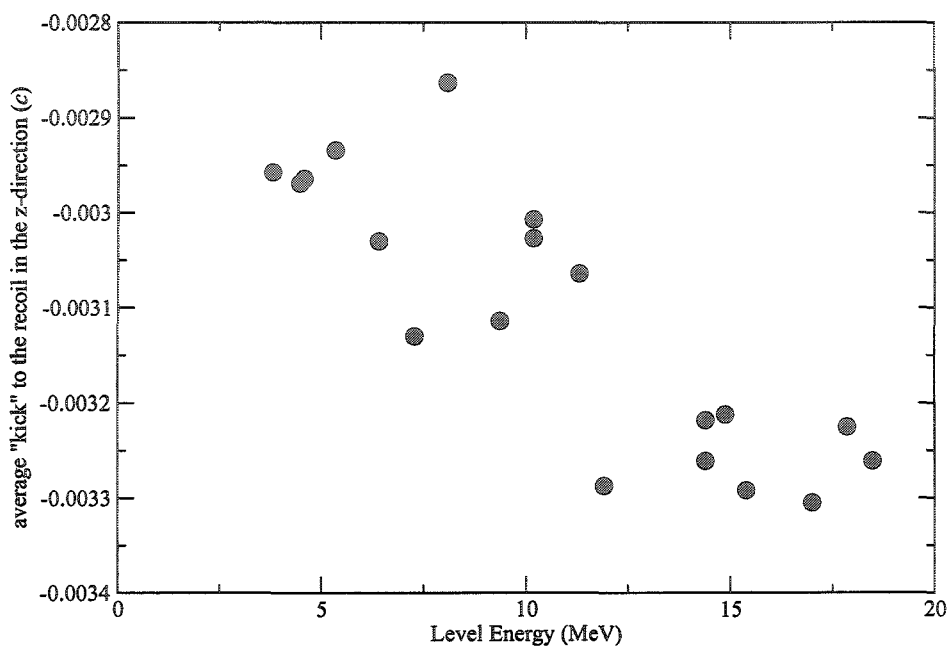


Figure 4.18: Z-direction Kicks to the Recoils

The highest- H transitions receive the greatest mean “kicks” from the departing particles, despite the fact that those particles will have, on average, lower energies than the particles which populate the recoil at lower H .

kick to the recoils is marginally *larger* than the average: $\sim 7.6\%$. This effect is illustrated in figure 4.18, which shows the increasing z-“kick” with increasing level energy. The highest energy levels must have been populated with the highest H (the close relationship between H and excitation energy at high excitation energy can be shown through H - E_γ coincidences), which have the greatest negative “kicks”.

Another possible way to explain the higher z-direction kick at higher excitation energy is to examine the profile of the total energy as a function of the target depth of the reaction. The beam loses energy as it traverses the target, so the total energy available to the reaction product varies depending on where the reaction takes place. One effect of that is that different reaction channels are produced predominately

at different positions in the target [Chi03a]. Another side effect is variation in the total energy for each channel. If the very high H events are only possible when the reaction takes place early in the target (and therefore there is more total energy available for particle evaporation and excitation energy), it is possible that the particle evaporation which leads to high excitation energy states actually have *more* energy than the majority of particles for that channel. Such an effect would be observable in that those recoils created upstream in the target would have to travel through more target than the average, and therefore would have lower exit velocities (see section 4.5.2) than the average. Figure 4.19 maps the exit velocities measured in coincidence with transitions de-exciting states of increasing excitation energy. It may be worth further exploration, given that the highest H transitions are in coincidence with exit velocities below the mean, and the lowest H transition is in coincidence with exit velocities above the mean, but in this experiment the results are not statistically significant.

The sensitivity of the detector can be discerned by an examination of the “kicks”. Figure 4.20 shows the x and y “kicks” in coincidence with the same γ rays used in figure 4.18. It is worth mentioning that there is not the energy dependence of the mean “kick” in the x and y directions seen in the z direction. The mean x and y kicks are non-zero. However, they are negligibly small, only $\sim 0.6\%$ and $\sim 0.8\%$ of the centre of mass velocity. This probably results from the beam being slightly off-centre. If the impact of the beam on the target is displaced 1 mm from the centre of the array, that will enlarge the solid angle viewed by a single MICROBALL CsI crystal in the front ring on the displacement side by 0.57% relative to its opposite crystal. Although the placement of MICROBALL inside GAMMASPHERE is very precise, the

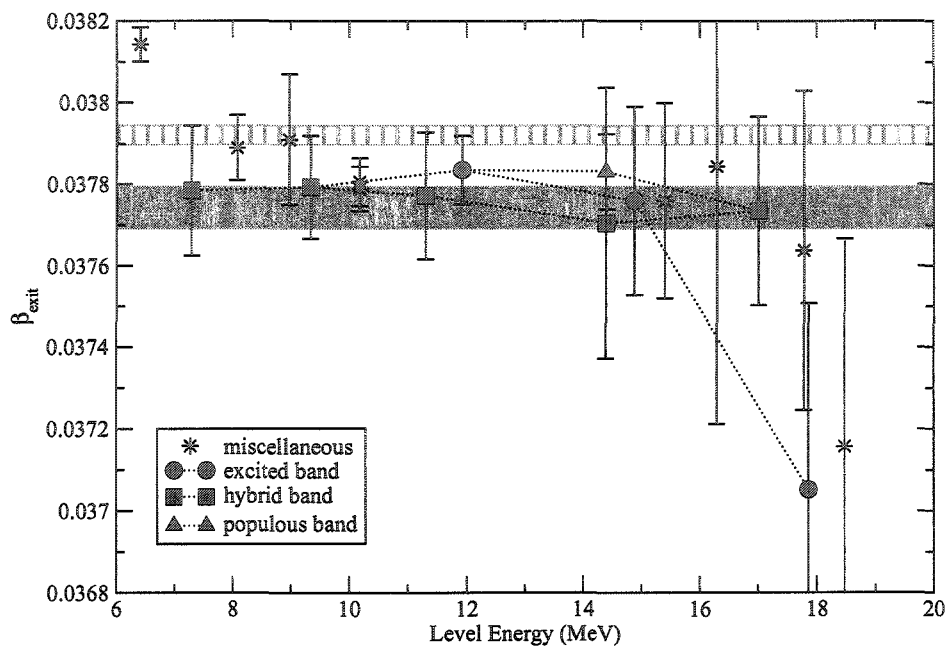


Figure 4.19: Exit Velocity

It is possible that the highest- H transitions are in coincidence with slower β_{exit} 's than the mean. Both the weighted mean β_{exit} limits (striped) and un-weighted mean limits (solid) are shown. The fact that the low β_{exit} 's at high level energies and the high β_{exit} at low energy are outside the limits of the mean is commensurate with statistical expectations.

position of the beam spot on the target can be a millimetre off centre, merely from the tuning of the beam.

4.5.2 Exit Velocity

The exit velocity is the average velocity of the recoils after they have escaped the target. The environment of the target is near-vacuum, which obviously has very little stopping effect on the recoils, so it is assumed that the velocity after exiting the target does not change. Those studying ^{38}Ar are fortunate in that there is a long(er)-lived state near the bottom of the decay scheme. The 5^- state at 4586 keV (see figure 4.1)

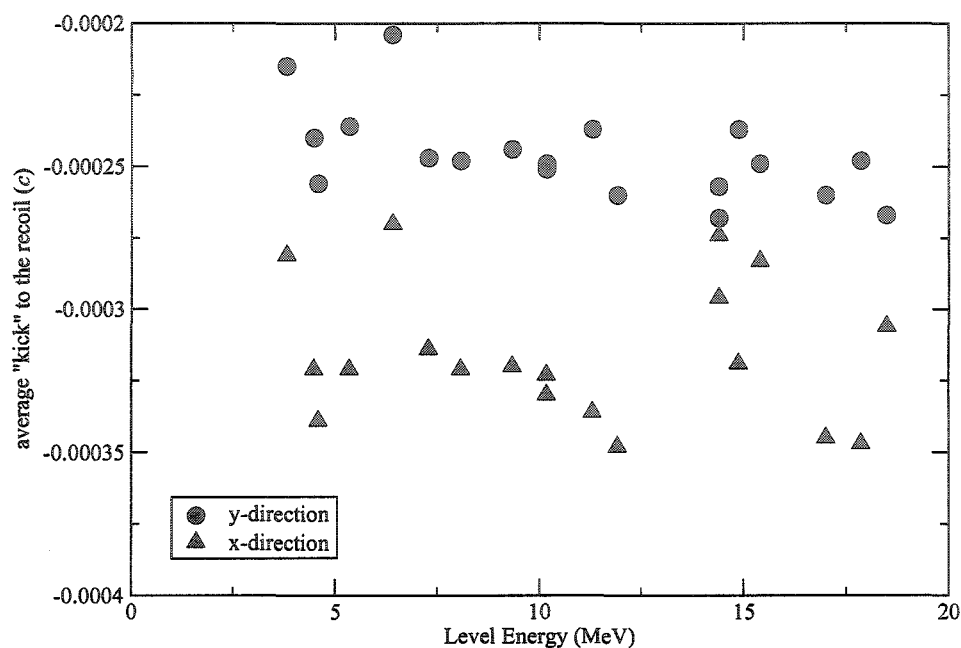


Figure 4.20: X- and Y- Direction Kicks to the Recoils

The x,y-direction “kicks” do not exhibit the same energy dependence as the z-direction kicks in figure 4.18.

has been previously determined to have a lifetime of 131 ± 2 ps. That long time should be more than ample to ensure that the recoiling nuclide has exited the target by the time any γ rays below it are emitted.

The exit velocity of the nucleus was measured through two very strong transitions below that state (at 670 and 1643 keV). Those measurements are shown in table 4.1, and they have a weighted mean $F(\tau)$ value of $(90.08 \pm 0.06)\%$ of the full shift applied. The full shift applied is a calculated quantity: It is the shift at the velocity of the compound system when it is created from a beam of the nominal energy in the centre of the nominal width of the target. The compound system then decays to the recoils that I study which naturally have velocities altered from the compound

$E_{\gamma, \text{gate}}$ (keV)	670 keV $F(\tau)$	1643 keV $F(\tau)$
1823	90.50 ± 0.14	90.69 ± 0.13
1201	89.72 ± 0.19	89.79 ± 0.19
1605	89.77 ± 0.20	89.83 ± 0.20
1669	89.91 ± 0.27	90.08 ± 0.26
4673	89.29 ± 2.26	90.36 ± 2.00
4092	89.13 ± 1.31	89.88 ± 1.31
3776	89.73 ± 0.78	89.65 ± 0.84
3593	90.14 ± 2.04	87.23 ± 1.51
2978	88.43 ± 1.47	87.52 ± 1.59
2961	89.55 ± 0.77	89.83 ± 0.79
2576	89.89 ± 0.29	89.85 ± 0.28
2050	89.75 ± 0.44	89.79 ± 0.42
2610	89.74 ± 0.77	89.51 ± 0.78
3090	89.40 ± 1.12	89.73 ± 1.12
1958	89.40 ± 0.52	90.03 ± 0.52
2474	89.81 ± 0.31	89.92 ± 0.31
4385	90.01 ± 0.54	90.09 ± 0.53

Table 4.1: $F(\tau)$ Values at Exit Velocity Measured in Different Gates

Presented here are the $F(\tau)$ values for two transitions below the 131 ps state at 4.586 MeV. The weighted mean of these $F(\tau)$ values, $(90.08 \pm 0.06)\%$, was used to determine the mean exit velocity, $(0.03792 \pm 0.00002) c$. These can be seen plotted in figure 4.19.

system velocity by the momentum from the outgoing evaporated particles. This corresponds to a velocity of $(0.03792 \pm 0.00002) c$. The data shown in figure 4.19 are statistically commensurate with all of the transitions occurring at the same mean exit velocity. That is to say that there is no reason to believe that the exit velocity is dependent on H or I .

$E_{\gamma, \text{gate}}$ (keV)	$F(\tau)\%$
2576	95.36 ± 1.20
3090	95.88 ± 2.13
2050	95.42 ± 1.25
1958	96.14 ± 2.29
2474	95.77 ± 1.06
1939	95.87 ± 1.81

Table 4.2: Initial $F(\tau)$ Values for 2610 keV Transition

When gated on the transitions indicated, the 2610 keV transition, which de-excites by the 17 MeV 14^+ state reveals these $F(\tau)$ values. This is the best measured of the high spin, high excitation energy transitions.

4.5.3 Initial Velocity

The velocity of the recoil at the instant it has been created I will refer to as the initial velocity. Although it is presumably not possible to measure the initial velocity (because the γ rays emitted by the recoil when it is created are randomly distributed in energy and therefore their Doppler shifts are not measurable), it is possible to measure the velocity of the recoils as they de-excite their highest observed discrete energy levels, and the initial velocity must be at least as large as that. The determination of initial velocity is further complicated by the fact that $F(\tau)$ values of the highest transitions in a band can only be measured from below (there being no higher transition to measure from). This introduces a risk of an influence in the measurement from side-feeding, as discussed in section 4.4.1.

The values for $F(\tau)$ for the 2610 keV transition are given in table 4.2. There is some variation in the values, and the uncertainties are large. This is because the transition is not a strong one. The weighted mean of all of the values in table 4.2 is $(95.36 \pm 0.86)\%$.

One may also attempt to determine the initial velocity through the 2978 keV transition, which de-excites the 17.9 MeV 14^+ state. A measurement from a gate on the 2961 keV transition immediately below it produces $(97.48 \pm 2.02)\%$. That $F(\tau)$ value corresponds to an initial velocity of $(0.04104 \pm 0.00085)c$. This value is in agreement with that for the 2610 keV value, but it is not as well measured as that value. However, there are indications that the mean velocity of recoils which decay through the 2978 keV transition is higher than those decaying through the 2610 keV transition. It is as though there is an unseen slightly slow transition above the 17 MeV state, or possibly that the 17.9 MeV state is only populated when the recoil is created at the upstream side of the target (following the arguments presented in section 4.5.1) and is therefore genuinely invariably travelling faster when it is created. (Recall from section 4.4 that the denominator of $F(\tau)$ is a quantity which assumes an 80 MeV beam energy.)

The evidence of the apparent slowness of the recoils emitting the 2610 keV transition (or the apparent rapidity of the recoils emitting the 2978 keV transition) comes from the $F(\tau)$ values themselves. If recoils which de-excite by the 2978 keV transition are going faster than those which de-excite by the 2610 keV transition, those recoils which de-excite via the slow 2610 keV route will be going slower than those de-exciting via the fast 2978 keV route when they pass through the 11.9 MeV 10^+ state. The 11.9 MeV state de-excites by the 2576 keV γ ray. It would be possible for the discrepancy to arise at the 14.9 MeV 12^+ state, but there is nothing exceptionally slow about that state; indeed the $F(\tau)$ value of the 2961 keV transition as measured in a gate on the 2978 keV γ ray is $(97.24 \pm 2.05)\%$, and as measured in a gate on the 3593 keV transition is $(100.24 \pm 2.61)\%$. Both of those gates are

weak transitions above the state, so the measurements have large uncertainties. If we risk contamination by side-feeding and look at the 2576 keV γ -ray gate immediately below the 2961 keV transition, the $F(\tau)$ value is $(97.76 \pm 1.16)\%$. There can be no doubt that this transition is emitted by fast recoils.

A gate on the 2978 keV transition produces an $F(\tau)$ value for the 2576 keV γ ray of $(95.80 \pm 1.59)\%$. A gate on the 2610 keV transition produces an $F(\tau)$ for the 2576 keV γ ray of $93.34 \pm 1.04\%$. The two are barely in agreement. If we then add in the information from the gates immediately below the 2978 keV and 2610 keV transitions (the 2961 keV and 2474 keV γ rays, respectively), we find that the mean value of $F(\tau)$ for the 2576 keV transition is $(96.50 \pm 0.80)\%$ for those recoils taking the fast 2978 keV route, and $(93.92 \pm 0.53)\%$ for those taking the slow 2610 keV route. We can repeat this action for other transitions further down the band. Eventually, the coincidences between distant γ rays will be too weak to support measurements, but for those where it is possible, the results are shown in table 4.3.

What table 4.3 illustrates is the significant difference in the measured $F(\tau)$ values between the fast 2961 keV route and the slow 2610 keV route. There is no evidence that the discrepancy between the values arises along the decay route; the values for both decay paths through the 2610 keV γ ray are in agreement, but they are not in agreement with those through the 2961 keV γ ray. The one exception to the disagreement is the high-uncertainty value for the 1939 keV transition.

The conclusion we reach is that there is something unseen which takes time before the recoil emits the 2610 keV γ ray. That means that the 2610 keV γ -ray $F(\tau)$ value is not a good choice as the recoil starting point. Unfortunately, it is the best measured, since it is so much stronger. In fact, only in the gate at $E_\gamma = 2961$ keV is

$E_{\gamma, \text{gate}}$ (keV)	2576 keV	2050 keV	1939 keV
2610	93.34 ± 1.04	90.91 ± 1.17	90.19 ± 1.39
2474	94.12 ± 0.62	92.07 ± 0.72	90.66 ± 1.18
3090	—	91.70 ± 1.72	90.85 ± 1.86
1958	—	91.17 ± 0.58	90.60 ± 0.78
$\langle 2610, 2474 \rangle$	93.92 ± 0.53	91.75 ± 0.61	90.46 ± 0.90
$\langle 2610, 3090, 1958 \rangle$	—	91.17 ± 0.50	90.54 ± 0.64
2978	95.80 ± 1.59	—	—
2961	96.74 ± 0.92	94.33 ± 1.17	92.08 ± 1.37
3593	96.61 ± 1.40	94.47 ± 1.57	91.44 ± 1.93
$\langle 2978, 2961 \rangle$	96.50 ± 0.80	—	—
$\langle 3593, 2961 \rangle$	96.70 ± 0.77	94.38 ± 0.94	91.86 ± 1.12

Table 4.3: Comparison of $F(\tau)$ Values

Comparison of $F(\tau)$ values for “high velocity” and “low velocity” de-excitation routes. Values of $F(\tau)$ for transitions in coincidence with both the 2610 and 2978 keV γ rays are shown. No values are given when the coincidence is too weak (e.g. $E_\gamma = 2978$ and 2050 keV) or where there is no coincidence (e.g. $E_\gamma = 1958$ and 2576 keV). The means of the $F(\tau)$ values for the four possible decay pathways are also given.

it possible to measure the $F(\tau)$ value for the 2978 keV transition. Table 4.4 gives the $F(\tau)$ values for the all of the “fast” transitions above the 2576 keV γ ray. Most of the values in table 4.4 are in agreement with the $F(\tau)$ value for the 2610 keV transition. The weighted mean of all the values in table 4.4 is $(97.80 \pm 0.72)\%$.

The question remains: What is the mean initial velocity? Clearly, not all of the recoils traverse the target at velocities as high as those listed in table 4.4. The “slow” route which de-excites via the 2610 keV transition is the preferred route for many more recoils than the “fast” route; it takes a greater portion of the intensity of the level scheme. For that reason, the value of the initial velocity calculated from the $F(\tau)$ values for the two gates immediately below the 2610 keV transition is the one in use in the analysis of this data.

$E_{\gamma, \text{gate}}$ (keV)	3593 keV	2978 keV	3781 keV	2961 keV
2576	97.05 ± 2.02	—	96.79 ± 2.45	97.76 ± 1.16
2961	99.29 ± 2.51	97.48 ± 2.02	—	—
2978	—	—	—	97.24 ± 2.05
3593	—	—	—	100.24 ± 2.61
mean	97.93 ± 1.57	97.48 ± 2.02	96.79 ± 2.45	98.17 ± 0.94

Table 4.4: Initial $F(\tau)$ Values for Transitions Above the 2576 keV Transition
 The $F(\tau)$ values for the 3593, 2978, 3781 and 3961 keV transitions according to gates on the 2576, 2961, 2978 and 3593 keV γ rays are given, along with the weighted means of the $F(\tau)$ values over all the gates.

4.5.4 Target Thickness and Beam Energy

Simulations inform us that a recoil traversing a $100 \mu\text{g}/\text{cm}^2$ target, having received the average kick from an α and two protons as measured in this experiment, will begin its journey at approximately $0.0397c$ when the beam energy was 80 MeV. That corresponds to an $F(\tau)$ of 94.24 %. Neither the “slow” nor the “fast” decay path, discussed in section 4.5.3, has $F(\tau)$ values in agreement with that value. In fact, the measured $F(\tau)$ values for the initial transitions of the recoil are all *faster* than the simulation (even when it is for a conspicuously thin target). This fact implies that at least one of the inputs to the model is faulty. The stopping powers may be to blame. They are certainly the least reliable quantity of all the inputs. However, the initial velocity is not affected by the slowing of the recoil in the target; it is only affected by the slowing of the beam in the target. Figure 4.21 shows the amount of beam energy lost in the target under the nominal conditions ($440 \mu\text{g}/\text{cm}^2$ thick target and 80 MeV beam), along with the losses if the stopping power is increased or decreased by 10% from the Northcliffe and Schilling [Nor70] values. Changing the stopping powers by 10% only changes the energy loss of the beam by 10%, which is not enough to affect

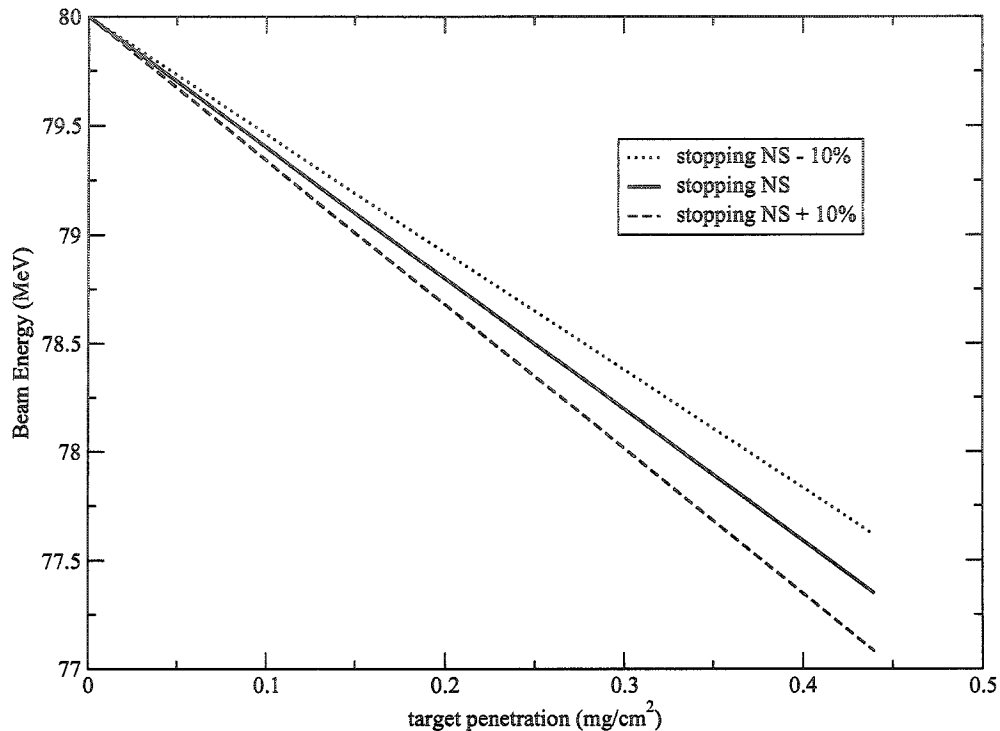


Figure 4.21: Beam Energy Loss in the Target

The beam loses energy as it passes through the target. Using the stopping powers provided by the Northcliffe and Schilling [Nor70] tables, the loss is 2.65 MeV over the entire target. Adjusting the stopping powers by 10% changes that value only by ~ 0.27 MeV.

a change in the simulated initial velocity which would bring it up to the velocities measured.

In fact, once the biased particle momentum kick has been factored into the calculations, no amount of fiddling with stopping powers will make the simulated recoils have the same velocities as the real recoils; there simply is not enough energy in the system. The particle energies and hence the kicks given to the recoils are trust-worthy. If there were a problem with the particle energy calibration it would

appear in the total energy plane. The line of total energy would be both at the wrong value, or have the wrong slope, or both. The only possible way to make the model agree with the data is to increase the beam energy input into the model.

The thickness of the target is nominally $440 \mu\text{g}/\text{cm}^2$. However, since the thickness of the target plays an important role in determining the lifetimes of the states, it is advantageous to ascertain it experimentally, with a qualitative sense of the uncertainty. Once the exit and initial velocities were established, it was necessary to determine the thickness of the target which would produce that exit velocity. Simulations of stopping in the target, using the stopping values as described in section 4.4.3, were performed for the target thicknesses 100, 200, 300, 400, 500 and $600 \mu\text{g}/\text{cm}^2$. That process was repeated for beam energies 80, 82, 84, 86, 88, and 90 MeV. Each simulation produced its own initial velocity and exit velocity.

The simulated initial velocities and exit velocities were compared to the measured initial velocity and exit velocity to find the experimental beam energy and target thickness. Figure 4.22 shows the target thickness fit as a function of beam energy for both the exit velocity and the initial velocity. The exit velocity used was derived from the mean of all values in table 4.1, and the initial velocity used was the mean values of the initial velocity of the “fast” decay, $(0.04123 \pm 0.00066)c$. The most obvious feature of figure 4.22 is that the uncertainty in the initial velocity is the source of the majority of the uncertainty in the results. The lines cross at beam energy (87.1 ± 0.9) MeV and target thickness $(446^{+97}_{-78}) \mu\text{g}/\text{cm}^2$.

The above values of the beam energy and the target thickness are obtained from the crossing points of the regressions of the data from the initial velocity and final velocity. Those regressions include the uncertainties as weights, but the beam

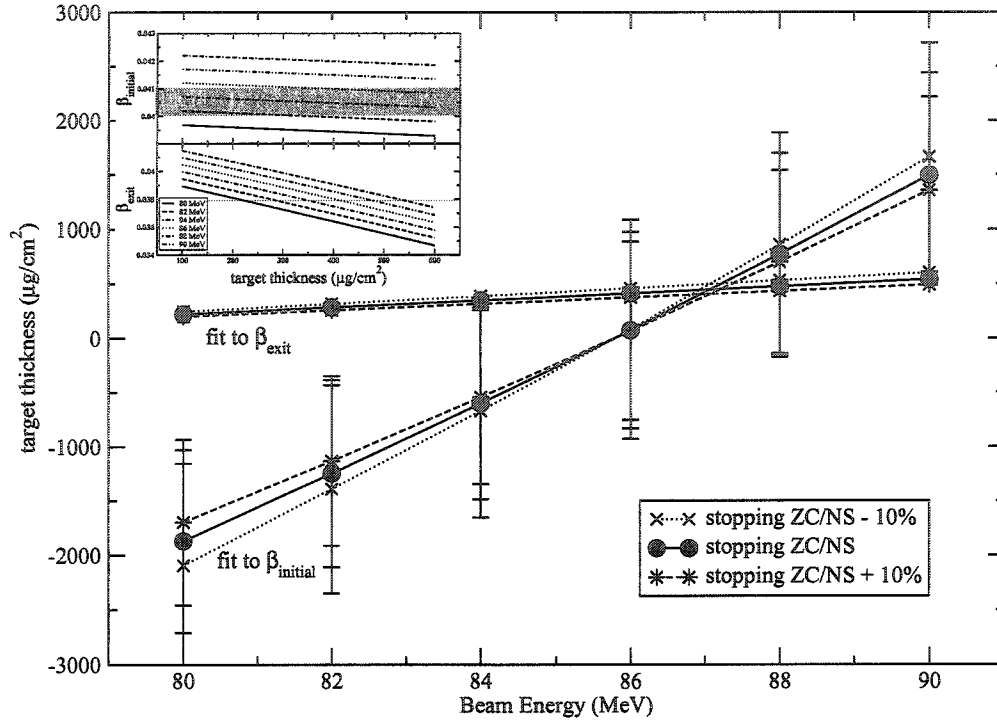


Figure 4.22: Target Thicknesses for Given Energies and Velocities

This figure shows the results of simulating beams and recoils traversing targets of varying thickness and with differing beam energies. The measured bias in the data is included in the simulations. The point at which the two lines cross is used as the target thickness and beam energy for all simulations.

energy and target thickness uncertainties do not reflect the *range* of all possible values within uncertainty, particularly those of the initial velocity. An estimation of the values, explicitly including the full range of possible values within the uncertainties of the initial velocities can be obtained by making a linear regression to the topmost and bottommost values in those ranges. The crossing points of those regressions are then determined to be at (84 ± 6) MeV and (90 ± 2) MeV. To be explicit: The absolute highest beam energy permitted within the uncertainties is 92 MeV and the

absolute lowest beam energy permitted within the uncertainties is 78 MeV. By those same rules, the absolute maximum and minimum target thicknesses permitted within uncertainties are $(3365) \mu\text{g}/\text{cm}^2$ and $(-3764) \mu\text{g}/\text{cm}^2$, respectively. This underlines the fallacy of using the absolute range of uncertainties, rather than folding the uncertainties (as weights) into the regression. The above values are in some sense valid limits. But clearly the thickness of the target must be positive and finite. The values $(87.1 \pm 0.9) \text{ MeV}$ and $(446_{-78}^{+97}) \mu\text{g}/\text{cm}^2$ will be used for beam energy and target thickness for the analysis in section 5.3.

A different approach to this problem would be to accept that the beam energy was genuinely 80 MeV. By this approach, the only important parameter is the exit velocity. The beam energy is fixed at 80 MeV, and the exit velocity of $(0.03792 \pm 0.00002) c$ then constrains the target thickness to be $(221 \pm 3) \mu\text{g}/\text{cm}^2$. This is illustrated in figure 4.23. The simulation of β_{exit} includes the average kick from the particles.

The latter approach results in a target thickness much less than the nominal value (fully half of the nominal value), which is not unusual. The target thickness is not necessarily well known by the target maker, so it is an invaluable exercise to determine the thickness from experimental parameters. The complication added in GSFMA93 of initial velocities above the highest possible recoil velocity for the nominal beam energy adds importance to this experimental determination of the target thickness.

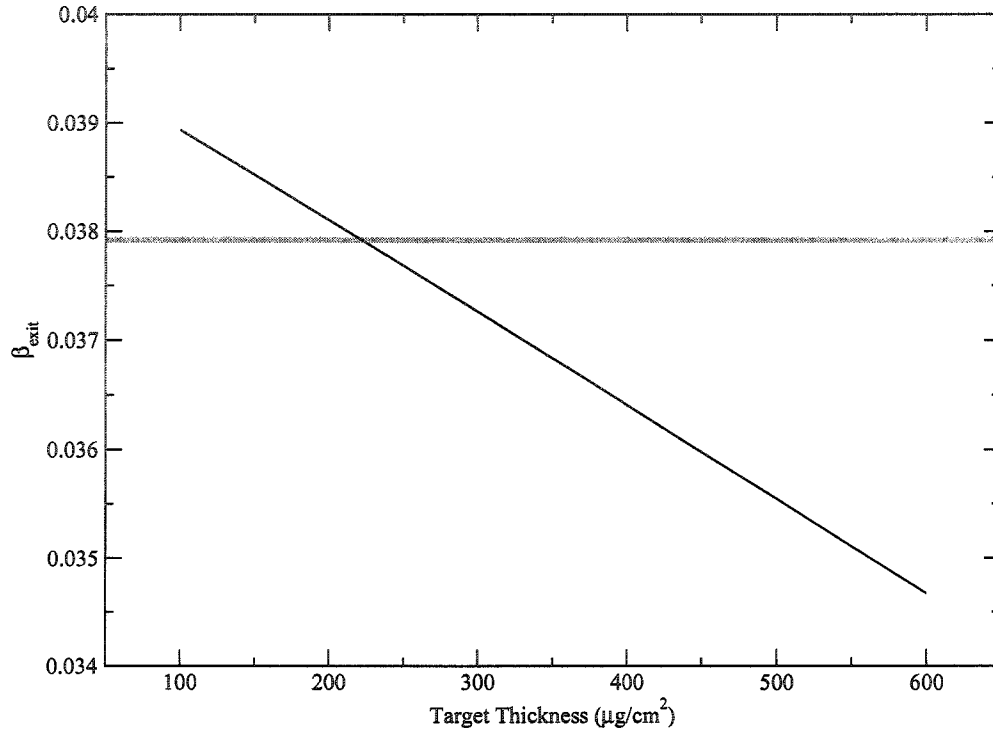


Figure 4.23: Exit Velocity and Target Thickness for 80 MeV Beam

The simulated exit velocity as a function of target thickness for a beam with energy fixed at 80 MeV is shown. The particle kick bias is included in the simulations. β_{exit} is the measured value, $(0.03792 \pm 0.00002)c$, when the target thickness is $(221 \pm 3) \mu\text{g}/\text{cm}^2$.

4.6 Sorting the Data

Matrices of γ -ray coincidence data were analysed using the computer programme ESCL8R [Rad95b]. Backgrounds were subtracted using the techniques described in [Rad95a]. Single dimension spectra were analysed with the programme GF3.

The data sorting was accomplished using a suite of codes written in-house. These codes were originally developed [Cro93] for use with a different detector, and

then were adapted [Sve96] for use with GAMMASPHERE and the MICROBALL and finally had additions to them for this particular analysis.

All the analysis was done on an event-by-event basis. Because of the event-by-event analysis, it is possible to determine the “kick” given to the recoil by the emitted particles, which enables a better Doppler correction than one based purely on the angle between the beam direction and the detector which registered the γ ray.

4.6.1 Double Gates

There was sufficient data to make double gates to resolve questions in this data set. Instead of sorting a “cube”, and attempting to properly subtract background from any spectra projected out of the cube, double γ gates were created by sorting a γ - γ matrix which had a single γ -coincidence gate applied. Any gates applied to that matrix were thus double gated. The resulting spectra were then background-subtracted according to the formula

$$S_{\gamma_1, \gamma_2}(\text{subt'd}) = S_{\gamma_1, \gamma_2} - S_{\gamma_{1\text{BG}}, \gamma_2} - \left(\frac{N(P_{\gamma_2, S_{\gamma_1}}) - N(P_{\gamma_2, S_{\gamma_{1\text{BG}}}})}{N(P_{\gamma_2, S_{\gamma_1}})} \right) S_{\gamma_1, \gamma_{2\text{BG}}}. \quad (4.9)$$

S_{γ_1, γ_2} represents a spectrum gated on both γ_1 and γ_2 . $S_{\gamma_{1\text{BG}}, \gamma_2}$ denotes a spectrum gated on the background of γ_1 and the peak at γ_2 . The number of counts in the peak at γ_2 in the total projection of a single gate on γ_1 is written $N(P_{\gamma_2, S_{\gamma_1}})$. $N(P_{\gamma_2, S_{\gamma_{1\text{BG}}}})$ indicates the number of counts in the peak at γ_2 in the total projection of a single gate on the background of γ_1 . (This makes the fraction in equation 4.9 equal to the peak-to-total ratio of γ_2 in the total projection of a single gate on γ_1 .) $S_{\gamma_1, \gamma_{2\text{BG}}}$ signifies a spectrum gated on γ_1 and the background of γ_2 .

4.7 Implementation

In this chapter I have described some of the techniques available in the analysis of measured heavy ion fusion reaction γ rays to determine lifetimes of excited states of the reaction products. Beyond the nuts and bolts of how to reduce data as measured to a form which can be interpreted, I detailed two approaches I used to solve the problem that the model simulated initial velocities lower than those measured. In the next chapter, I will present results using both methods; I will first use the constraint that the beam energy is 80 MeV and then I will remove that constraint. I also discussed the freedoms available in the simulations. The results in the next chapter arise from simulations using different combinations of those parameters, finally settling on the best combination for each of the highly deformed bands.

Chapter 5

Results

This chapter will present the level scheme of ^{38}Ar as it was determined by GSFMA93. The intensities and energies of all of the observed, placed transitions are offered in the extensive table 5.1. That table also includes the energies of the levels in the scheme, shown in figure 5.1. Some discussion of the construction of the level scheme follows.

The interpretation of the level scheme is next presented, with proposed shell-model configurations for the scheme's more outstanding features. That discussion of shell-model configurations leads to a discussion of deformed bands. The two deformed bands are separated into four decay pathways for the purposes of applying the analysis described in section 4.5 to determine the lifetimes. Three methods, of increasing degrees of freedom are engaged to illustrate the advantages and disadvantages of each.

This chapter concludes with a report of the deformation of the two highly

deformed bands in ^{38}Ar .

5.1 Level Scheme of ^{38}Ar

The single-particle nature of excitations in ^{38}Ar is evident from figure 5.1. Excitations above 4.5 MeV abound, with interactions burgeoning between diverse levels. The level scheme deduced from the data taken in GSFMA has 110 transitions and 53 levels.

Early studies of ^{38}Ar [Lie68, Gra69, Jam71, Bal72, Lin72, Bet74, Gla76, Aar79, Ker80, Bha84, Lap84] mainly used the $(\alpha, p\gamma)$ reaction from ^{35}Cl to access states in ^{38}Ar . One experiment used the inverse kinematics of that [Ker72], and another used $^{37}\text{Cl}(p, n)$ [Ald74a]. The first heavy-ion fusion-evaporation reaction to produce ^{38}Ar used N, O and F beams on Mg, Al and Si targets, and beam energy 40 MeV [Kol76]. The highest energy state observed in that experiment was the 11.6 MeV 11^- state. For many years, that state was the highest observed.

A fortunate accident enabled Rudolph *et al* [Rud02] to improve on that state of knowledge via the $^{16}\text{O}(^{32}\text{S}, \alpha 2p)$ reaction. The level scheme presented in this work is complementary to that study. Presented here is an expanded level scheme with some uncertain levels placed or re-placed. The most significant result of this thesis is the determination of the deformation of the superdeformed bands through a study of their lifetimes, which were not accessible by the serendipitous reaction on oxygen.

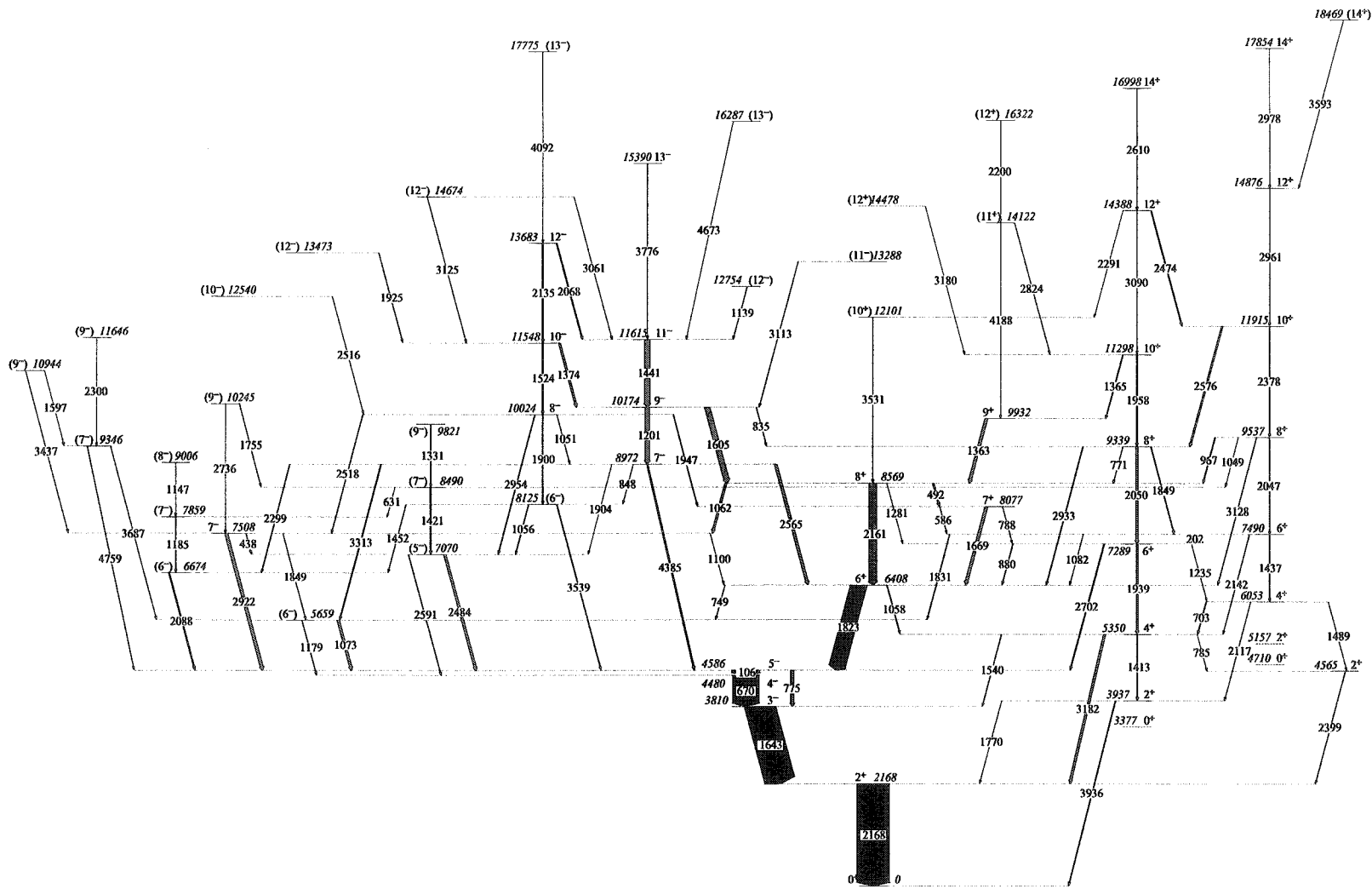
Table 5.1 lists the energies of all transitions in the level scheme. The uncertainties on the energies of the γ rays are calculated from the widths of the peaks in the spectra. Additional sources of uncertainty, such as the energy calibration or the internal consistency of the level scheme, are not included. The uncertainties on the energies of the levels, which are also given in table 5.1, do include consistency

requirements. The table is organized in order of increasing initial energy level, and it also includes the intensity of each transition. The values presented in table 5.1 were calculated by programmes in the RADWARE [Rad95b] suite.

J_i^π	J_f^π	E_i^* (keV)	E_f^* (keV)	E_γ (keV)	I_γ
2 ⁺	0 ⁺	2167.6±0.3	0	2167.56±0.03	232±6
3 ⁻	2 ⁺	3810.3±0.4	2167.6±0.3	1642.79±0.03	216±6
2 ⁺	0 ⁺	3936.5±0.5	0	3935.64±0.06	4.00±0.83
2 ⁺	2 ⁺	3936.5±0.5	2167.6±0.3	1769.7±0.1	0.58±0.02
4 ⁻	3 ⁻	4479.9±0.4	3810.3±0.4	669.61±0.03	187±6
2 ⁺	2 ⁺	4565.4±0.9	2167.6±0.3	2398.6±0.2	1.16±0.08
5 ⁻	3 ⁻	4585.9±0.4	3810.3±0.4	775.48±0.03	23.65±0.71
5 ⁻	4 ⁻	4585.9±0.4	4479.9±0.4	105.79±0.03	194±6
4 ⁺	2 ⁺	5349.9±0.4	3936.5±0.5	1413.47±0.04	5.16±0.16
4 ⁺	2 ⁺	5349.9±0.4	2167.6±0.3	3182.15±0.04	14.80±0.45
4 ⁺	3 ⁻	5349.9±0.4	3810.3±0.4	1539.82±0.07	1.80±0.06
4 ⁺	2 ⁺	5349.9±0.4	4565.4±0.9	784.5±0.2	0.13±0.01
6 ⁻	4 ⁻	5659.2±0.4	4479.9±0.4	1179.36±0.07	1.73±0.06
6 ⁻	5 ⁻	5659.2±0.4	4585.9±0.4	1073.18±0.03	17.40±0.52
4 ⁺	2 ⁺	6053.5±0.4	3936.5±0.5	2117.1±0.2	0.75±0.03
4 ⁺	2 ⁺	6053.5±0.4	4565.4±0.9	1488.5±0.1	0.53±0.02
4 ⁺	4 ⁺	6053.5±0.4	5349.9±0.4	703.44±0.03	3.25±0.10
6 ⁺	5 ⁻	6408.2±0.4	4585.9±0.4	1822.74±0.03	116±3
6 ⁺	4 ⁺	6408.2±0.4	5349.9±0.4	1058.48±0.04	3.59±0.11
6 ⁺	6 ⁻	6408.2±0.4	5659.2±0.4	749.10±0.05	0.99±0.03
6 ⁻	5 ⁻	6673.8±0.5	4585.9±0.4	2088.32±0.04	6.88±0.21
5 ⁻	4 ⁻	7069.7±0.4	4479.9±0.4	2591.4±0.1	2.05±0.07
5 ⁻	5 ⁻	7069.7±0.4	4585.9±0.4	2483.82±0.04	16.89±0.51

Table 5.1: Energies and Relative Intensities of Gamma Rays

The energies of the transitions in figure 5.1 are given, along with the level energies and the relative intensities of the gamma rays. Table continued on following pages.



Results

Figure 5.1: Level Scheme of ^{38}Ar

The level scheme of ^{38}Ar is shown. The values of energies and intensities of transitions and the energies of levels are given in table 5.1. Energies are in keV.

J_i^π	J_f^π	E_i^* (keV)	E_f^* (keV)	E_γ (keV)	I_γ
6 ⁺	5 ⁻	7288.6±0.4	4585.9±0.4	2702.37±0.05	5.28±0.16
6 ⁺	4 ⁺	7288.6±0.4	5349.9±0.4	1938.65±0.04	13.07±0.40
6 ⁺	4 ⁺	7288.6±0.4	6053.5±0.4	1235.15±0.08	0.68±0.02
6 ⁺	6 ⁺	7288.6±0.4	6408.2±0.4	880.21±0.04	3.03±0.09
6 ⁺	4 ⁺	7490.4±0.4	5349.9±0.4	2141.8±0.1	1.28±0.05
6 ⁺	6 ⁻	7490.4±0.4	5659.2±0.4	1831.16±0.06	3.04±0.10
6 ⁺	4 ⁺	7490.4±0.4	6053.5±0.4	1436.83±0.04	3.35±0.11
6 ⁺	6 ⁺	7490.4±0.4	6408.2±0.4	1081.6±0.1	0.56±0.03
6 ⁺	6 ⁺	7490.4±0.4	7288.6±0.4	201.60±0.04	0.81±0.03
7 ⁻	5 ⁻	7507.7±0.4	4585.9±0.4	2922.04±0.04	21.71±0.65
7 ⁻	6 ⁻	7507.7±0.4	5659.2±0.4	1848.83±0.09	1.36±0.05
7 ⁻	6 ⁺	7507.7±0.4	6408.2±0.4	1099.9±0.1	0.58±0.03
7 ⁻	5 ⁻	7507.7±0.4	7069.7±0.4	437.94±0.04	2.02±0.06
7 ⁻	6 ⁻	7858.9±0.6	6673.8±0.5	1185.04±0.05	2.33±0.07
7 ⁺	6 ⁺	8077.1±0.4	6408.2±0.4	1668.91±0.03	19.79±0.60
7 ⁺	6 ⁺	8077.1±0.4	7288.6±0.4	788.38±0.04	1.25±0.04
7 ⁺	6 ⁺	8077.1±0.4	7490.4±0.4	586.50±0.04	1.34±0.04

Table 5.1: (Continued) Energies and Relative Intensities of Gamma Rays
The energies of the transitions in figure 5.1 are given, along with the level energies and the relative intensities of the gamma rays. Table continued on following pages.

5.1.1 3182 & 3180 keV Doublet

The doublet of the 3182 keV transition was tentatively placed near the top of the level scheme in reference [Rud02], feeding the 14876 keV 12⁺ level. However, with the improved statistics available from this experiment, it was possible to double gate on the 3182 keV γ ray. The results of those gates are shown in figure 5.2. The 1958 keV γ ray and the 2576 keV γ ray both feed the 9339 keV 8⁺ state that the 2050 keV γ ray decays from. In the 2050/3182 keV double gate in figure 5.2c), the peak at 3180 keV is comparable in intensity to the peak at 2824 keV, and has no less

J_i^π	J_f^π	E_i^* (keV)	E_f^* (keV)	E_γ (keV)	I_γ
6 ⁻	5 ⁻	8125.1±0.5	4585.9±0.4	3539.20±0.08	3.35±0.11
6 ⁻	6 ⁻	8125.1±0.5	6673.8±0.5	1451.56±0.07	1.38±0.05
6 ⁻	5 ⁻	8125.1±0.5	7069.7±0.4	1055.64±0.04	2.59±0.08
7 ⁻	5 ⁻	8490.0±0.5	7069.7±0.4	1420.59±0.04	7.32±0.22
7 ⁻	7 ⁻	8490.0±0.5	7858.9±0.6	631.04±0.05	0.47±0.02
8 ⁺	6 ⁺	8569.3±0.4	6408.2±0.4	2161.10±0.03	56±2
8 ⁺	6 ⁺	8569.3±0.4	7288.6±0.4	1281.0±0.1	0.59±0.03
8 ⁺	7 ⁻	8569.3±0.4	7507.7±0.4	1061.55±0.03	13.90±0.42
8 ⁺	7 ⁺	8569.3±0.4	8077.1±0.4	492.23±0.03	9.57±0.29
7 ⁻	5 ⁻	8972.5±0.4	4585.9±0.4	4385.03±0.05	8.78±0.27
7 ⁻	6 ⁻	8972.5±0.4	5659.2±0.4	3312.93±0.05	5.03±0.15
7 ⁻	6 ⁺	8972.5±0.4	6408.2±0.4	2564.64±0.03	19.12±0.58
7 ⁻	6 ⁻	8972.5±0.4	6673.8±0.5	2299.14±0.06	2.45±0.08
7 ⁻	5 ⁻	8972.5±0.4	7069.7±0.4	1903.7±0.3	0.43±0.02
7 ⁻	6 ⁻	8972.5±0.4	8125.1±0.5	847.60±0.07	0.53±0.02
8 ⁻	7 ⁻	9006.2±1.2	7858.9±0.6	1147.3±0.1	0.36±0.02
8 ⁺	6 ⁺	9339.2±0.4	6408.2±0.4	2932.93±0.09	3.42±0.11
8 ⁺	6 ⁺	9339.2±0.4	7288.6±0.4	2050.48±0.03	16.19±0.49
8 ⁺	6 ⁺	9339.2±0.4	7490.4±0.4	1848.66±0.05	3.17±0.10
8 ⁺	8 ⁺	9339.2±0.4	8569.3±0.4	771.38±0.07	0.95±0.04
7 ⁻	5 ⁻	9346.0±1.3	4585.9±0.4	4759.4±0.2	1.09±0.04
7 ⁻	6 ⁻	9346.0±1.3	5659.2±0.4	3687.0±0.2	0.66±0.02
8 ⁺	6 ⁺	9536.9±0.5	6408.2±0.4	3127.6±0.1	1.42±0.05
8 ⁺	6 ⁺	9536.9±0.5	7490.4±0.4	2046.56±0.09	1.71±0.06
8 ⁺	7 ⁻	9536.9±0.5	8490.0±0.5	1048.63±0.09	0.45±0.02
8 ⁺	8 ⁺	9536.9±0.5	8569.3±0.4	967.15±0.03	3.63±0.11
9 ⁻	7 ⁻	9820.8±0.8	8490.0±0.5	1330.87±0.07	1.21±0.04
9 ⁺	8 ⁺	9932.3±0.5	8569.3±0.4	1363.04±0.03	19.57±0.59
8 ⁻	5 ⁻	10024.4±0.5	7069.7±0.4	2954.20±0.07	3.01±0.09
8 ⁻	7 ⁻	10024.4±0.5	7507.7±0.4	2517.61±0.10	1.87±0.06
8 ⁻	7 ⁺	10024.4±0.5	8077.1±0.4	1946.57±0.06	2.66±0.08
8 ⁻	6 ⁻	10024.4±0.5	8125.1±0.5	1899.69±0.04	4.64±0.14
8 ⁻	7 ⁻	10024.4±0.5	8972.5±0.4	1051.40±0.07	1.06±0.04
9 ⁻	7 ⁻	10244.8±0.9	7507.7±0.4	2736.2±0.2	0.75±0.03
9 ⁻	7 ⁻	10244.8±0.9	8490.0±0.5	1754.99±0.09	1.18±0.04

Table 5.1: (Continued) Energies and Relative Intensities of Gamma Rays
The energies of the transitions in figure 5.1 are given, along with the level energies and the relative intensities of the gamma rays. Table continued.

J_i^π	J_f^π	E_i^* (keV)	E_f^* (keV)	E_γ (keV)	I_γ
9 ⁻	8 ⁺	10174.2±0.4	8569.3±0.4	1605.08±0.03	37.38±1.12
9 ⁻	7 ⁻	10174.2±0.4	8972.5±0.4	1201.49±0.03	32.12±0.97
9 ⁻	8 ⁺	10174.2±0.4	9339.2±0.4	835.16±0.04	1.58±0.05
9 ⁻	7 ⁻	10943.7±1.8	7507.7±0.4	3437.3±0.3	0.58±0.03
9 ⁻	7 ⁻	10943.7±1.8	9346.0±1.3	1596.9±0.2	0.38±0.02
10 ⁺	8 ⁺	11297.7±0.5	9339.2±0.4	1958.45±0.04	6.84±0.21
10 ⁺	9 ⁺	11297.7±0.5	9932.3±0.5	1365.35±0.05	3.88±0.12
10 ⁻	8 ⁻	11548.4±0.5	10024.4±0.5	1523.80±0.04	6.79±0.21
10 ⁻	9 ⁻	11548.4±0.5	10174.2±0.4	1374.40±0.03	13.64±0.41
11 ⁻	9 ⁻	11614.9±0.5	10174.2±0.4	1440.67±0.03	38.71±1.16
9 ⁻	7 ⁻	11646.2±2.6	9346.0±1.3	2300.2±0.2	0.47±0.02
10 ⁺	8 ⁺	11914.9±0.5	9339.2±0.4	2576.11±0.04	10.14±0.31
10 ⁺	8 ⁺	11914.9±0.5	9536.9±0.5	2377.56±0.05	4.28±0.13
10 ⁺	8 ⁺	12100.6±1.1	8569.3±0.4	3531.3±0.1	2.62±0.09
10 ⁻	8 ⁻	12540.4±2.3	10024.4±0.5	2515.9±0.2	0.70±0.03
12 ⁻	11 ⁻	12754.2±0.7	11614.9±0.5	1139.29±0.05	1.49±0.05
11 ⁻	9 ⁻	13287.6±1.6	10174.2±0.4	3113.4±0.2	1.40±0.05
12 ⁻	10 ⁻	13473.0±0.8	11548.4±0.5	1924.88±0.07	2.21±0.07
12 ⁻	10 ⁻	13683.1±0.5	11548.4±0.5	2134.89±0.04	7.54±0.23
12 ⁻	11 ⁻	13683.1±0.5	11614.9±0.5	2068.02±0.04	6.25±0.19
11 ⁺	9 ⁺	14121.8±1.2	9932.3±0.5	4188.2±0.6	0.18±0.01
11 ⁺	10 ⁺	14121.8±1.2	11297.7±0.5	2824.2±0.1	1.14±0.04
12 ⁺	10 ⁺	14388.4±0.6	11297.7±0.5	3090.3±0.1	1.24±0.04
12 ⁺	10 ⁺	14388.4±0.6	11914.9±0.5	2473.61±0.05	5.30±0.16
12 ⁺	10 ⁺	14388.4±0.6	12100.6±1.1	2291±2	0.05±0.01
12 ⁻	10 ⁻	14674.4±1.5	11548.4±0.5	3125.1±0.2	1.07±0.04
12 ⁻	11 ⁻	14674.4±1.5	11614.9±0.5	3060.7±0.2	0.59±0.02
12 ⁺	10 ⁺	14875.7±1.2	11914.9±0.5	2960.8±0.1	1.78±0.06
13 ⁻	11 ⁻	15390.5±0.8	11614.9±0.5	3775.54±0.07	3.07±0.09
13 ⁻	11 ⁻	16286.9±9.2	11614.9±0.5	4672.6±1.0	0.11±0.01
12 ⁺	11 ⁺	16321.6±2.6	14121.8±1.2	2200.4±0.2	0.34±0.02
14 ⁺	12 ⁺	16998.5±0.9	14388.4±0.6	2610.07±0.07	2.28±0.07
14 ⁻	12 ⁻	17775.0±2.1	13683.1±0.5	4091.9±0.2	0.64±0.02
14 ⁺	12 ⁺	17853.8±3.5	14875.7±1.2	2978.2±0.4	0.28±0.02
14 ⁺	12 ⁺	18468.7±5.0	14875.7±1.2	3593.3±0.5	0.19±0.01

Table 5.1: (Concluded) Energies and Relative Intensities of Gamma Rays
The energies of the transitions in figure 5.1 are given, along with the level energies and the relative intensities of the gamma rays.

than half the intensity of the peak at 2961 keV. The 3180 keV peak is certainly larger than the peak at 2978 keV in that spectrum. In the 1958/3182 keV double gate shown in figure 5.2b), the ratio of intensities of the 2824 keV peak and the 3180 keV peak is consistent with the corresponding ratio to be found in the 2050/3182 keV double gate. However, the ratio of the intensities of the 2961 keV peak and the 3180 keV “peak” (meaning any counts to be found within the dotted line border) in figure 5.2a) is not consistent with the corresponding ratio in figure 5.2c). This evidence is exemplary. The 3090/, 2610/, 2474/, and 2961/3182 keV double gates also point to the same conclusion: The 3180 keV transition feeds the 11297 keV 10^+ level, out of which the 1958 keV γ ray decays.

5.2 Shell Model Configurations

The ground-state configuration of the 18 protons in ^{38}Ar can be deduced to be

$$\pi : (1s_{\frac{1}{2}})^2 \parallel (1p_{\frac{3}{2}})^4 (1p_{\frac{1}{2}})^2 \parallel (1d_{\frac{5}{2}})^6 (2s_{\frac{1}{2}})^2 (1d_{\frac{3}{2}})^2 \parallel \quad (5.1)$$

and that of the 20 neutrons

$$\nu : (1s_{\frac{1}{2}})^2 \parallel (1p_{\frac{3}{2}})^4 (1p_{\frac{1}{2}})^2 \parallel (1d_{\frac{5}{2}})^6 (2s_{\frac{1}{2}})^2 (1d_{\frac{3}{2}})^4 \parallel \quad (5.2)$$

As can be seen, the magic number 20 neutrons close a shell, whereas the 18 protons leave 2 holes in the $(1d_{\frac{3}{2}})$ shell.

It is educational at this point to look at the ground state spin of the neighbouring even-odd nuclei; for example ^{37}Cl and ^{37}Ar , which were both produced in this experiment. The ground state spin and parity of both is $\frac{3}{2}^+$. The paired nucleons contribute nothing to the ground state spin and parity, so all that matters is the

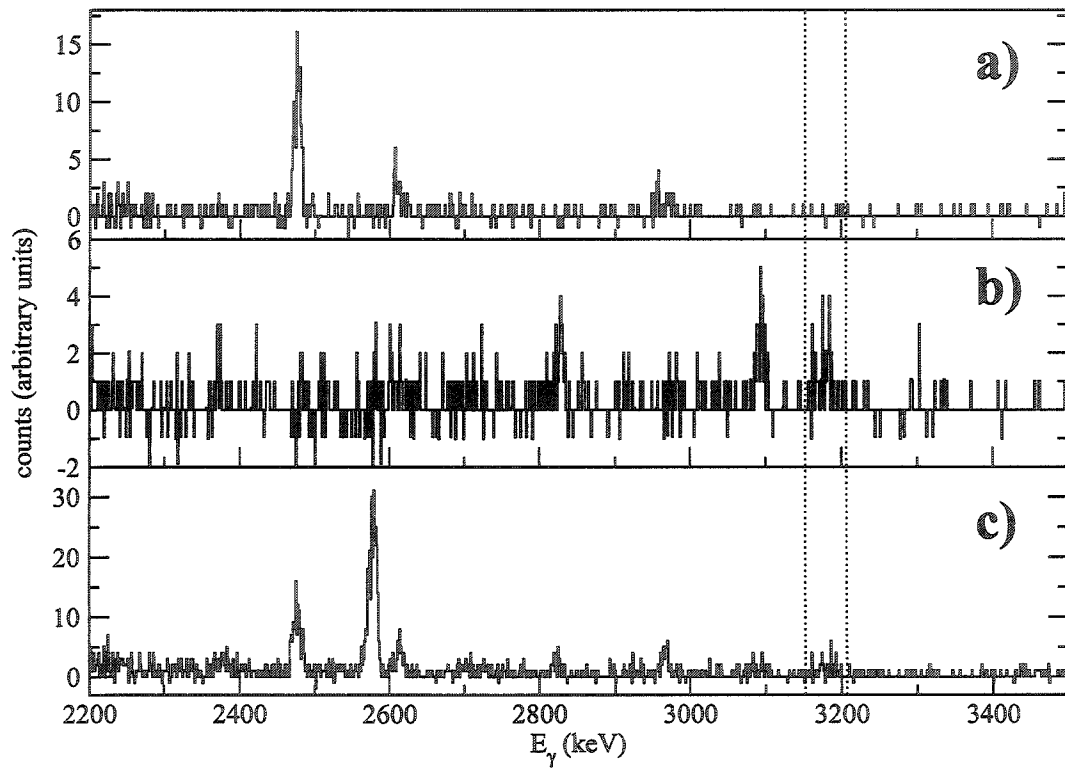


Figure 5.2: Evidence for Placement of 3183 keV Doublet

The 3182 keV doublet is shown here with double gates on the 3182 keV γ ray and γ rays at a) 2576 keV, b) 1958 keV, and c) 2050 keV. There is no evidence of the 3180 keV transition (between the dotted lines) in a), but there is in b) and c).

unpaired proton (neutron) in ^{37}Cl (^{37}Ar). The unpaired nucleon is in the $1d_{\frac{3}{2}}$ orbital, whence comes the $\frac{3}{2}$ spin, and the even parity emerges because $\ell = 2$.

Without exciting any particles out of their shells, this lowest configuration of ^{38}Ar can support $2\hbar$ units of spin.

$$+\frac{3}{2} + \frac{1}{2} = 2. \quad (5.3)$$

The first excited state of the nucleus is a 2^+ state. And we see that the energetic cost of adjusting two protons in the $1d_{\frac{3}{2}}$ shell from zero spin to maximal spin alignment is approximately 2.7 MeV.

The next step is to excite nucleons. The lowest excited states beyond the 2^+ are negative parity spin 3, 4, $5\hbar$ levels. A negative parity band with those spins can be constructed by promoting one nucleon into the $1f_{\frac{7}{2}}$ shell. Such a configuration has the possible spins and parities $I^\pi = 2^-, 3^-, 4^-, 5^-$, if the promoted nucleon is a proton. If a neutron is promoted into the $1f_{\frac{7}{2}}$ orbital, then the possible spins and parities are $I^\pi = 2^-, \dots, 7^-$. There is no candidate state for the 2^- below the 3^- state at 3.8 MeV, the lowest 2^- state (observed in previous experiments [FSB⁺96]) is at 5.1 MeV.

The next strongest band in ^{38}Ar , includes the 6.4 MeV 6^+ state and the 8.6 MeV 8^+ . A simple way to achieve that is to promote a pair of nucleons from the $1d_{\frac{3}{2}}$ shell to the $1f_{\frac{7}{2}}$ shell. Then the two nucleons each in the $(1d_{\frac{3}{2}})$ and $(1f_{\frac{7}{2}})$ orbitals can combine to angular momentum $8\hbar$. If a pair of protons is promoted, $8\hbar$ represents the maximum angular momentum. If the pair promoted is neutrons, the maximum angular momentum is $10\hbar$. Because we have already seen (from the first 2^+ state) that the energy to adjust the spins of two protons in the $1d_{\frac{3}{2}}$ orbital from zero to two units of angular momentum is ~ 2.2 MeV, and the energy difference between

the 6^+ state and the 8^+ state is almost identical to that, we may assume that the identical process was responsible for the energy difference in both cases.

One possible higher excitation arises from breaking a neutron pair at this stage

$$\begin{aligned}\pi & : (1s_{\frac{1}{2}})^2 \parallel (1p_{\frac{3}{2}})^4 (1p_{\frac{1}{2}})^2 \parallel (1d_{\frac{5}{2}})^6 (2s_{\frac{1}{2}})^0 (1d_{\frac{3}{2}})^2 \parallel (1f_{\frac{7}{2}})^2 \\ \nu & : (1s_{\frac{1}{2}})^2 \parallel (1p_{\frac{3}{2}})^4 (1p_{\frac{1}{2}})^2 \parallel (1d_{\frac{5}{2}})^6 (2s_{\frac{1}{2}})^2 (1d_{\frac{3}{2}})^3 \parallel (1f_{\frac{7}{2}})^1\end{aligned}\quad (5.4)$$

Then the $8\hbar$ contribution from the protons is complimented by a contribution of

$$+\frac{3}{2} + \frac{1}{2} - \frac{1}{2} + \frac{7}{2} = 5^* \quad (5.5)$$

units of angular momentum from the neutrons to make $13\hbar$. In this case (recalling that pairs don't contribute), the parity should be

$$(-)^2 \times (-)^3 = -. \quad (5.6)$$

There is a strong negative parity excitation above the ground band, shown in figure 5.3, but that appears to reach a maximum at 11^- , not 13^- , so perhaps that band is instead built on the configuration

$$\begin{aligned}\pi & : (1s_{\frac{1}{2}})^2 \parallel (1p_{\frac{3}{2}})^4 (1p_{\frac{1}{2}})^2 \parallel (1d_{\frac{5}{2}})^6 (2s_{\frac{1}{2}})^2 (1d_{\frac{3}{2}})^0 \parallel (1f_{\frac{7}{2}})^2 \\ \nu & : (1s_{\frac{1}{2}})^2 \parallel (1p_{\frac{3}{2}})^4 (1p_{\frac{1}{2}})^2 \parallel (1d_{\frac{5}{2}})^6 (2s_{\frac{1}{2}})^2 (1d_{\frac{3}{2}})^3 \parallel (1f_{\frac{7}{2}})^1.\end{aligned}\quad (5.7)$$

However, there is a candidate 13^- state at 15.4 MeV, which is much more weakly populated than other members of this band.

There is also a negative parity band which reaches at least as high as angular momentum $12\hbar$, shown in figure 5.4. That band could be built on the configuration

$$\pi : (1s_{\frac{1}{2}})^2 \parallel (1p_{\frac{3}{2}})^4 (1p_{\frac{1}{2}})^2 \parallel (1d_{\frac{5}{2}})^6 (2s_{\frac{1}{2}})^1 (1d_{\frac{3}{2}})^2 \parallel (1f_{\frac{7}{2}})^1$$

*At this stage, it is convenient to note that the contribution of holes is identical to the contribution of particles in an orbital.

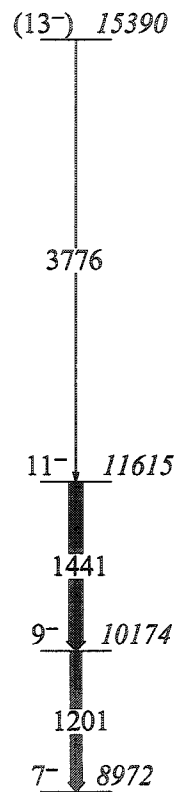


Figure 5.3: Angular Momentum 11 Negative Parity Band

This band may have a configuration with one neutron promoted to the $1f_{7/2}$ orbital from the $1d_{5/2}$ orbital. The neutron excitation is built on top of a proton excitation which has maximum angular momentum of either 8 or 6 \hbar .

$$\nu : (1s_{\frac{1}{2}})^2 || (1p_{\frac{3}{2}})^4 (1p_{\frac{1}{2}})^2 || (1d_{\frac{5}{2}})^6 (2s_{\frac{1}{2}})^2 (1d_{\frac{3}{2}})^2 || (1f_{\frac{7}{2}})^2, \quad (5.8)$$

or perhaps it is built on the configuration

$$\begin{aligned} \pi & : (1s_{\frac{1}{2}})^2 || (1p_{\frac{3}{2}})^4 (1p_{\frac{1}{2}})^2 || (1d_{\frac{5}{2}})^6 (2s_{\frac{1}{2}})^2 (1d_{\frac{3}{2}})^1 || (1f_{\frac{7}{2}})^1 \\ \nu & : (1s_{\frac{1}{2}})^2 || (1p_{\frac{3}{2}})^4 (1p_{\frac{1}{2}})^2 || (1d_{\frac{5}{2}})^6 (2s_{\frac{1}{2}})^2 (1d_{\frac{3}{2}})^2 || (1f_{\frac{7}{2}})^2, \end{aligned} \quad (5.9)$$

and 13^- state (which has the maximum possible angular momentum available) is not observed with any strength because it was at too high energy to be well populated. There is a candidate for the 13^- state at 17.8 MeV, which is also shown in figure 5.4.

5.2.1 Superdeformed Band Configurations

The superdeformed band identified in ^{36}Ar [Sve00, Sve01b, Sve01a] has been assigned the configuration

$$\begin{aligned} \pi & : (1s_{\frac{1}{2}})^2 || (1p_{\frac{3}{2}})^4 (1p_{\frac{1}{2}})^2 || (1d_{\frac{5}{2}})^6 (2s_{\frac{1}{2}})^0 (1d_{\frac{3}{2}})^2 || (1f_{\frac{7}{2}})^2 \\ \nu & : (1s_{\frac{1}{2}})^2 || (1p_{\frac{3}{2}})^4 (1p_{\frac{1}{2}})^2 || (1d_{\frac{5}{2}})^6 (2s_{\frac{1}{2}})^0 (1d_{\frac{3}{2}})^2 || (1f_{\frac{7}{2}})^2 \end{aligned} \quad (5.10)$$

which has a maximum angular momentum $16 \hbar$ and positive parity. This band is identified as a $4p - 8h$ configuration, meaning that a total of four particles (two protons, two neutrons) and eight holes (four proton holes and four neutron holes) are excited across the gap at magic number 20. Two bands have been identified in ^{40}Ca [Ide01], and they have been assigned $4p - 4h$ and $8p - 8h$ configurations. ^{38}Ar has two proton holes more than ^{40}Ca and two neutrons more than ^{36}Ar . One might therefore forecast a band in ^{38}Ar with the configuration $4p - 6h$ at the very least. Since there is more than one deformed band in ^{38}Ar , it is worth seeing if one of the others could have the configuration $6p - 8h$.

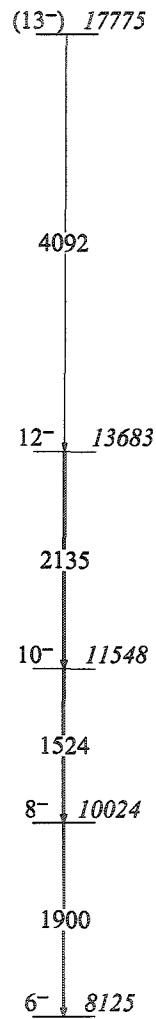


Figure 5.4: Angular Momentum 13 Negative Parity Band

This band is built on a configuration with one proton promoted from the $1d_{3/2}$ orbital to the $1f_{7/2}$ orbital, and a pair of neutrons promoted in the same way.

The earliest identification of a deformed band in ^{38}Ar [Bet74] suggested that the band, called the yrast deformed band in this work (which, until the work of Rudolph *et al* [Rud02], reached only as high as spin 8) was based on a $4p - 6h$ configuration, as predicted by a calculation by Skouras [Sko70]. Interestingly, later works [Kol76, Lap84] deduced that there was no rotational deformed band by re-assigning the spins of the members of the band on the basis of their populations.

There are a number of different ways to assign levels to highly deformed bands. These ways are shown in figure 5.5. There is an yrast band:

I_i	I_f	E_i^* (MeV)	E_γ (keV)
14	12	17.00	2610
12	10	14.39	3090
10	8	11.30	1958
8	6	9.34	2050
6	4	7.29	1939
4	2	5.35	1413
(2)	(0)	(3.40)	(360)

However, the yrast band as described above was not the most intense in this experiment. The most common decay from the 17 MeV 14^+ state goes through the 11.91 MeV 10^+ state, instead of the 11.30 MeV 10^+ state. This is the populous band:

I_i	I_f	E_i^* (MeV)	E_γ (keV)
14	12	17.00	2610
12	10	14.39	2474
10	8	11.91	2576
8	6	9.34	2050
6	4	7.29	1939
4	2	5.35	1414
(2)	(0)	(3.40)	(360)

That 11.91 MeV 10^+ is also included in the decay from a more excited 14^+ state, which seems to be a member of an excited band.

I_i	I_f	E_i^* (MeV)	E_γ (keV)
14	12	18.47	3593
12	10	14.88	2961
10	8	11.91	2378
8	6	9.54	2046
6	4	7.49	1437
(4)	(2)	(6.06)	(898)
(2)	(0)	(5.16)	(447)

Unfortunately, there are not sufficient measurable transitions in that band to do any statistically significant fitting of the lifetimes. I will also name a hybrid band, which originates in the excited band and decays through the lower states of the yrast band:

I_i	I_f	E_i^* (MeV)	E_γ (keV)
14	12	17.85	2978
12	10	14.88	2961
10	8	11.91	2576
8	6	9.34	2050
6	4	7.29	1939
4	2	5.35	1414
(2)	(0)	(3.40)	(360)

These four “bands” have been subjected to the same analysis, wherever possible.

Figure 5.5 illustrates that there are two bands with four different decay paths between them. I have focused on those four “bands” identified above because the determination of lifetimes is based on the decay paths.

The highest-spin $4p - 6h$ configuration in ^{38}Ar is

$$\begin{aligned}
 \pi & : (1s_{\frac{1}{2}})^2 \parallel (1p_{\frac{3}{2}})^4 (1p_{\frac{1}{2}})^2 \parallel (1d_{\frac{5}{2}})^6 (2s_{\frac{1}{2}})^0 (1d_{\frac{3}{2}})^2 \parallel (1f_{\frac{7}{2}})^2 \\
 \nu & : (1s_{\frac{1}{2}})^2 \parallel (1p_{\frac{3}{2}})^4 (1p_{\frac{1}{2}})^2 \parallel (1d_{\frac{5}{2}})^6 (2s_{\frac{1}{2}})^2 (1d_{\frac{3}{2}})^2 \parallel (1f_{\frac{7}{2}})^2
 \end{aligned} \tag{5.11}$$

which has a maximum spin $16 \hbar$. The $6p - 8h$ configuration with the greatest angular momentum is

$$\begin{aligned}
 \pi & : (1s_{\frac{1}{2}})^2 \parallel (1p_{\frac{3}{2}})^4 (1p_{\frac{1}{2}})^2 \parallel (1d_{\frac{5}{2}})^6 (2s_{\frac{1}{2}})^0 (1d_{\frac{3}{2}})^2 \parallel (1f_{\frac{7}{2}})^2 \\
 \nu & : (1s_{\frac{1}{2}})^2 \parallel (1p_{\frac{3}{2}})^4 (1p_{\frac{1}{2}})^2 \parallel (1d_{\frac{5}{2}})^6 (2s_{\frac{1}{2}})^0 (1d_{\frac{3}{2}})^2 \parallel (1f_{\frac{7}{2}})^4
 \end{aligned} \tag{5.12}$$

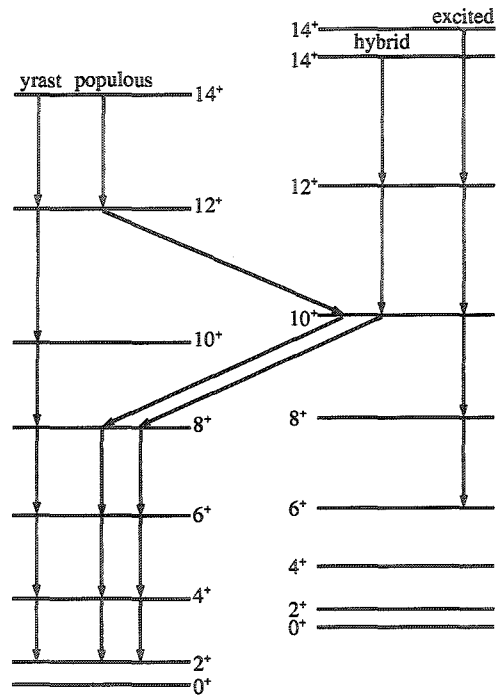


Figure 5.5: Schematic of Levels in Deformed Bands

This figure shows schematically how decays and levels fall into the bands named in section 5.2.1. Note that “yrast” is irregular compared to “excited”, but not many transitions in “excited” were actually observed in this experiment. Neither band follows the “rules” according to equation 2.12.

which terminates at spin $18 \hbar$.

No bands in ^{38}Ar were observed to beyond $14 \hbar$. This probably results from the energetics of the reaction, rather than an effect of the terminating angular momenta of the bands. The total energy available to the $\alpha 2p$ channel was ~ 40 MeV, of which ~ 27 MeV is usually dedicated to the kinetic energies of the particles. That leaves only 13 MeV for the excitation energy of the recoil. Since the lowest spin 14 state is at 17 MeV, it can be no surprise that it was not often populated. The minimum sum of particle kinetic energy for the $\alpha 2p$ channel was ~ 20 MeV, which means that those few highest H events were populating ^{38}Ar at only ~ 1.5 MeV above the most energetic discrete level observed. With so little excitation energy available (keeping in mind that the transition energies at these excitations are between 2.5 and 3 MeV), it can be no surprise that spin 16 or 18 states were not observed.

5.3 Lifetimes

In order to determine the lifetimes of the states in this nucleus a number of approaches were used. The simplest way to use DSAM to find lifetimes of the states in the highly-deformed bands is to take the single exit velocity fit from section 4.5.2 for the target thickness as an input to the simulations, as described in section 4.4 and find the constant quadrupole moment that best describes the band. Figure 5.6 shows the results of such a procedure for the three bands which have measurements of $F(\tau)$ values for six decays. Only four decays of the fourth band were measurable, and that, combined with the very high measured $F(\tau)$ values, made the fitting under these circumstances impossible.

The lifetime fits produced by this “simple” method are given in table 5.2.

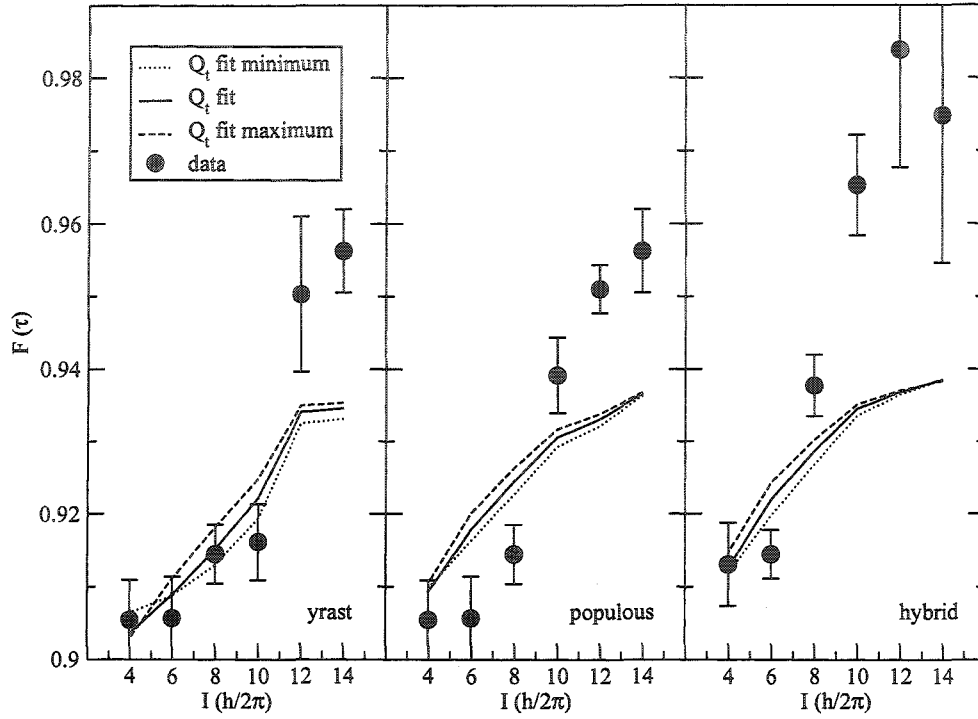


Figure 5.6: “Simple” Fit of $F(\tau)$ Values

The fits of $F(\tau)$ values from the simulations of the decay sequences through a target with a thickness only determined through measurement of the exit velocity for the three “bands” are shown.

The high uncertainty in the quadrupole moments reflects the high uncertainties in the lifetimes. A glimpse at figure 5.6 shows that those high uncertainties are justified. There exist previous lifetime measurements for three of the states measured here [Jam71, Bet74, Ald74b, Lap84]. This method reproduces the previously measured lifetime, (27 ± 13) fs, for the 6^+ 7.29 MeV state, and it does so for all three bands. However, it reproduces neither the lifetime of the 4^+ 5.35 MeV state, nor that of the 8^+ 9.34 MeV state, which were previously measured to be (140 ± 25) fs and (73 ± 18) fs respectively.

The fits in figure 5.6 are not convincing. The reduced χ^2 values for the fits

I_i	I_f	E_γ (keV)	B.R.	τ (fs)
Yrast $Q_t = 1.5 \pm 0.5$ eb				
14	12	2610.07 ± 0.07	1	8 ± 3
12	10	3090.3 ± 0.1	0.1881 ± 0.0089	0.7 ± 0.3
10	8	1958.45 ± 0.04	0.6472 ± 0.0246	24 ± 10
8	6	2050.48 ± 0.03	0.6126 ± 0.0224	19 ± 8
6	4	1938.65 ± 0.04	0.5914 ± 0.0214	25 ± 10
4	2	1413.47 ± 0.04	0.2353 ± 0.0091	53 ± 21
Populous $Q_t = 1.9 \pm 0.3$ eb				
14	12	2610.07 ± 0.07	1	5 ± 2
12	10	2473.61 ± 0.05	0.7985 ± 0.0328	6 ± 2
10	8	2576.11 ± 0.04	0.7122 ± 0.0276	4 ± 1
8	6	2050.48 ± 0.03	0.6126 ± 0.0224	12 ± 4
6	4	1938.65 ± 0.04	0.5914 ± 0.0214	16 ± 5
4	2	1413.47 ± 0.04	0.2353 ± 0.0091	33 ± 10
Hybrid $Q_t = 2.0 \pm 0.4$ eb				
14	12	2978.2 ± 0.4	1	2 ± 1
12	10	2960.8 ± 0.1	1	3 ± 1
10	8	2576.11 ± 0.04	0.7122 ± 0.0276	4 ± 2
8	6	2050.48 ± 0.03	0.6126 ± 0.0224	10 ± 4
6	4	1938.65 ± 0.04	0.5914 ± 0.0214	14 ± 6
4	2	1413.47 ± 0.04	0.2353 ± 0.0091	30 ± 12

Table 5.2: "Simple" Fit of the Transition Quadrupole Moments

The lifetimes produced when the "standard" method is applied. The lifetimes of the same states determined by fitting different bands (i.e., the transitions between 8^+ and 2^+) are all in agreement. There is very good agreement between the two measurements of the populous band and the hybrid band 10^+ state lifetime.

range between 3.7 and 11.0. This is to be expected, since this method of fitting relies both on the band having a constant quadrupole moment throughout, and on the nominal beam energy. There is so much interaction between the bands and the rest of the structure that it is unreasonable to impose a constant quadrupole moment

on them. We have already argued in section 4.5.4 that there is reason to allow the beam energy to vary in the simulations beyond its nominal value. After rejecting the constant quadrupole moment condition, the next step is to allow the quadrupole moment to vary smoothly through the band but keep the beam energy input at the nominal value. It is not possible to take this step with these data because the transitions at high angular momenta (those with velocities higher than the simulated initial velocity) drive the fits towards $Q_t = \infty$, so there is no minimum in χ^2 . Since it is the simulated initial velocity that is causing the fits to fail, a new simulation must be performed, with the beam energy fit as in section 4.5.4.

Fits with the beam energy set to (87.1 ± 0.9) MeV and the target thickness set to 446_{-78}^{+91} $\mu\text{g}/\text{cm}^2$ produce better reduced χ^2 values than the previous fits, even before the quadrupole moment is allowed to vary within the band. Permitting change in the quadrupole moment for many of the bands, permits even greater reductions of the χ^2 values.

The yrast band, however, is fit well without much variation of the quadrupole moment. Compare figure 5.7 and table 5.3 to figure 5.6 and table 5.2. The very slight, (less than its uncertainty), change in the quadrupole moment is positive with decreasing spin. This can indicate a couple of things, neither of which is an actual increase in the deformation of the nucleus as it de-excites. The first possibility is that the fit, with $\Delta Q_t < \sigma(\Delta Q_t)$, indicates simply that the transition quadrupole moment within the band is actually static. In that case, it is probably best to assign the quadrupole moment the value 6.7 ± 0.6 eb, which is the best fit when ΔQ_t is constrained to be 0. That fit, which has a reduced χ^2 only 0.04 greater than the reduced χ^2 for the varying Q_t fit, is shown in figure 5.8. The second possibility

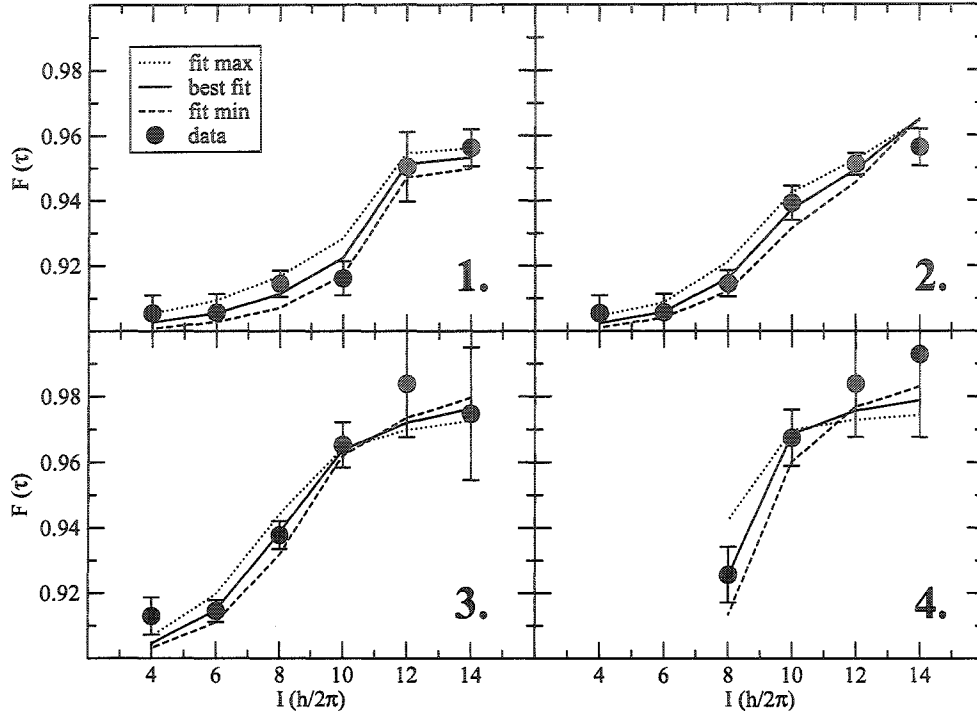


Figure 5.7: Smoothly Varying Q_t Fits of Deformed Bands

Fits varying the parameters Q_t and ΔQ_t for the four bands are shown. See table 5.3 for the values. Extreme fits from simulations with different thicknesses, stopping powers and beam energies are also shown. Graphs 1., 2., 3., and 4. represent the data of the yrast band, the populous band, the hybrid band, and the excited band, respectively.

is that the yrast band has some gamma deformation, which gradually decreases as the structure nears ground. Unfortunately, there is no way to measure γ deformation directly, so the choice between those two hypotheses remains. If the band has constant deformation, and a γ deformation which reduces to zero at the bottom of the band, the value of γ at the top of the band is $\sim 19^\circ$.

The deformation of the yrast band, if we assume that there is no γ deformation,

Band	I_i	I_f	E_γ (keV)	Q_t (eb)	τ (fs)
Yrast	14	12	2610.07 ± 0.07	$0.64^{+0.18}_{-0.13}$	47^{+27}_{-19}
	12	10	3090.3 ± 0.1	$0.68^{+0.18}_{-0.17}$	3^{+2}_{-2}
	10	8	1958.45 ± 0.04	$0.72^{+0.18}_{-0.20}$	106^{+54}_{-58}
	8	6	2050.48 ± 0.03	$0.76^{+0.18}_{-0.23}$	74^{+36}_{-45}
	6	4	1938.65 ± 0.04	$0.80^{+0.18}_{-0.26}$	90^{+41}_{-60}
	4	2	1413.47 ± 0.04	$0.84^{+0.18}_{-0.29}$	175^{+76}_{-124}
Populous	14	12	2610.07 ± 0.07	$0.93^{+0.24}_{-0.18}$	22^{+12}_{-8}
	12	10	2473.61 ± 0.05	$0.84^{+0.20}_{-0.16}$	29^{+14}_{-11}
	10	8	2576.11 ± 0.04	$0.75^{+0.16}_{-0.14}$	27^{+12}_{-10}
	8	6	2050.48 ± 0.03	$0.66^{+0.12}_{-0.12}$	95^{+35}_{-33}
	6	4	1938.65 ± 0.04	$0.58^{+0.08}_{-0.10}$	169^{+48}_{-57}
	4	2	1413.47 ± 0.04	$0.49^{+0.04}_{-0.08}$	502^{+90}_{-157}
Hybrid	14	12	2978.2 ± 0.4	$1.50^{+0.48}_{-0.32}$	4^{+3}_{-2}
	12	10	2960.8 ± 0.1	$1.29^{+0.39}_{-0.28}$	6^{+4}_{-3}
	10	8	2576.11 ± 0.04	$1.08^{+0.31}_{-0.23}$	13^{+7}_{-6}
	8	6	2050.48 ± 0.03	$0.87^{+0.22}_{-0.18}$	55^{+28}_{-24}
	6	4	1938.65 ± 0.04	$0.66^{+0.13}_{-0.14}$	129^{+52}_{-54}
	4	2	1413.47 ± 0.04	$0.45^{+0.04}_{-0.09}$	593^{+121}_{-246}
Excited	14	12	3593.3 ± 0.5	$2.1^{+1.2}_{-0.6}$	$0.8^{+0.9}_{-0.5}$
	12	10	2960.8 ± 0.1	$1.5^{+0.9}_{-0.5}$	4^{+5}_{-3}
	10	8	2377.56 ± 0.05	$0.9^{+0.6}_{-0.4}$	11^{+13}_{-9}
	8	6	2046.56 ± 0.09	$0.3^{+0.2}_{-0.2}$	159^{+248}_{-251}

Table 5.3: Lifetimes from Fits of Smoothly Varying Quadrupole Moments

The transition quadrupole moments and lifetimes from the fits shown in figure 5.7 are presented. The lifetimes for the three previously measured states as fit in the yrast band are in agreement with the previous measurement.

is not very great. $Q_{20} = (6.7 \pm 0.6)$ eb leads to $\beta_2 = (0.30 \pm 0.03)$, and $Q_{20} = 8.4^{+0.18}_{-0.29}$ eb results in $\beta_2 = 0.38^{+0.08}_{-0.13}$, neither of which indicates superdeformation. The latter value is just in agreement with a 3 : 2 axis ratio, but it would be overly optimistic to declare that to be the case. Accepting that the deformation of the yrast band is $\beta_2 = (0.30 \pm 0.03)$, the axis ratio is 1.3 ± 0.3 . This is in agreement with the value of $1.38^{+0.09}_{-0.07}$ deduced in [Bet74].

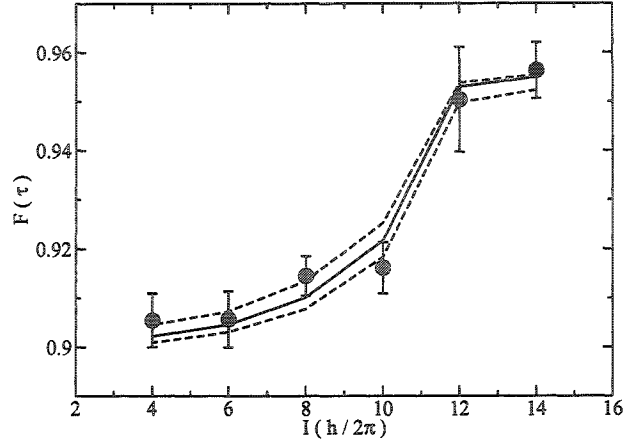


Figure 5.8: Fit of Yrast Deformed Band with Quadrupole Moment Constant
 In this fit of the yrast band the quadrupole moment is constrained to be unchanging. This does not produce a significantly different fit to that shown in figure 5.7, and has the advantage over that one of having fewer parameters.

I_i	I_f	E_γ (keV)	τ (fs)
14	12	2610.07 ± 0.07	42^{+8}_{-6}
12	10	3090.3 ± 0.1	$3.5^{+0.7}_{-0.5}$
10	8	1958.45 ± 0.04	120^{+23}_{-8}
8	6	2050.48 ± 0.03	93^{+18}_{-14}
6	4	1938.65 ± 0.04	124^{+24}_{-18}
4	2	1413.47 ± 0.04	264^{+51}_{-40}

Table 5.4: Lifetimes of the Yrast Band

For the fit to the above lifetimes, the quadrupole moment was constrained to be (6.7 ± 0.6) eb. Note that the lifetimes fit by this method are in agreement with those in table 5.3, but these possess smaller uncertainties.

The populous band, which is an excitation of the yrast band, is slightly more deformed, as expected. In that case, the deformation at the top of the band (assuming no γ deformation) is $\beta_2 = 0.42^{+0.11}_{-0.08}$, which is more in line with a 3 : 2 axis ratio.

In figure 5.7 (2), the highest energy transition of the populous band is not well fit, although the other transitions are very well fit. This may be an indication that

there is an unseen transition at the top of the band which continues the excitation of the yrast band. It may also be evidence of a γ deformation which begins near the top of the band. It is also possible that the designation of this particular combination of transitions as a band is inappropriate. The three transitions near at the bottom of the band are very well fit within the context of the yrast band and perhaps this excitation of the yrast band has a different, still more excited path to ground which is too high above yrast to have been populated here. The fact that the fits of the yrast band and the yrast band excitation lead to lifetimes of those states which do not agree for the $4^+ \rightarrow 2^+$ transition may be an indication that when the transition between the yrast excitation and the yrast band takes place, there is some non-smooth change in the quadrupole moment. For example, perhaps above the 2050 keV transition the variation in transition quadrupole moment is different than it is below that transition. With only six γ rays to extract information from, it is not possible to determine that satisfactorily. Three (or two, if we consign the 2610 keV γ ray to the yrast band alone) transitions are not sufficient for meaningful fitting.

That is of course why the third, most excited band is fit both with a decay path through the yrast states (as though they are part of the same structure) as well as through the second, less populous pathway. Both fits produce high deformations. What we have been calling the hybrid band has a value of $\beta_2 = 0.68_{-0.14}^{+0.22}$; an axis ratio between 5 : 3 and 2 : 1. If we remove the condition that this band be anchored to the yrast band, and instead attempt a fit with the four transitions we can measure in the excited band, still greater deformation is dictated. If we assume no γ deformation, the transition quadrupole moment $Q_t = 2.1_{-0.6}^{+1.2}$ at the top of the excited band corresponds to a value of $\beta_2 = 0.95_{-0.27}^{+0.54}$, which actually represents an axis ratio greater than 2 : 1,

Band	I_i	I_f	E_γ (keV)	Q_t (eb)	τ (fs)
Yrast	14	12	2610	0.70	40
	12	10	3090	0.38	11
	10	8	1958	0.51	206
	8	6	2050	2.18	9
	6	4	1939	0.56	178
	4	2	1414	6.02	3
Populous	14	12	2610	0.70	40
	12	10	2474	1.47	10
	10	8	2576	0.77	26
	8	6	2050	0.55	137
	6	4	1939	0.60	154
	4	2	1414	6.18	3
Hybrid	14	12	2981	1.23	7
	12	10	1958	∞	0
	10	8	2576	1.01	15
	8	6	2050	0.82	62
	6	4	1939	0.65	132
	4	2	1414	3.89	8
Excited	14	12	3593	∞	0
	12	10	2961	∞	0
	10	8	2378	0.71	18
	8	6	2046	0.32	149

Table 5.5: Fits to the Q_t of Individual Transitions

Infinity appears in the table when the measured $F(\tau)$ of a transition is greater than that of the transition preceding it. Infinite quadrupole moments also arise from $F(\tau)$ measurements larger than the simulated $F(\tau)$.

although it is in agreement with that value, as well. Recall from table 5.2 that the value of the quadrupole moment of the hybrid band is $Q_t = 2.0 \pm 0.4$, if the quadrupole moment is constant. Clearly, with only four measurable transitions, the uncertainties on this band are necessarily very great indeed. However, there can also be no doubt that the band is very deformed.

There is yet a third way to fit the quadrupole moments of the transitions.

Rather than assuming that there is a smooth change in the quadrupole moment throughout the band, it is possible to fit a quadrupole moment to each transition individually. This wreaks havoc on the statistics, since of course there is no way of testing the quality of a fit to a single point. However, some useful information may be extracted from such a technique, as long as it is borne in mind that the results are more qualitative than quantitative. It is standard practice to assign an uncertainty to the results which reflects only the uncertainties in the measurement of the $F(\tau)$ value and not (obviously) those in the fit. Although this does give a lower bound on the error bars, it can be misleading and I will not follow that practice here[†].

Table 5.5 presents the fits of transition quadrupole moment to the individual transitions within the band. The choice of decay chain affects the results, since the answer for each transition depends on those for all preceding transitions. Some of the transitions are un-fittable by this technique, either because the actual $F(\tau)$ value measured is greater than that simulated, or because it is greater than the one before it. In both of those cases, it is safe to assume that the lifetime is very small indeed and leave it at that. The lifetime of the 17.0 MeV state which decays by the 2610 keV γ ray is comparatively long, because of the assumption that the velocity of the recoil when it was created is the velocity of the recoils when they de-excite from the “fast” 17.9 MeV state, as discussed in section 4.5.3.

There are two salient features of the data in table 5.5. The 1414 transition is consistently predicted to be emitted after a short lifetime; shorter than its predeces-

[†]In fact, under these circumstances the only way to find uncertainties which will translate honestly to uncertainties in the lifetime is to find the greatest or least *changes* in $F(\tau)$ values, rather than merely treating the max/min of the $F(\tau)$ values in the same way as the $F(\tau)$ values themselves. Having attempted such a treatment myself, and found that it very quickly leads to lifetimes anywhere in the range of 0 to ∞ , I have decided that this method is best left qualitative.

sors. The intensity passing through that state is in bulk carried away by the 3182 keV transition to the ground band 2^+ state.

5.4 Summary

Section 5.3 presents the results of three different methods of lifetime calculation in four separate band-like entities. As explained in section 5.2.1, the motivations for defining four “bands” can mainly be found in a desire for good statistics. Now that the calculations are complete, I will discuss the yrast band and the excited band, which I believe are two separate (but interacting) structures.

Unlike the example of heavy-ion superdeformation presented in section 2.2, the superdeformation in ^{38}Ar does not reveal itself in a “picket-fence” (ΔE_γ constant) spectrum, illustrated in table 5.6. The irregularity of the gamma-ray spacings is a manifestation of the single-particle attributes of the band. The two units of angular momentum different between states is gained via rearrangements of orbitals which, for such a light nucleus, cannot be assumed. Shifting the occupations of the orbitals, when there are so few particles to bear the weight of the shift, is an upheaval. Individual shells assert their characters with every transition.

Another manifestation of the single-particle attributes of the bands is the interaction between the deformed bands and the rest of the structures in the nucleus. The traditional picture of superdeformation has the band floating isolated from the rest of the structure. Nothing could be farther from the case here. One could say that this is because the bandhead is so low in energy that the superdeformed bands are barely excited relative to the normal deformed structure. The truth is that two states reasonably close in energy and spin will not have transitions between them unless the

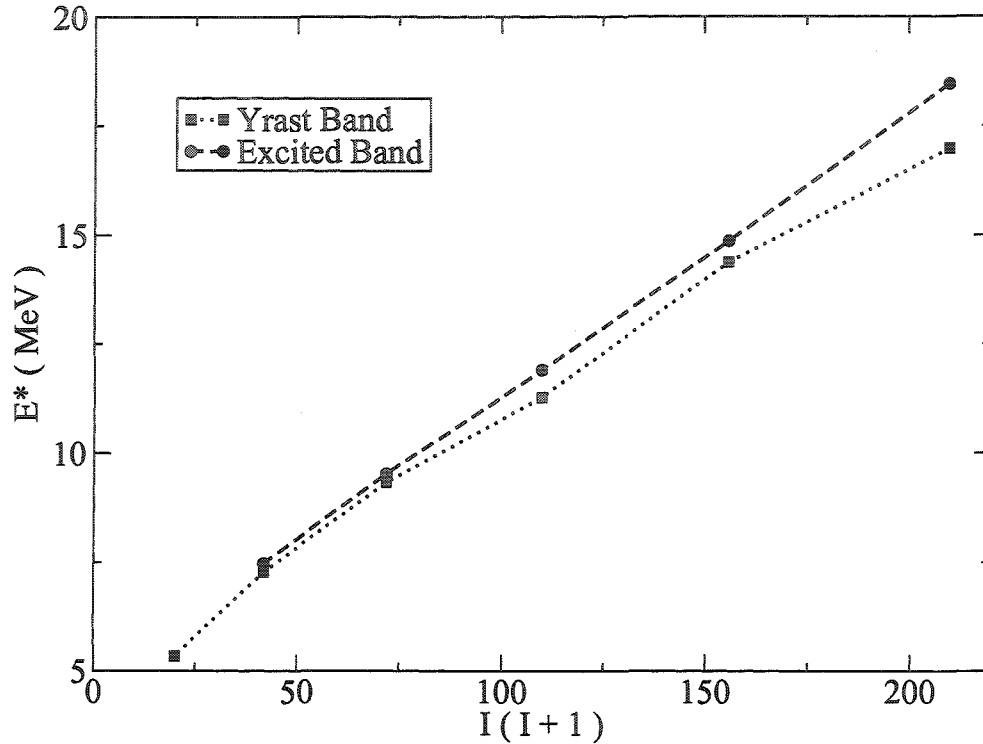


Figure 5.9: Highly Deformed Bands

The energies of states in the the highly deformed bands are plotted as a function of $I(I+1)$. The excited band varies smoothly, but the yrast band has a kink at the 10^+ state, where the interaction between the two bands is strongest.

configuration of those states is close enough to allow overlap (see the discussion in section 2.6) of their wavefunctions. The fact that there are many transitions between the normal deformed structures in ^{38}Ar and the highly deformed ones reflects the fact that a light nucleus has only a limited number of configurations available to it, so many of them will bear a resemblance to one another, permitting interactions.

The strongest interaction between the two deformed bands in ^{38}Ar appears at spin 10, where there are very strong transitions between the two bands (in fact, stronger than the yrast transitions). Figure 5.9 shows the effect that the interactions

I_i	I_f	Yrast		Excited	
		E_γ (keV)	ΔE_γ (keV)	E_γ (keV)	ΔE_γ (keV)
14	12	2610		3593	
12	10	3090	-479	2961	632
10	8	1958	1132	2378	583
8	6	2050	-92	2046	332
6	4	1939	111	1437	609
4	2	1413	526	898	539
2	0	360	1053	447	451

Table 5.6: In-Band Transition Differences

The change in γ -ray energies in the band are shown. In the classical rigid rotor interpretation, the ΔE_γ values are constant.

have had on the spin 10 state in the yrast band: It has been pushed lower in energy.

Chapter 6

Conclusions

^{38}Ar is the first $N \neq Z$ nucleus in this region to be shown to display superdeformation. Determination of the lifetimes by DSAM shows that there are two highly deformed bands. One, the yrast band, has a deformation parameter $\beta_2 = (0.30 \pm 0.03)$. The other, excited band, may have a deformation as high as $\beta_2 = 0.95_{-0.27}^{+0.54}$. The deformation of the excited band is certainly higher than $\beta_2 = 0.68_{-0.14}^{+0.22}$. That deformation is greater than that determined for the superdeformed band in ^{40}Ca , $\beta_2 = 0.59_{-0.26}^{+0.11} \pm 0.06$ [Chi03b]. The deformation of the yrast band is less than that, and it is also less than the deformation of the superdeformed band in ^{36}Ar , quoted as $\beta_2 = 0.46 \pm 0.03$ at the decay out of the band [Sve01a]. The deformation of the excited band in ^{38}Ar is greater than the deformation of the superdeformed band observed in ^{36}Ar , which has a γ deformation predicted to be as high as 60° .

Superdeformation in this light nucleus allows us to see the contest between collective and single-particle behaviour. The pressure of high angular momentum

drives the collective nuclear body into a superdeformed shape. The fact that individual nucleons must change their occupation of orbitals to achieve a new overall shape imposes irregular transition energies, and a high degree of interaction between the superdeformed shapes and the normal deformed structure.

There has not been a full microscopic calculation of this nucleus because it does not fall on the $N = Z$ line, so the parameter space is too big for a decent truncated calculation. Presumably, in the not-too-distant future a calculation will be made. Calculations reveal the contributions of individual orbitals to the overall structure. If the calculations are grossly imperfect, that indicates imperfections in our models. Improvements in the models are considered to be improvements in our understanding, perhaps even steps towards the all-encompassing theory (or even law!) of nuclear interactions that I felt was lacking when I first was drawn to the field.

Appendix A

Gamov Approximation

A straightforward description of the Gamov theory of α decay can be found for example in [Gri95], pp.281-283, and its use is nicely illustrated in [Kra88], p.253. The discussion that follows goes a step further than Griffiths, in that the angular momentum of the system is allowed to be non-zero. The only other modification is that I will apply it to proton decay, which only affects the masses and charges involved.

The argument begins from the premise that T , the probability of a quantum body tunnelling through a barrier is given by

$$T \cong e^{-2\gamma} \tag{A.1}$$

where

$$\gamma \equiv \frac{1}{\hbar} \int_{r_1}^{r_2} |p(r)| dr \tag{A.2}$$

and r_1 is the limit of the attractive nuclear potential well and r_2 is the limit of the repulsive Coulomb potential barrier, usually defined as $1.2A^{\frac{1}{3}}$ fm where A is the mass

number of the recoil. $p(r)$ is momentum,

$$p(r) = \sqrt{2m[V(r) - E]}. \quad (\text{A.3})$$

The potential energy $V(r)$ is

$$V(r) = \frac{Ze^2}{4\pi\epsilon_0 r} - \frac{\hbar^2}{2m} \frac{\ell(\ell+1)}{r^2}, \quad (\text{A.4})$$

and the energy E is

$$E = V(r_2) = \frac{Ze^2}{4\pi\epsilon_0 r_2} - \frac{\hbar^2}{2m} \frac{\ell(\ell+1)}{r_2^2}, \quad (\text{A.5})$$

because that is how r_2 is defined. It is of course more useful to specify that

$$r_2 = \frac{\frac{Ze^2}{4\pi\epsilon_0} + \sqrt{\left(\frac{Ze^2}{4\pi\epsilon_0}\right)^2 + 4E\frac{\hbar^2}{2m}\ell(\ell+1)}}{2E}. \quad (\text{A.6})$$

Although equation A.6 is ungainly, it is beneficial to use it, since E is the energy of the particle (measured) and Z is the proton number of the recoil.

After a bit of manipulation, the equation to solve is

$$\gamma = \frac{1}{\hbar} \int_{r_1}^{r_2} \sqrt{2m \left(\frac{Ze^2}{4\pi\epsilon_0 r} + \frac{\hbar^2}{2m} \frac{\ell(\ell+1)}{r^2} - E \right)} dr. \quad (\text{A.7})$$

At this stage it is helpful to define a few quantities to make the solution easier to follow:

$$\begin{aligned} k_1 &\equiv \frac{\hbar}{2m} \ell(\ell+1) \\ k_2 &\equiv \frac{Ze^2}{4\pi\epsilon_0} \\ r_2 &= \frac{k_2 + \sqrt{k_2^2 + 4Ek_1}}{2E} \\ \Delta &\equiv k_2^2 + 4Ek_1 \end{aligned} \quad (\text{A.8})$$

Equations A.8 reduce equation A.7 to

$$\gamma = \frac{1}{\hbar} \int_{r_1}^{r_2} \frac{\sqrt{2m}}{r} \sqrt{k_1 + k_2 r - Er^2} dr. \quad (\text{A.9})$$

The solution to equation A.9 can be looked up in a table. It is

$$\begin{aligned} \gamma = & \sqrt{2m} \left\{ \sqrt{k_1 + k_2 r_2 - Er_2} - \sqrt{k_1 + k_2 r_1 - Er_1} \right. \\ & - \sqrt{k_1} \left[\operatorname{atanh} \left(\frac{2k_1 + k_2 r_2}{2\sqrt{k_1} \sqrt{k_1 + k_2 r_2 - Er_2^2}} \right) - \operatorname{atanh} \left(\frac{2k_1 + k_2 r_1}{2\sqrt{k_1} \sqrt{k_1 + k_2 r_1 - Er_1^2}} \right) \right] \\ & \left. - \frac{k_2}{2\sqrt{E}} \left[\arcsin \left(\frac{k_2 - 2Er_2}{\sqrt{-\Delta^2}} \right) - \arcsin \left(\frac{k_2 - 2Er_1}{\sqrt{-\Delta^2}} \right) \right] \right\}, \quad (\text{A.10}) \end{aligned}$$

which reduces to

$$\begin{aligned} \gamma = & \frac{\sqrt{2m}}{h} \left\{ \frac{k_2}{2\sqrt{E}} \left[\arccos \left(\sqrt{(1-x^2)(1-y^2)} + xy \right) \right] \right. \\ & - \ln \left(\frac{r_1}{r_2} \frac{2k_1 + k_2 r_2}{2k_1 + k_2 r_1 + 2\sqrt{k_1}(k_1 + k_2 r_1 - Er_1^2)} \right) \\ & \left. - \sqrt{k_1 + k_2 r_1 - Er_1^2} \right\} \quad (\text{A.11}) \end{aligned}$$

when we define

$$\begin{aligned} x & \equiv \frac{k_2 - 2Er_2}{\sqrt{\Delta}} \\ y & \equiv \frac{k_2 - 2Er_1}{\sqrt{\Delta}}. \end{aligned}$$

Gamov's approximation was that the α particle was pre-formed inside the nucleus, with a particular velocity. A proton is obviously already existent inside the nucleus, and we will follow Gamov's assumption that it has a velocity v which determines its "knocking frequency",

$$\frac{2r_1}{v}. \quad (\text{A.12})$$

A standard guess for v is the velocity of the proton (or α) after it has escaped, i.e., the measured velocity.

Finally, we follow Gamov's approximation that the lifetime for the decay will be the knocking frequency multiplied by the probability of tunnelling

$$\tau = \frac{2r_1}{v} e^{2\gamma}. \quad (\text{A.13})$$

Clearly, there are many assumptions involved in this calculation (not the least of which being the guess at the knocking frequency), so it is best to interpret its results relative to each other, not as definite or absolute quantities.

Appendix B

Table of Symbols and Abbreviations

What follows is a list of the Roman letters and Greek symbols used in the body of this thesis, with a definition. There are a number of examples of multiple uses of a single symbol. Context should make it clear which definition is appropriate in those circumstances.

αalpha particle, the ^4He nucleus
β scaled velocity of recoil when state decays
β_{corr}varying fraction of calculated scaled velocity of compound system
β_{full}calculated scaled velocity of compound system
β_2deformation parameter
γdeformation parameter
δdeformation parameter

Δ	“the change in”
ϵ_2	deformation parameter
θ	polar spherical angle
λ	nuclear decay constant
λ	primary index of spherical harmonic function
μ	secondary index of spherical harmonic function
ν :	neutron configuration
π	parity
π :	proton configuration
τ	lifetime
ϕ	azimuthal spherical angle
A	number of decays from a radioactive sample
amu	atomic mass unit
ANL	Argonne National Laboratory
ATLAS	Argonne Tandem Linear Accelerator System
BGO	bismuth germanate
c	speed of light
DSAM	Doppler shift attenuation method
E	energy
E1	electric dipole

E2	electric quadrupole
E3	electric octupole (<i>etc.</i>)
ECR	electron cyclotron resonance
eV	electron volt
FMA	Fragment Mass Analyser
Gb	gigabyte
GSFMA93	serial number of experiment which produced these results
H	total γ -ray energy
h	hole
\hbar	Planck's constant, scaled by 2π
HI	heavy ion
HPGe	high-purity germanium
I	total nuclear angular momentum
i	nucleon spin angular momentum
\mathcal{J}	moment of inertia
j	nucleon total angular momentum
ℓ	orbital angular momentum
LBNL	Lawrence Berkeley National Laboratory
M1	magnetic dipole
M2	magnetic quadrupole

M3	magnetic octupole (<i>etc.</i>)
m_e	electron mass
N	number of neutrons in a nucleus
N	number of nuclei in sample
N_0	number of nuclei in sample at time $t = 0$
n	neutron
NS	Northcliffe and Schilling
p	proton
p	particle
Q_{20}	quadrupole moment
Q_t	transition quadrupole moment
R	nuclear radius
R_0	average nuclear radius
S	spectrum
t	time
$t_{1/2}$	half-life
T	kinetic energy
TEP	total energy plane
Z	number of protons in nucleus
ZC	Ziegler and Chu

Bibliography

- [Aar79] J.M. Aarts, G.A.P. Engelbertink, H.H. Eggenhuisen, and L.P. Ekström. *Nuclear Physics*, A321:515–532, 1979.
- [Ald74a] C. Alderliesten, P.G.A.M. Aerts, H.M.J. van Bijlert, and C. van der Leun. *Nuclear Physics*, A220:284–316, 1974.
- [Ald74b] C. Alderliesten and C.A.L. van Loon. *Nuclear Physics*, A220:317–334, 1974.
- [Bal72] G.C. Ball, W.G. Davies, J.S. Forster, A.N. James, and D. Ward. *Nuclear Physics*, A182:529–540, 1972.
- [Bet74] P. Betz, H. Röpke, G. Hammel, V. Glattes, and W. Brendler. *Zeitschrift für Physik*, 271:195–199, 1974.
- [Bha84] R.K. Bhalla and A.R. Poletti. *Nuclear Physics*, A420:96–108, 1984.
- [Bla66] A.E. Blaugrund. *Nuclear Physics*, 88:501–512, 1966.
- [Bol86] Lowell M. Bollinger. *Annual Review of Nuclear and Particle Science*, 36:475–503, 1986.

- [Bol93] L.M. Bollinger, R.C. Pardo, K.W. Shepard, J.M. Bogaty, B.E. Clift, F.H. Munson, and G. Zinkann. *Nuclear Instruments and Methods in Physics Research*, A328:221–230, 1993.
- [Chi03a] C.J. Chiara. private communication, 2003.
- [Chi03b] C.J. Chiara, E. Ideguchi, M. Devlin, D.R. LaFosse, F. Lerma, W. Reviol, S.K. Ryu, D.G. Sarantites, C. Baktash, A. Galindo-Uribarri, M.P. Carpenter, R.V.F. Janssens, T. Lauritsen, C.J. Lister, P. Reiter, D. Seweryniak, P. Fallon, A. Görden, A.O. Macchiavelli, and D. Rudolph. *Physical Review*, C 67:041303(R), 2003.
- [Cro93] Mario Cromaz. 8PISORT. Computer code, 1993.
- [Dav92] C.N. Davids, B.B. Back, K. Bindra, D.J. Henderson, W. Kutschera, T. Lauritsen, Y. Nagame, P. Sugathan, A.V. Ramayya, and W.B. Walters. *Nuclear Instruments and Methods in Physics Research B*, 70:358–365, 1992.
- [Dia80] R.M. Diamond and F.S. Stephens. *Annual Review of Nuclear and Particle Sciences*, 30:80–157, 1980.
- [Ewa64] G.T. Ewan and A.J. Tavendale. *Nuclear Instruments and Methods*, 26:183–186, 1964.
- [Fal] Paul Fallon. Gammasphere WorldWideWeb Server at Lawrence Berkeley National Laboratory. <http://www-gam.lbl.gov/>.

- [FSB+96] Richard B. Firestone, Virginia S. Shirley, Coral M. Baglin, S.Y. Frank Chu, and Jean Zipkin. *Table of Isotopes*. John Wiley & Sons, Toronto, eighth edition, 1996.
- [Gam28] G. Gamow. *Zeitschrift für Physik*, 51:204–212, 1928.
- [Gla76] F. Glatz, G. Pappert, A. Brachet, P. Betz, and H. Röpke. *Zeitschrift für Physik A*, 278:319–325, 1976.
- [Gra69] H. Grawe and K.P. Lieb. *Nuclear Physics*, A127:13–32, 1969.
- [Gri95] David J. Griffiths. *Introduction to Quantum Mechanics*. Prentice-Hall, New Jersey, 1995.
- [Has98] Dean Stuart Haslip. *Studies of $\Delta I = 4$ bifurcation in $A \sim 150$ super-deformed bands*. PhD thesis, McMaster University, 1998.
- [Hil53] David Lawrence Hill and John Archibald Wheeler. *Physical Review*, 89:1102–1145, 1953.
- [Ide01] E. Ideguchi, D.G. Sarantites, W. Reviol, A.V. Afanasjev, M. Devlin, C. Baktash, R.V.F. Janssens, D. Rudolph, A. Axelsson, M.P. Carpenter, A. Galindo-Uribarri, D.R. LaFosse, T. Lauritsen, F. Lerma, C.J. Lister, P. Reiter, D. Seweryniak, M. Weiszflog, and J.N. Wilson. *Physical Review Letters*, 87:222501, 2001.
- [Jam71] A.N. James, P.R. Alderson, D.C. Bailey, P.E. Carr, J.L. Durell, L.L. Green, M.W. Greene, and J.F. Sharpey-Schafer. *Nuclear Physics*, A168:56–64, 1971.

- [Ker72] B.D. Kern and P.D. Bond. *Nuclear Physics*, A181:403–408, 1972.
- [Ker80] B.D. Kern, P. Betz, E. Bitterwolf, F. Glatz, and H. Röpke. *Zeitschrift für Physik A*, 294:51–64, 1980.
- [Kno89] Glenn F. Knoll. *Radiation Detection and Measurement*. Wiley, Toronto, second edition, 1989.
- [Kol76] J.J. Kolata, J.W. Olness, E.K. Warburton, and A.R. Poletti. *Physical Review C*, 13:1944–1951, 1976.
- [Kra88] Kenneth S. Krane. *Introductory Nuclear Physics*. John Wiley & Sons, Toronto, second edition, 1988.
- [Lap84] R. Lappalainen, J. Keinonen, A. Anttila, A. Kiss, and E. Somorjai. *Nuclear Physics*, A426:287–300, 1984.
- [Laua] Torben Lauritsen. Gammasphere @ ANL.
<http://www.phy.anl.gov/gammasphere/index.html>.
- [Laub] Torben Lauritsen. Physics division equipment picture gallery.
<http://www.phy.anl.gov/gallery/equipment/index.html>.
- [Lee90] I-Y. Lee. *Nuclear Physics A*, 520:641c–655c, 1990.
- [Leo87] William R. Leo. *Techniques for Nuclear and Particle Physics Experiments; A How-to Approach*. Springer-Verlag, New York, 1987.
- [Lie68] K.P. Lieb, H. Röpke, H. Grawe, H.J. Brundiers, and O. Klepper. *Nuclear Physics*, A108:233–240, 1968.

- [Lin72] J. Lindskog, D.M. Gordon, and R.W. Kavanagh. *Nuclear Physics*, A187:1–11, 1972.
- [Löb70] K.E.G Löbner, M. Vetter, and V. Hönig. *Nuclear Data Tables*, A7:495–564, 1970.
- [Lov89] D. Love. QVAL. Computer code, 1989.
- [Noo84] G.J.L. Nooren, H.P.L. de Esch, and C. van der Leun. *Nuclear Physics*, A423:228, 1984.
- [Nor70] L.C. Northcliffe and R.F. Schilling. *Nuclear Data Tables A*, 7:233–463, 1970.
- [Nya84] B.M. Nyakó, J.R. Cresswell, P.D. Forsyth, D. Howe, P.J. Nolon, M.A. Riley, J.F. Sharpey-Schafer, J. Simpson, N.J. Ward, and P.J. Twin. *Physical Review Letters*, 52:507 – 510, 1984.
- [PB75] M.A. Preston and R.K. Bhaduri. *Structure of the Nucleus*. Addison-Wesley, Reading, 1975.
- [Pol62] S.M. Polikanov, V.A. Druin, V.A. Karnaukhov, V.L. Mikheev, A.A. Pleve, N.K. Skobelev, V.G. Subbotin, G.M. Ter-Akop'yan, and V.A. Fomichev. *Soviet Physics JETP*, 15:1016–1021, 1962.
- [Rad95a] D.C. Radford. *Nuclear Instruments and Methods in Physics Research A*, 361:306–316, 1995.
- [Rad95b] D.C. Radford. *Nuclear Instruments and Methods in Physics Research A*, 361:297–205, 1995.

- [Rud02] D. Rudolph, A. Poves, C. Baktash, R.A.E. Austin, J. Ebarth, D. Haslip, D.R. LaFosse, M. Lipoglavšek, S.D. Paul, D.G. Sarantites, C.E. Svensson, H.G. Thomas, J.C. Waddington, W. Weintraub, and J.N. Wilson. *Physical Review C*, 65:034305, 2002.
- [Sar] Dmitrios Sarantites. The Microball. <http://wunmr.wustl.edu/dgs/mball/>.
- [Sar96] D.G. Sarantites, P.-F. Hua, M. Devlin, L.G. Sobotka, J. Elson, J.T. Hood, D.R. LaFosse, J.E. Sarantites, and M.R. Maier. *Nuclear Instruments and Methods in Physics Research A*, 381:418–432, 1996.
- [Sie77] S.H. Sie, D. Ward, J.S. Geiger, R.L. Graham, and H.R. Andrews. *Nuclear Physics A*, 291:443–458, 1977.
- [Sko70] L.D. Skouras. *Physics Letters*, 31B:439–441, 1970.
- [Ste65] P.H. Stelson and L. Grodzins. *Nuclear Data A*, 1:21–102, 1965.
- [Sto94] Tom Stoppard. *Hapgood (I:v)*. Faber and Faber, London, second edition, 1994.
- [Str67] V.M. Strutinsky. *Nuclear Physics*, A95:420–442, 1967.
- [Sve96] C.E. Svensson. GSSORT. Computer code, 1996.
- [Sve97] C.E. Svensson, J.A. Cameron, S. Flibotte, G. Gervais, Haslip D.S., J.M. Nieminen, J.C. Waddington, J.N. Wilson, G.C. Ball, A. Galindo-Uribarri, V.P. Janzen, D.C. Radford, D. Ward, M. Cromaz, and T.E. Drake. *Nuclear Instruments and Methods in Physics Research A*, 396:228, 1997.

- [Sve00] C.E. Svensson, A.O. Macchiavelli, A. Juodagalvis, A. Poves, I. Ragnars-son, S. Åberg, D.E. Appelbe, R.A.E. Austin, C. Baktash, G.C. Ball, M.P. Carpenter, E. Caurier, R.M. Clark, M. Cromaz, M.A. Deleplanque, R.M. Diamond, P. Fallon, M. Furlotti, A. Galindo-Uribarri, R.V.F. Janssens, G.J. Lane, I.Y. Lee, M. Lipoglavšek, F. Nowacki, S.D. Paul, D.C. Radford, D.G. Sarantites, D. Seweryniak, F.S. Stephens, V. Tomov, K. Vetter, D. Ward, and C.H. Yu. *Physical Review Letters*, 85:2693–2696, 2000.
- [Sve01a] C.E. Svensson, A.O. Macchiavelli, A. Juodagalvis, A. Poves, I. Ragnars-son, S. Åberg, D.E. Appelbe, R.A.E. Austin, C. Baktash, G.C. Ball, M.P. Carpenter, E. Caurier, R.M. Clark, M. Cromaz, M.A. Deleplanque, R.M. Diamond, P. Fallon, M. Furlotti, A. Gallindo-Uribarri, R.V.F. Janssens, G.J. Lane, I.Y. Lee, M. Lipoglavšek, F. Nowacki, S.D. Paul, D.C. Radford, D.G. Sarantites, D. Seweryniak, F.S. Stephens, V. Tomov, K. Vetter, D. Ward, and C.H. Yu. *Acta Physica Polonica B*, 32, 2001.
- [Sve01b] C.E. Svensson, A.O. Macchiavelli, A. Juodagalvis, A. Poves, I. Ragnars-son, S. Åberg, D.E. Appelbe, R.A.E. Austin, G.C. Ball, M.P. Carpen-ter, E. Caurier, R.M. Clark, M. Cromaz, M.A. Deleplanque, R.M. Dia-mond, P. Fallon, R.V.F. Janssens, G.J. Lane, I.Y. Lee, F. Nowacki, D.G. Sarantites, F.S. Stephens, K. Vetter, and D. Ward. *Physical Review C*, 63:061301(R), 2001.
- [Twi85] P.J. Twin, A.H. Nelson, B.M. Nyakó, D. Howe, H.W. Cranmer-Gordon, D. Elenkov, P.D. Forsyth, J.K. Jabber, J.F. Sharpey-Schafer, J. Simpson, and G. Sletten. *Physical Review Letters*, 55:1380 – 1383, 1985.

- [Twi86] P.J. Twin, B.M. Nyakó, A.H. Nelson, J. Simpson, M.A. Bentley, H.W. Cranmer-Gordon, P.D. Forsyth, D. Howe, A.R. Mokhtar, J.D. Morrison, J.F. Sharpey-Schafer, and G. Sletten. *Physical Review Letters*, 57:811–814, 1986.
- [Zie74] J.F. Ziegler and W.K. Chu. *Atomic Data and Nuclear Data Tables*, 13:463–489, 1974.